FIRST-PRINCIPLE APPROACHES TO STRONGLY CORRELATED QUANTUM SPIN SYSTEMS

FIRST-PRINCIPLE APPROACHES TO STRONGLY CORRELATED QUANTUM SPIN SYSTEMS

A Thesis Presented

by

YUAN HUANG

Submitted to the Graduate School of the
University of Massachusetts Amherst in partial fulfillment
of the requirements for the degree of

DOCTOR OF PHILOSOPHY

May 2018

Physics Department

FIRST-PRINCIPLE APPROACHES TO STRONGLY CORRELATED QUANTUM SPIN SYSTEMS

A Thesis Presented

by

YUAN HUANG

Approved as to style and content by:

Boris V. Svistunov, Co-chair

Nikolay V. Prokof'ev, Co-chair

Gregory Grason, Member

Tigran Sedrakyan, Member

Narayanan Menon, Department Chair
Physics Department

ACKNOWLEDGEMENTS

First and foremost I want to thank my supervisors Prof. Boris Svistunov and Prof. Nikolay Prokof'ev. I cannot express my gratitude enough for their support and guidance that have led me through my research. I appreciate all their contributions of time, ideas, and funding to make my Ph.D. experience productive and stimulating. They have taught me, both consciously and unconsciously, how good physics research is done. The enthusiasm they both have for their research is contagious and motivational for me, even during the tough times in my Ph.D. pursuit.

The members of our Theoretical Quantum Fluids Group have contributed immensely to my personal and professional time at UMass. The group has been a great source of friendship as well as good advice and collaboration. I am especially grateful for all the fun group members who spent all these enjoyable time with me: graduate students Kun Chen and Zhiyuan Yao; and postdocs Olga Goulko and Johan Carlström. I would like to acknowledge the group's adjunct professor Youjin Deng, who is also my former Ph.D. advisor at Univerisity of Science and Technology of China. We worked together on both the deconfined criticality and frustrated magnets diagrammatic Monte Carlo studies, and I very much appreciate the inspirational discussions with him. Other current and past group members and visitors that I have had the pleasure to meet and have discussions with are Egor Babaev, Igor Tupitsyn, Fèlix Werner, Kris Van Houcke, Lode Pollet, Evgeny Kozik, Evgeni Burovski, Sergey Kulagin, Karine Piacentini, Takahiro Ohgoe, Fedor Simkovic and Riccardo Rossi.

The deconfined criticality studies discussed in this dissertation would not have been possible without Prof. Anatoly Kuklov and Kun Chen. Anatoly made significant contributions to the simulations on the deconfined critical action and Kun

contributed a lot in the path-integral Monte Carlo simulations of the JQ model. For the diagrammatic Monte Carlo studies, Kun also provided me a lot of help in setting up the object oriented framework for the large-scale Monte Carlo code and carrying out the simulations. I am really grateful for their collaborations. I would also like to thank Anders Sandvik, Oleg Starykh, Gang Chen, Andrey Mishchenko, and especially the late Christopher Henley for advice and inspiring discussions in the deconfined criticality and diagrammatic Monte Carlo studies.

For this dissertation I would like to thank my committee members: Tigran Sedrakyan and Gregory Grason for their time, interest, and helpful comments. I gratefully acknowledge the funding sources that made my Ph.D. work possible. My work was supported by the Simons Collaboration on the Many Electron Problem, the National Science Foundation, the MURI Program "New Quantum Phases of Matter" from the AFOSR.

My time at UMass was made enjoyable in large part due to all my great friends that became a part of my life. I am grateful for all the pleasant off-work time spent with my friends (including my beloved supervisors Nikolay and Boris), for our memorable hiking and cycling trips, for Nikolay and Svetlana's hospitality during all the holiday times and especially during the summer of 2016, and for many other people and memories.

Lastly, I would like to thank my family for all their love and encouragement. For my parents who raised me with a love of science and supported me in all my pursuits. And most of all for my loving, supportive, encouraging, and patient husband Kun who is always there for me in all my ups and downs. I simply could not imagine doing all of these without you.

Thank you.

ABSTRACT

FIRST-PRINCIPLE APPROACHES TO STRONGLY CORRELATED QUANTUM SPIN SYSTEMS

MAY 2018

YUAN HUANG

B.Sc., UNIVERSITY OF SCIENCE AND TECHNOLOGY OF CHINA

Ph.D., UNIVERSITY OF SCIENCE AND TECHNOLOGY OF CHINA

Ph.D., UNIVERSITY OF MASSACHUSETTS AMHERST

Directed by: Professor Boris V. Svistunov and Professor Nikolay V. Prokof'ev

My Ph.D. research focuses on the numerical study of two quantum spin systems—one is the square-lattice Heisenberg antiferromagnet with ring-exchange interaction at the Nèel to valence-bond solid state transition, which is proposed to be described by the theory of deconfined criticality; the other is the highly frustrated pyrochlore Heisenberg antiferromagnet. Both systems are known as prototypical candidates for the exotic spin-liquid state with emergent fractionalized excitations and gauge structure. Regarding the long standing controversy of deconfined criticality, our results conclude that the deconfined critical theory capture the essence of the Nèel to valence-bond solid state transition *at least* at intermediate scales of distances, and also suggest that both the deconfined critical point and the Nèel to valence-bond solid state transition are weak first-order transitions. In the frustrated pyrochlore

Heisenberg antiferromagnet, we found a wide cooperative paramagnetic temperature regime where the system is in an emergent thermal spin-ice state. The conclusion is drawn by a remarkably accurate microscopic correspondence for static structure factor between the quantum Heisenberg model and its classical counterparts. An analysis for the dynamic structure factor obtained by the analytic continuation of numerical data is also performed, showing a result consistent with diffusive spinon dynamics of certain special modes.

TABLE OF CONTENTS

LIST OF TABLES

Table **Page**

LIST OF FIGURES

Figure **Page**

INTRODUCTION

The modern research in condensed matter physics aims at understanding the collective behavior that may emerge when large numbers of atoms or molecules organize into solids or liquids. In such systems, one can hardly directly apply fundamental laws of physics using only analytical methods. However it is possible to find simple models that capture the nontrivial physics phenomena in a complicated system and simulate them numerically. Numerical approaches play an essential role in understanding the emergent phenomena in many-body systems while providing quantitatively accurate results.

In the field of magnetism, a system of interest can be reduced to a minimal model having only spin degrees of freedom. At high temperature, the spins are randomly oriented. When decreasing the temperature below a certain critical point, the ferromagnetic or antiferromagnetic interactions can force the spins to form an aligned or anti-aligned pattern. This is an example of spontaneous symmetry breaking phenomenon. There exist other types of phases and phase transitions that do not fit in this scenario. The most famous example in magnetism is the spin-liquid state.

Spin liquids is a type of "quantum-disordered" ground states of spin systems, in which quantum fluctuations are so strong that they prevent conventional magnetic long-range order. More interestingly, quantum spin liquids (QSLs) feature massive many-body entanglement, which gives rise to unique properties such as emergent non-local excitations, topological order, and gauge structure [3, 4]. Extensive experimental and theoretical search for materials and models, which may realize this intriguing QSL state, is crucial in modern condensed matter physics.

Deconfined Criticality. One possible realization of quantum spin liquids was proposed at a special type of quantum critical points, the deconfined critical point (DCP). The concept of deconfined criticality was introduced in the context of quantum phase transitions in two dimensions (2D), between phases characterized by different broken symmetries. The hallmark of DCP theory is the prediction of the emergence of fractional degrees of freedom (spinons) and gauge fields at the critical point, which can not be expressed in terms of the order parameters on either side of the transition [5]. The emergent gauge structure indicates that the system at DCP is a critical spin liquid.

It was suggested that, at DCP, the universality class of the transition is captured by a 3D classical action involving two complex-valued matter fields (describing spinons) coupled to a gauge field [5, 6, 7]. However, the studies of this proposed DCP action with different symmetries revealed generic runaway renormalization-group flows consistent with weak first-order transitions for any strength of the gauge interaction [8, 9].

On the other hand, the numerical study of microscopic models that are candidates for deconfined criticality have been yielding inconclusive results. Early studies of the antiferromagnetic SU(2)-symmetric J-Q model [10, 11, 12] suggested that the Nèel phase (antiferromagnetic phase) transforms into the valence-bond solid (VBS) in a continuous fashion, while subsequent work [13, 14] revealed violations of scale invariance. It is important, however, that, up to linear system sizes of a few hundred sites, the J-Q model clearly demonstrates an emergent U(1) symmetry and its runaway flow remains rather weak, leaving room for speculations about the second-order DCP scenario [14].

In Chapter 1, we perform a direct quantitative comparison of critical flows in the J-Q model and the 3D SU(2)-symmetric effective model for the DCP theory, the discrete noncompact CP^1 ($NCCP^1$) model. We find that the winding-number flows [8, 9] of

the two models coincide with each other in a significantly large region of linear system sizes, suggesting that independently of the order of the transition, the DCP theory in general, and the 3D SU(2)-symmetric discrete NCCP^1 model, in particular, capture the essence of the quantum phase transition *at least* at intermediate scales of distances. At larger sizes we observe significant deviations between the two flows, which preserve their runaway character. The most conservative conclusion then is that at least one of the two models does not feature the second-order criticality, with the straightforward interpretation being that both models feature weak first-order transitions.

Frustrated magnets. Quantum spin liquid does not necessarily correspond to quantum critical state, but also can exist as a stable phase in certain antiferromagnetic systems. These systems usually have Hamiltonians with competing interactions which make contributions to the energy that cannot simultaneously be minimised. This phenomon is often called "frustration." In a classical system, frustration leads to a large degeneracy of the ground-state. Quantum fluctuations lift the ground-state degeneracy and lead the system to either an ordered ground state—this effect is usually referred to as the "order by disorder" phenomenon—or a strongly correlated yet disordered ground state, which is the quantum spin liquid [15]. In many quantum antiferromagnets (AFMs), frustration has a simple geometric origin when nearest-neighbor spins form triangular or tetrahedral units. The canonical three-dimensional example of such a system is the Heisenberg AFM on a pyrochlore lattice that consists of corner-sharing tetrahedrons.

At moderate temperatures, thermal fluctuations still preserve the strongly correlated motion of spins. Such a state is referred to as "cooperative paramagnet." In frustrated magnets, there is usually a wide temperature interval where the spins are strongly interacting but remain in a disordered cooperative paramagnetic state. Unbiased understanding of spin correlations and dynamics in this regime is a crucial task.

The bold diagrammatic Monte Carlo (BDMC) methods provides a unique tool to numerically attack strongly correlated frustrated magnets in a controlled manner, provided the skeleton diagram series are convergent or subject to resummation. In this thesis, we not only apply the established BDMC method based on G^2W expansion [16, 17] to the frustrated magnets, but also explore several possibilities to further improve the performance of BDMC.

In Chapter 2, we introduce the bold diagrammatic Monte Carlo method based on the G^2W-skeleton expansion, and also explore the possibility of employing the full skeleton technique based on the effective three-point vertex. In Chapter 3, we introduce a new approach, referred to as Conserving Bold Diagrammatic Monte Carlo (CBDMC), which allows us to construct observables that satisfy conservation laws order by order in the bold diagrammatic Monte Carlo framework. In Chapter 4, we show the results from BDMC and CBDMC simulations in various quantum spin systems with or without frustration and compare the performance with high-temperature expansions.

In Chapter 5, we study low-temperature physics in the cooperative paramagnetic regime of the SU(2)-symmetric spin-1/2 Heisenberg antiferromagnet on a 3D pyrochlore lattice using the BDMC method. We find that there exists a large temperature interval in which the system can be described as a thermal spin-ice state. The spin-ice state features emergent gapped $S_z = 1/2$ spinons with Coulomb interactions, and can be considered as a classical spin liquid.

Our conclusions are based on the results of BDMC [18, 17] simulations. The method of BDMC combines the most versatile theoretical tool—Feynman diagrams—with the power of Monte Carlo sampling of multi-dimensional configuration spaces. In a system of spins, the diagrammatic representation is achieved by mapping the spin operators into auxiliary fermions with imaginary chemical potential [19]. One of the advantages of Feynman diagrammatic representation is the ability to apply standard

tricks of the analytic diagrammatic approach to reduce the number of diagrams by self-consistently taking into account chains of repeating parts as, e.g., in the Dyson equation, or screening equation. This is the essence of BDMC method introduced in Ref. [18]. In a word, the BDMC method is a controlled numerical approach based on stochastic sampling of all skeleton Feynman diagrams up to some high order N and extrapolation to the $N \to \infty$ limit. The series are supposed to be convergent or subject to the analytic continuation beyond convergence radius by resummation protocols. Our implementation of BDMC algorithm is based on the G^2W-skeleton expansion in the real-space–imaginary-time representation similar to that described in Refs. [16]. In our study, the skeleton series show good convergence down to the temperature $T/J = 1/6$.

The identification of the spin-ice state is achieved through a remarkably accurate microscopic correspondence for static structure factor between the quantum Heisenberg, classical Heisenberg, and Ising models at all accessible temperatures, given that both classical spin models are dominated by the spin-ice physics at low temperature [20, 21]. In the static structure factor, we also find the spin-ice characteristic bow-tie pattern with pinch points. The dynamic structure factor at real frequencies (obtained by the analytic continuation of numerical data) is consistent with diffusive spinon dynamics at those pinch points.

CHAPTER 1

DECONFINED CRITICALITY

The text of this chapter has been adapted from Ref. [22].

1.1 Introduction to Deconfined Criticality

The concept of the deconfined critical point (DCP) [23, 5, 6, 24, 25] was developed for understanding quantum transitions in two dimensions (2D) between phases characterized by different broken symmetries. The key feature of DCP is the emergence of fractional degrees of freedom (spinons) and gauge fields at the critical point (cf. [26]). Potentially, the DCP scenario has a broad range of applications ranging from quantum phases transitions in lattice models and magnets to normal-superfluid transitions in multi-component charged superconductors, etc. [23, 5, 6, 24, 25, 27, 28, 29]. Ultra-cold atoms in an optical lattice is another promising system where DCP can be tested experimentally [30].

A hallmark of the theory is a conjecture that the DCP universality class is captured by the 3D classical action involving two complex-valued matter fields, $\psi_{a=1,2}$, describing spinons coupled to a vector gauge field [23, 5, 6, 24, 25]. Depending on the symmetry group of the underlying quantum system—global U(1) or global SU(2)—the DCP action features the following symmetry in terms of its two components: either the Z_2 symmetry between two spinon fields and the U(1)×U(1) symmetry associated with the individual phases of ψ_a or an enhanced SU(2) symmetry between the spinon fields. However, flowgram studies of the typical U(1)×U(1) [8] and SU(2) [9] DCP actions revealed generic runaway flows consistent with weak first-order transitions.

The initial work focused on microscopic models of the superfluid to solid quantum phase transitions first claimed the observation of the second-order U(1)×U(1) transition [31] but severe violations of scale invariance revealed in the subsequent analysis all but ruled it out [32]. Similarly to the U(1)×U(1) case, early studies of the anti-ferromagnetic SU(2)-symmetric J-Q model [10, 13, 11] suggested that the Néel phase transforms into the valence bond solid (VBS) in a continuous fashion, while subsequent work [12, 14] revealed violations of scale invariance. It is important, however, that, up to linear system sizes of few hundred sites, the J-Q model clearly demonstrates an emergent $U(1)$ symmetry and its runaway flow remains rather weak, leaving room for speculations about the second-order DCP scenario [14].

In this chapter, we perform a direct quantitative comparison of critical flows in the J-Q and the 3D SU(2)-symmetric discrete NCCP^1 models. The rationale behind our study is as follows. Slow run-away flows in both models suggest that, independently of the order of the transition, the DCP theory in general, and the 3D SU(2)-symmetric discrete NCCP^1 model, in particular, capture the essence of the quantum phase transition *at least* at intermediate scales of distances. And we indeed find that the winding-number flowgrams [8, 9] of the two models can be collapsed in a significantly large region of linear system sizes (up to $L \approx 75$ for the J-Q model), proving the hypothesis. At larger sizes we observe significant deviations between the two flows which preserve their runaway character. The most conservative conclusion then is that at least one of the two models does not feature the second-order criticality, with the straightforward interpretation being that both models feature weak first-order transitions.

1.2 J-Q Model and Deconfined Quantum Critical Action

The SU(2)-symmetric J-Q model describing $s = 1/2$ spins on a square lattice has been analyzed in Ref. [10]:

$$H = J \sum_{\langle ij \rangle} \hat{\vec{S}}_i \hat{\vec{S}}_j - Q \sum_{\langle ijkl \rangle} (\hat{\vec{S}}_i \hat{\vec{S}}_j - \tfrac{1}{4})(\hat{\vec{S}}_k \hat{\vec{S}}_l - \tfrac{1}{4}) \; . \tag{1.1}$$

The first sum runs over nearest-neighbor sites $\langle ij \rangle$ and represents the standard Heisenberg model with $J > 0$. The second sum runs over the corners of plaquettes $\mathcal{P} = \langle ijkl \rangle$ such that ij and kl form two parallel adjacent horizontal or vertical links and adds the four-site ring-exchange terms with $Q > 0$. The model features a phase transition between the Néel and an insulating VBS phase (its precise nature, however, cannot be determined from available system sizes [11, 14]). While in the Néel phase the order parameter $\vec{S} = \langle \hat{\vec{S}} \rangle$ is linear in the spin operator, the VBS long-range order is based on a bilinear scalar combination of $\hat{\vec{S}}$. Since broken symmetries in these phases are different, according to the standard Ginzburg-Landau-Wilson paradigm a single phase transition between them must be discontinuous or through a co-existence phase where both symmetries are broken. The actual discontinuities, however, should be very weak if one of the order parameters is characterized by a significant numerical smallness far away from the transition, as is the case in the VBS phase of the J-Q model where the dimer order $\sqrt{D^2} \approx 1/20$ and no signatures of Z_4 broken symmetry are observed even for largest system sizes [10]]. Thus, if a single continuous transition were observed, this would be a strong evidence supporting the DCP scenario.

The DCP is described by the 3D classical two-component SU(2) symmetric electrodynamics with the emerging U(1) gauge vector-field $\vec{A}$ [5, 6], $H_{\rm DCP} = \int d^3x \{t|[\vec{\nabla} - \mathrm{i}\vec{A}]\psi|^2 + \frac{1}{8g}(\vec{\nabla} \times \vec{A})^2\}$, where the spinor ψ consists of two complex fields $\psi = (\psi_1, \psi_2)$. According to the mapping, the Néel vector $\vec{S} = \frac{1}{2}\vec{n}$, where $\vec{n}$ is given by

$$\vec{n} = \psi^* \vec{\sigma} \psi, \tag{1.2}$$

with $\vec{\sigma}$ standing for the Pauli matrices. With the NCCP[1] fixed-modulus constraint [23], $|\psi_1|^2 + |\psi_2|^2 = 1$, one obtains $\vec{n}^2 = (|\psi_1|^2 + |\psi_2|^2)^2 = 1$ and $n^+ = n_x + i n_y = 2\psi_1^* \psi_2$

implying that the azimuthal angle of $\vec{n}$ is the relative phase of the spinon fields, $\varphi = \varphi_2 - \varphi_1$, where $\psi_a \sim \exp(\mathrm{i}\varphi_a)$, $a = 1, 2$.

The lattice version of the DCP action on a simple cubic lattice [6, 5] is:

$$\begin{aligned} H_{\rm DCP} &= -t \sum_{\langle ij \rangle,\, a} \left(\psi^*_{ai} \psi_{aj} e^{iA_{\langle ij \rangle}} + \text{c.c.} \right) + \\ &+ \frac{1}{8g} \sum_{\mathcal{P}} \left(\vec{\nabla} \times \vec{A} \right)^2, \end{aligned} \tag{1.3}$$

where the gauge field $A_{\langle ij \rangle}$ is oriented along the bond $\langle ij \rangle$ from site j to site i, and $\vec{\nabla} \times \vec{A}$ is the lattice curl-operator evaluated on elementary plaquettes $\mathcal{P}$. The effective constants (t, g) relate in some way to the parameters of the J-Q model (1.1). Below we will present evidence that $g = 1.1$ and $t = 0.8822(4)$ provide the closest description of the J-Q model with $J/Q \approx 0.04$ up to a linear size $L \sim L^* = 75$.

Dual variables. In Ref. [9], the statistics of the model (1.3) has been reformulated in terms of the dual variables—integer bond currents $\vec{J}^{(a)}$ which obey the Kirchhoff conservation laws. The mapping to the J-current model starts from the partition function $Z = \int D\psi D\psi^* DA \exp(-S)$ and a Taylor expansion of the exponentials $\exp\{t\psi^*_{ai}\psi_{aj}e^{iA_{<ij>}}\}$ and $\exp\{t\psi^*_{aj}\psi_{ai}e^{-iA_{<ij>}}\}$ on all bonds. One can then perform an explicit Gaussian integration over $A_{<ij>}$, ψ_{ai} and arrive at a formulation in terms of integer non-negative bond currents $J^{(a)}_{i,\mu}$. We use $\mu = \pm 1, \pm 2, \pm 3$ to label the directions of bonds going out of a given site the corresponding unit vectors are denoted by $\hat{\mu}$. These J-currents obey the conservation laws:

$$\sum_{\mu} I^{(a)}_{i,\mu} = 0, \;\; \text{with} \;\; I^{(a)}_{i,\mu} \equiv J^{(a)}_{i,\mu} - J^{(a)}_{i+\hat{\mu},-\mu}. \tag{1.4}$$

The final expression for the partition function reads

$$Z = \sum_{\{J\}} \mathcal{Q}_{\rm site}\; \mathcal{Q}_{\rm bond}\; \exp(-H_J), \tag{1.5}$$

where

$$
\begin{aligned}
H_J &= \frac{g}{2} \sum_{i,j;\, a,b;\, \mu=1,2,3} I^{(a)}_{i,\mu}\, V_{ij}\, I^{(b)}_{j,\mu} \qquad (1.6)\\
\mathcal{Q}_{\rm site} &= \prod_i \frac{\mathcal{N}_i^{(1)}!\,\mathcal{N}_i^{(2)}!}{(1+\mathcal{N}_i^{(1)}+\mathcal{N}_i^{(2)})!}, \quad \mathcal{N}_i^{(a)} = \frac{1}{2}\sum_\mu J^{(a)}_{i,\mu}\\
\mathcal{Q}_{\rm bond} &= \prod_{i,a,\mu} \frac{t^{J^{(a)}_{i,\mu}}}{J^{(a)}_{i,\mu}!}\,,
\end{aligned}
$$

The long-range interaction V_{ij} depends on the distance r_{ij} between the sites i and j. Its Fourier transform is given by $V_{\mathbf{q}} = 1/\sum_{\mu=1,2,3}\sin^2(q_\mu/2)$ and implies an asymptotic behavior $V \sim 1/r_{ij}$ at large distances.

Define $\vec{W}_a$ as the windings of the bond currents $\vec{I}^{(a)}$, then the partition function$Z$ can be written as a sum of contributions from different winding sectors:

$$
Z = \sum_{\vec{W}_1,\vec{W}_2} Z(\vec{W}_1,\vec{W}_2) \qquad (1.7)
$$

Consider the case when the system is coupled to a uniform lattice gauge field $(\delta\varphi_a, \vec{A}_0)$, the partition function of the DCP action can be represented as

$$
\begin{aligned}
Z[\delta\varphi_a] = \int d\vec{A}_0 \sum_{\vec{W}_1,\vec{W}_2} Z(\vec{W}_1,\vec{W}_2)\cdot\\
\exp\left[\mathrm{i}\left(\delta\vec{\varphi}_1+\vec{A}_0\right)\cdot\vec{W}_1 + \mathrm{i}\left(\delta\vec{\varphi}_2+\vec{A}_0\right)\cdot\vec{W}_2\right], \qquad (1.8)
\end{aligned}
$$

where $\vec{A}_0$ stands for the $q = 0$ harmonic of the gauge field defined on the lattice with periodic boundary conditions, $\vec{W}_a$ are windings of the bond currents $\vec{I}^{(a)}$, and $\delta\vec{\varphi}_a$ stand for the Thouless boundary phase twists of the spinon-field phases φ_a. By definition, $Z(\vec{W}_1,\vec{W}_2)$ is the partition function in a given winding number sector. The integration over $\vec{A}_0$ yields the constraint $\vec{W}_1 + \vec{W}_2 = 0$ so that $Z = \sum_{\vec{W}} Z(\vec{W},-\vec{W})\exp(\mathrm{i}\,\delta\vec{\varphi}\cdot\vec{W})$ with $\delta\vec{\varphi} \equiv \delta\vec{\varphi}_1 - \delta\vec{\varphi}_2$.

The stiffness of the S-vector field is found from

$$\rho_S = \frac{1}{3L}\frac{d^2 \ln Z}{d(\vec{\delta\varphi})^2}\bigg|_{\vec{\delta\varphi}=0} = \frac{1}{3L}\langle \vec{W}^2 \rangle, \tag{1.9}$$

It is important that at the critical point the scaling behavior of winding numbers is characterized by $\langle \vec{W}^2 \rangle = \mathcal{O}(1)$ so that $\rho_S \propto 1/L$. In the ordered Néel phase $\langle \vec{W}^2 \rangle \propto L$ and the stiffness is finite, $\rho_S = \mathcal{O}(1)$.

1.3 Path-integral Monte Carlo Simulations and Results

Our simulations of the J-Q model (1.1) are based on the path-integral representation for the partition function with periodic boundary conditions in the imaginary time $0 < \tau \leq \beta$, where β denotes the inverse temperature. The path-integral Quantum Monte Carlo (PIMC) is an example of quantum Monte Carlo methods that allows us to study bosonic and non-frustrated quantum spin systems in arbitrary dimensions with very large system size without any approximation. Path-integral Monte Carlo method provides us the accurate computation of thermodynamic properties of quantum many-body systems in discrete and continuous space, at finite temperature. With the help of worm algorithm, one can perform quantum simulations in the grand canonical ensemble, as well as to compute off-diagonal imaginary-time correlation functions, such as the Matsubara Green function, simultaneously with diagonal observables. The simulations of the DCP action were performed as described in Ref. [9]. In the simulation of the classical DCP action, we also use the worm algorithm.

Accordingly, the spin stiffness ρ_{JQ} with respect to the Thouless phase-twist can be expressed in terms of the spin world-line windings W'_x, W'_y along the spatial directions x and y , respectively:

$$\rho_{JQ} = \frac{1}{2\beta}\left[\langle (W'_x)^2 \rangle + \langle (W'_y)^2 \rangle\right]. \tag{1.10}$$

In order to compare the two models at the transition point we also need to fine-tune the β/L ratio for each system size L in order to reach the space-time symmetry in the J-Q model. We achieve this by defining a space-time symmetric winding in the time direction, $W'_\tau \equiv \sum_{x,y} S_z$ (in the basis where $\hat{S}_z = S_z = \pm 1/2$ is diagonal), and requiring that its mean-square fluctuations coincide with $\langle (W'_x)^2 \rangle = \langle (W'_y)^2 \rangle$. We note that W'_τ is defined without the factor of 2 (cf. Eq.(4) of Ref.[14]). Such definition guarantees that fluctuations of W'_τ proceed in the same way as the spatial windings do—in increments of ± 1.

Thus, if parameters of both models (1.1) and (1.3) are kept at the critical point $J/Q \approx 0.04$ [10] and $t = t(g)$ (below the bicritical point) [9], the universal values of the winding number fluctuations in both models $R_{JQ} = \langle [(W'_x)^2 + (W'_y)^2 + (W'_\tau)^2] \rangle \sim \mathcal{O}(1)$ and $R = \langle [(W_x)^2 + (W_y)^2 + (W_z)^2] \rangle \sim \mathcal{O}(1)$ must coincide provided J-Q and NCCP^1 models have the same fixed point.

Finite size analysis. Simulations of both models have been conducted for a sequence of linear sizes using exactly the same definition of the pseudo-transition point in a finite size system, according to the flowgram method [8, 9]. Specifically, we tuned model parameters so that the ratio of statistical weights of configurations with and without windings, $\mathcal{F}$, equals the same constant of order unity. We have chosen $\mathcal{F} = 0.55$ because it offers the smallest deviations from the space-time symmetry in the J-Q model at large L, as shown in Fig. 1.1. The values of the parameters at the pseudo-transition points for both models are presented in Fig. 1.2.

The universality of scaling behavior is characterized by a unique function $R = \mathcal{R}(\mathcal{F})$ in the thermodynamic limit $L \to \infty$, $\beta \sim L$, i.e. for fixed $\mathcal{F} = 0.55$ one expects that $R(L)$ curves saturate to the same value even if they deviate from each other at finite L. To see if this is indeed the case we have measured R_{JQ} vs L and R vs (L, g) for several values of L (from $L = 4$ to $L = 36$ for the DCP model and from $L = 6$ to $L = 196$ for the J-Q model). Figure 1.3 shows the family of DCP flowgrams $R(L)$

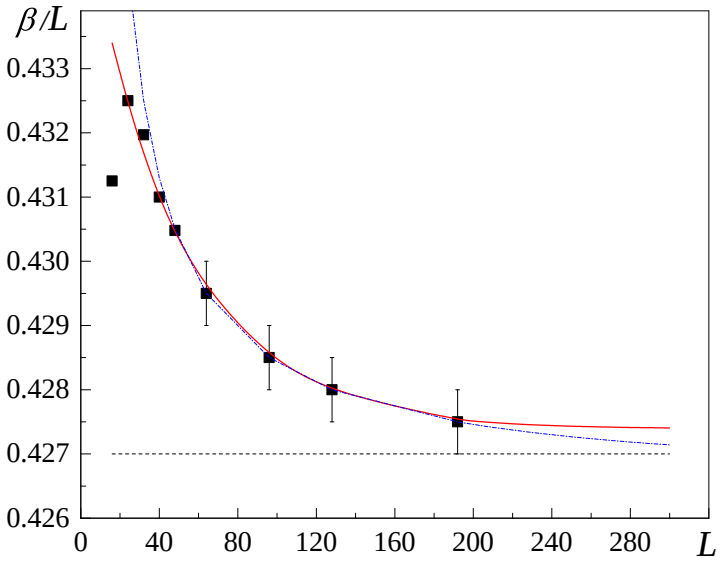

Figure 1.1. Optimal ratio $\beta(L)/L$ vs L, with the numerical data represented by dots obtained at the pseudo critical points defined in the text. Solid red line is the fit by $D + A\exp(-BL)$ and the dashed-dotted blue line is the fit by $D + B/L$, with the dashed black line representing the asymptote $\beta/L = D = 0.4270 \pm 0.0005$ corresponding to the space-time symmetry of the J-Q model.

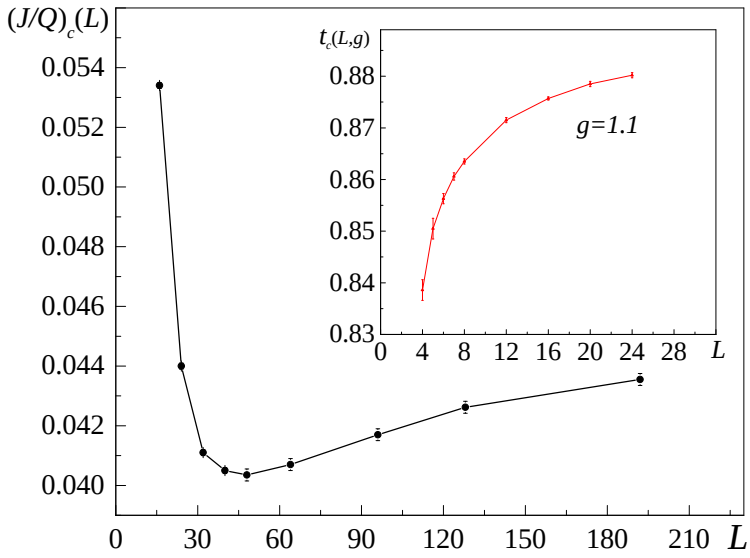

Figure 1.2. Size-dependent transition points $(J/Q)_c(L)$ of the J-Q model with the β/L ratios as in Fig. 1.1. The inset shows the pseudo-transition points $t_c(L, g)$ for $g = 1.1$ in the DCP model (1.3). Extrapolation of both curves to the $L \to \infty$ limit provides estimates of the thermodynamic transition points: $(J/Q)_c = 0.0451 \pm 0.0004$ and $t_c(g = 1.1) = 0.8822 \pm 0.0004$.

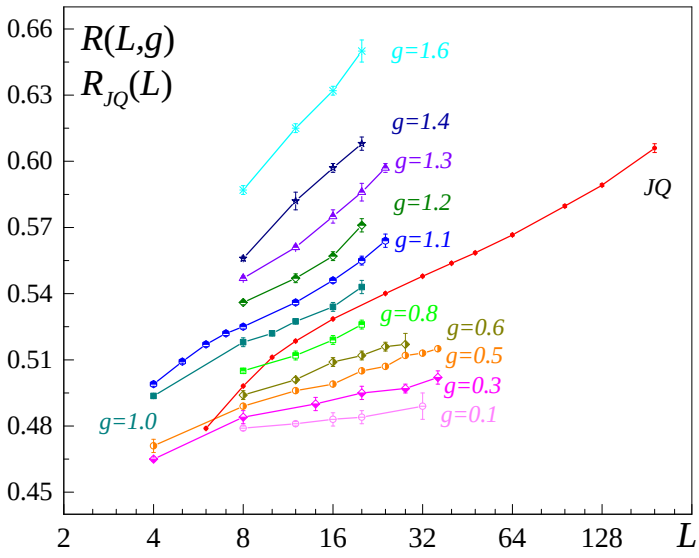

Figure 1.3. Flowgrams of the J-Q (red line) and the DCP models (for several values of g).

for several values of the interaction constant g. It also shows the flowgram $R_{JQ}(L)$ for the J-Q model. It is immediately clear that the values of R-curves overlap and all by itself this is evidence that DCP theory captures the physics of the transition point in the J-Q model. This crucial aspect as well as the fact that all the curves feature divergence with L, in violation of the scale invariance hypothesis for both models will become more evident below.

As discussed earlier in Ref. [9], the family of DCP flowgrams can be collapsed on a single master curve by rescaling system sizes as $L \to C(g)L$, where $1/C(g)$ is the distance scale as in $L/\xi(g)$. This collapse implies that properties of the DCP model at coupling strength $g = g_1$ and length scale $L = L_1$ are the same as at $g = g_2$ and $L = L_2 = L_1 C(g_1)/C(g_2)$, provided L is larger than some microscopic size ≈ 6. Figure 1.4 shows the quality of the data collapse procedure as well as the master curve which emerges from it. It also shows the flowgram of the J-Q model with rescaled distance $L \to C_{JQ}L$. The value of C_{JQ} has been adjusted in order to achieve the

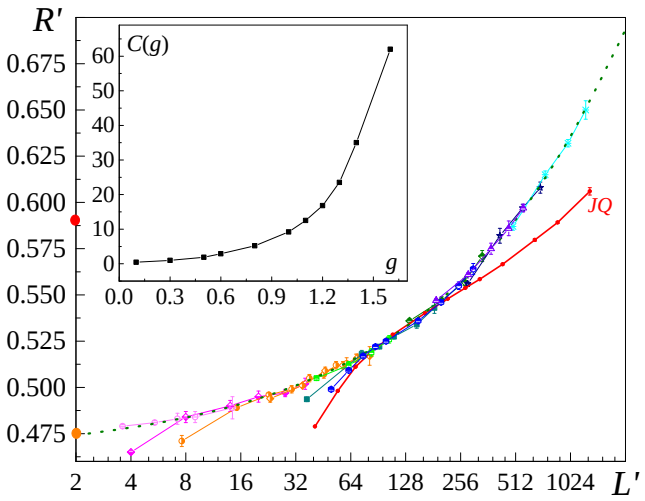

Figure 1.4. Flowgrams from Fig. 1.3 are collapsed by rescaling system sizes as $L' = C(g)L$ for the DCP model (this amounts to the horizontal shifts of the curves) and $L' = 6.8L$ for the J-Q model. Green dotted line shows the master curve fit by the $A + B(L')^{\alpha}$ function with $A = 0.463, B = 0.00823, \alpha = 0.437$. The lower (orange) dot on the R'-axis indicates the universal value $R'_{\mathrm{O}(4)} \approx 0.475$ for the O(4) universality class ($g = 0$ case). The upper (red) dot on the R' axis corresponds to the universal value $R'_{\mathrm{O}(3)} \approx 0.583$ characterizing the O(3)-universality. Inset: the rescaling function $C(g)$ such that $C(0.3) = 1$.

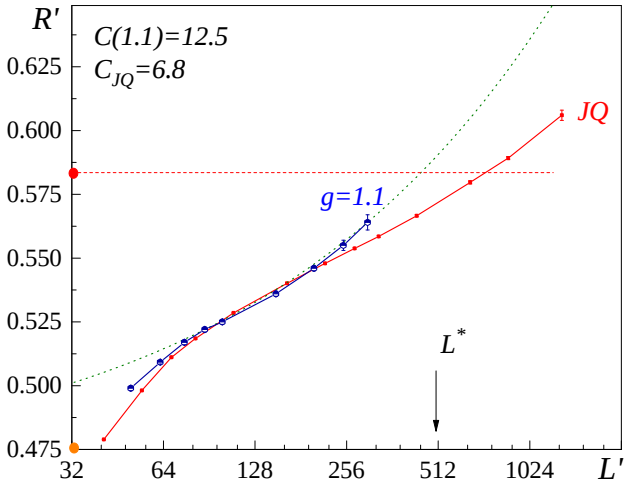

Figure 1.5. J-Q flowgram from Fig. 1.4 is shown together with the DCP $g = 1.1$ flowgram demonstrating the best overlap between the two models. The dotted line shows the master curve. The vertical arrow indicates the scale ($L^* = 75$ for the J-Q model) starting from which the flows diverge significantly. The dots on the R' axis mark the O(4) and O(3) universal values as in Fig. 1.4, with the dashed horizontal line for the O(3) asymptote.

best overlap with the DCP-master curve. Note that the freedom of choosing C_{JQ} is equivalent to shifting the R_{JQ} curve horizontally as a whole (in the $\log L$-scale), i.e. the curve's shape remains preserved. It means that the rescaling procedure is not supposed to result in the same slope at the crossing point between the two flows unless they have some common origin. As can be seen, the two curves coincide with each other at length scales $10 < L < 50$ (in terms of "bare" J-Q model sizes) before they start to diverge from each other at $L > L^* = 75$. It is also important that the J-Q flow starts from the O(4) universal value $R'_{\mathrm{O}(4)} \approx 0.475$ rather than from the O(3) universality characterized by $R'_{\mathrm{O}(3)} \approx 0.583$ as one would expect from the classical Heisenberg model, see Fig. 1.5. Finally, as Fig. 1.5 clearly shows, the J-Q flow runs past the O(3) universality at $L > L^*$.

1.4 Conclusion and Discussions

Our key finding is that the physics of the transition point between the Néel and insulating phases in the J-Q model is indeed captured by the DCP model up to a large length scale $L^* = 75$. At small sizes the flows of R and R_{JQ} start from the universal value characterizing the O(4) universality class $R'_{\mathrm{O}(4)} \approx 0.475$. This very fact is a strong indication that spinons emerge as dominant degrees of freedom in the J-Q model already at length scales $L < 8$ (in agreement with the observed U(1) symmetry of the VBS order parameters [10]). However, the divergence of the flows at $L > L^*$ unambiguously excludes the possibility that the J-Q model and the DCP action share the same criticality in the thermodynamical limit.

As shown in Ref. [9], the run-away flow of the DCP master curve ends up in the first order phase transition (detectable at $g \approx 1.65$ for sizes $L \sim 30 - 36$). [The rescaling function $C(g)$ shown in the inset in Fig. 1.4 is a smooth function defined on $g \geq 0$. It has no features indicating the presence of the tricritical point at some $g = g_{\mathrm{tr}} > 0$]. This explains why the J-Q and DCP flows ultimately depart. Given the data, there are two possibilities for the ultimate fate of the J-Q flow: either the first order transition or some unknown universality at larger values of R'. The fact that both models follow the same flow at $L < L^*$ and both violate the scale invariance hypothesis at large length scales strongly favors the first possibility—while showing quasi-universal behavior at intermediate L the two models deviate from this universality when the system size is approaching the size of the first-order nucleation bubble which does not need to be the same in different models.

CHAPTER 2

BOLD DIAGRAMMATIC QUANTUM MONTE CARLO FOR QUANTUM SPIN SYSTEMS

As stated in Chapter 1, when the spin model has a ferromagnetic coupling or it is defined on a bipartite lattice, the path-integral representation of the system's partition function will have positive weights for all the configurations, thus one can apply path-integral Monte Carlo method and obtain unbiased results very efficiently. However, a large family of spin systems that exhibit far more interesting phenomena fall out of this scenario, namely the frustrated spin systems. In frustrated spin models, the coupling is antiferromagnetic and the lattice usually consists of triangle units and therefore is not bipartite, so that the path-integral expansion of the partition function consists of sign-alternating configurations. An accurate numerical evaluation of such an integral requires extremely dense sampling of its domain, so the computational effort to solve the model increases exponentially with the number of spins.

In this chapter, we introduce another numerical method to deal with the frustrated spins, the bold diagrammatic Monte Carlo (BDMC) method, which combines the most versatile theoretical tool, Feynman diagrammatics, with the power of Monte Carlo sampling of complex configuration spaces. The simplest way of arriving at the diagrammatic technique for spins is to represent them by auxiliary fermions with imaginary chemical potential, which was first proposed by Popov and Fedotov in Ref [19]. With this representation, we can treat a frustrated spin system as a strongly-correlated fermionic system and implement skeleton formulation which leads to the BDMC approach.

2.1 Spin Fermionization

Consider the antiferromagnetic spin-1/2 Heisenberg model as an example,

$$H = \sum_{ij} J_{ij} \boldsymbol{S}_i \cdot \boldsymbol{S}_j \tag{2.1}$$

where $\boldsymbol{S}_i$ is the spin-1/2 spin operator and the interaction can happen between site i and j at any distance on arbitrary lattice in any dimension. The spin-1/2 operator can be represented as two species of auxiliary fermions

$$\boldsymbol{S}_i \to \frac{1}{2} f^\dagger_{i\alpha} \boldsymbol{\sigma}_{\alpha\beta} f_{i\beta} \tag{2.2}$$

where $f^{(\dagger)}_{i\alpha}$ is the fermionic annihilation (creation) operator with spin projection α on site i, α and β can take values ± 1 (up or down), and σ are the Pauli matrices. Here we use Einstein's summation notation. In this representation, we can write the spin-spin interaction as a two-body fermionic interaction term $\frac{1}{4} J_{ij} \boldsymbol{\sigma}_{\alpha\beta} \cdot \boldsymbol{\sigma}_{\gamma\delta} f^\dagger_{i\alpha} f_{i\beta} f^\dagger_{j\gamma} f_{j\delta}$. To solve the resulting standard two-body interacting fermionic model, one can enjoy the numerous diagrammatic techniques that have been developed over the decades.

One thing worth noting is that by representing the spin operator as auxillary fermions, we are increasing the Hilbert space from the original two states (spin up or down) at a given site to four states (0 fermion, 1 spin-up fermion, 1 spin-down fermion, 2 fermions). The states with 0 or 2 occupation number at any site are unphysical in the original model. In order to use the fermionic Hamiltonian to achieve the exactly same result, we need to eliminate the contributions of the unphysical states in the fermionic model to any physical observables we are interested in. In fact, this can be done with a simple trick first proposed by Popov and Fedotov [33, 19], who added an imaginary chemical potential to the fermionic Hamiltonian,

$$H = \sum_{ij} \frac{1}{4} J_{ij} \boldsymbol{\sigma}_{\alpha\beta} \cdot \boldsymbol{\sigma}_{\gamma\delta} f^\dagger_{i\alpha} f_{i\beta} f^\dagger_{j\gamma} f_{j\delta} - \sum_i \frac{i\pi T}{2} (\sum_\alpha f^\dagger_{i\alpha} f_{i\alpha} - 1). \tag{2.3}$$

The chemical potential term is always zero for any physical state and thus doesn't have any effect on the physical subspace. Also, in the grand canonical partition function and spin-spin correlation function, the contributions of the unphysical states exactly cancel out to zero when tracing over all the unphysical states due to the imaginary chemical potential. In a word, we have an exact mapping between the Hamiltonian in Eq. 2.3 and the original Heisenberg model in Eq. 2.1 as long as the grand canonical partition function and all the thermodynamic observables derived from it are concerned.

The non-interacting part (the second term) of the fermionic Hamiltonian is completely localized, which leaves us with the flat-band (zero-dispersion) auxiliary particles. The Green's function in this system is an artificial object which will always be localized because of the lack of hopping term in the Hamiltonian. The main observable of interest in this system is the spin-spin correlation function, which in terms of fermionic operators is the two-body correlation function,

$$\chi_{ij}(\tau) = \langle \mathcal{T} \boldsymbol{S}_i(0) \cdot \boldsymbol{S}_j(\tau) \rangle \tag{2.4}$$

$$= \boldsymbol{\sigma}_{\alpha\beta} \cdot \boldsymbol{\sigma}_{\gamma\delta} \langle \mathcal{T} f^\dagger_{i\alpha}(0)\ f_{i\beta}(0) f^\dagger_{j\gamma}(\tau) f_{j\delta}(\tau) \rangle \tag{2.5}$$

where T_τ is the imaginary time ordering operator.

2.2 Feynman Diagrams

In this section, we will apply the standard diagrammatic technique [34] and formulate the self-consistent scheme for dealing with skeleton diagrams based on fully dressed objects.

We start from the perturbative diagrammatic expansion in terms of the non-interacting Green's function (particle propagators) $G^{(0)}_{ij,\alpha\alpha'}(\tau)$ and "bare" two-body interaction lines $J_{ij,\alpha\beta\gamma\delta}$. The non-interacting Green's function in the imaginary time representation (see Fig. 2.1) is given by

$$\begin{aligned} G^{(0)}_{ij,\alpha\alpha'}(\tau) &= \langle \mathcal{T} f_{i,\alpha}(\tau) f^{\dagger}_{j,\alpha'}(0) \rangle_0 && (2.6) \\ &= \delta_{i,j}\delta_{\alpha\alpha'} G^{(0)}(\tau) && (2.7) \\ &= \delta_{i,j}\delta_{\alpha\alpha'}[\theta(\tau-\eta)\cdot\frac{e^{\mu\tau}}{1+e^{\mu\beta}} + \theta(-\tau+\eta)\cdot\frac{-e^{\mu\tau}}{1+e^{-\mu\beta}}] && (2.8) \end{aligned}$$

where $\mu = \frac{i\pi T}{2}$ is the imaginary chemical potential, and $\beta = 1/T$ is the inverse temperature. Here we take the Boltzmann constant $k_B = 1$. Since the Green's function (both "bare" and dressed) is always localized in space, we will ignore the space index in later discussions. Without external magnetic field h_z, the Green's function does not depend on the spin index. However, if we want to add a external field h_z to the Hamiltonian, namely $\mu \to \mu' = \frac{i\pi T}{2} + \alpha \cdot h_z$, the symmetry between the Green's function $G^{(0)}_{+1}(\tau)$ and $G^{(0)}_{-1}(\tau)$ will be broken and an additional spin index needs to be added. For simplicity, we ignore the external field term in our discussion.

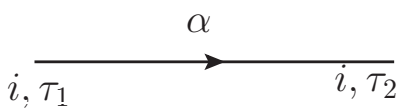

Figure 2.1. Graphical representation for the non-interacting Green's function $G^{(0)}_{ij,\alpha\alpha'}(\tau_2 - \tau_1)$.

The interaction line for the $SU(2)$-symmetric Heisenberg model can be represented as

$$J_{ij,\alpha\beta\gamma\delta}(\tau) = \frac{1}{4}J_{ij}\delta(\tau)\boldsymbol{\sigma}_{\alpha\beta}\cdot\boldsymbol{\sigma}_{\gamma\delta} \tag{2.9}$$

$$= \frac{1}{4}J_{ij}\delta(\tau)(\alpha\gamma\cdot\delta_{\alpha,\beta}\delta_{\gamma,\delta}+2\delta_{\alpha,\delta}\delta_{\alpha,-\beta}\delta_{\gamma,-\delta}) \tag{2.10}$$

where the first term in the spin dependence represents the $z-z$ interaction between sites i and j, while the second term is the spin-flip interaction, see Fig. 2.2. For more general XXZ models, the magnitudes need to be adjusted accordingly.

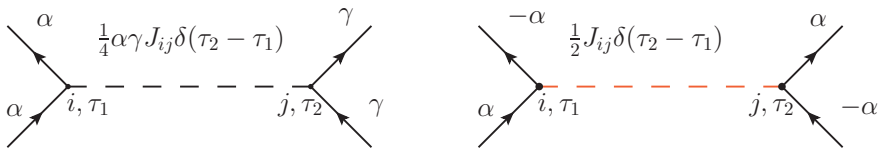

Figure 2.2. Graphical representation for the interaction line in Heisenberg model. Note that the sums of incoming and outgoing spin indices satisfy the conservation law.

Using Wick's theorem, the perturbation expansion for the grand potential $\Omega = F-\mu N = -T\ln\mathcal{Z}$ can be represented in terms of diagrammatic series of connected diagrams. An order-n diagram can be constructed using the following rules (see Fig. 2.3):

1. Draw n interaction lines (Fig. 2.2) and connect all the $2n$ vertexes by directed propagator lines (Fig. 2.1). Make sure that the diagram only has one connected component.

2. Assign a space variable r_i and a time variable τ_i for each vertex, and a spin index for each propagator line. Note that the spin indices must satisfy the conservation law at each interaction line, otherwise the contribution would be zero.

3. Each propagator line is associated with factor $G^{(0)}_{ij,\alpha}(\tau_j - \tau_i)$; while each interaction line is associated with factor $J_{ij,\alpha\beta\gamma\delta}(\tau_j - \tau_i)$.

4. Multiply all the factors from interaction lines and propagators, then multiply by $(-1)^n(-1)^{n_L}$, where n_L is the number of closed loops formed by propagators (Fermi loops).

5. By summing over the spin indices and space variables, and integrating over imaginary time $\{\tau_i\}$, we can obtain the contribution of this order-n diagram to the grand potential Ω.

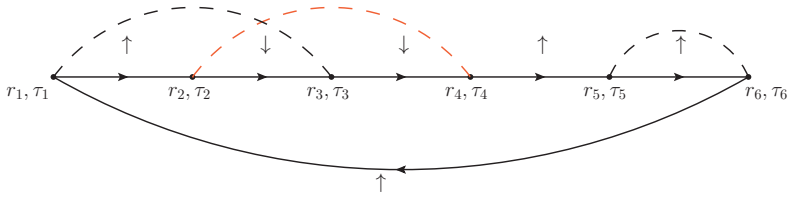

Figure 2.3. An example of 3rd-order diagram in terms of bare propagator lines and interaction lines. Each propagator has a spin index, while each vertex has a space and imaginary time variable.

The fully dressed propagator G of Hamiltonian 2.3 is defined as follows.

$$G_{ij,\alpha\alpha'}(\tau) = \langle \mathcal{T} f_{i,\alpha}(\tau) f^{\dagger}_{j,\alpha'}(0) \rangle \tag{2.11}$$

It can be expanded in terms of the bare propagator $G^{(0)}$ and interaction J as in Fig. 2.4.

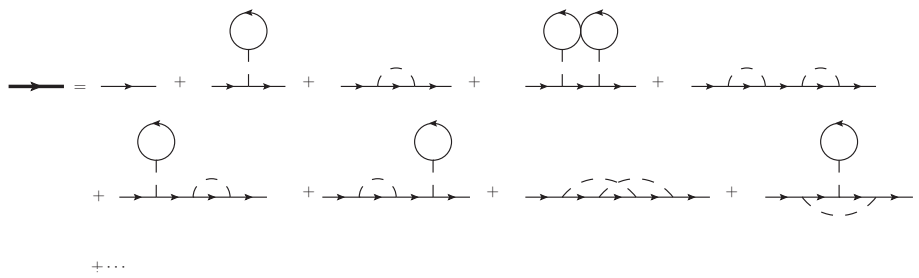

Figure 2.4. The bare series expansion for the fully dressed propagator G. We use bold directed line to represent the fully dressed propagator, while the thin directed line denotes the non-interacting propagator and the dash line denotes the interaction line.

The observable we are most interested is the spin susceptibility function $\chi(\mathbf{r}, \tau)$ (Eq. 2.4). The bare series expansion for the susceptibility is as shown in Fig. 2.5.

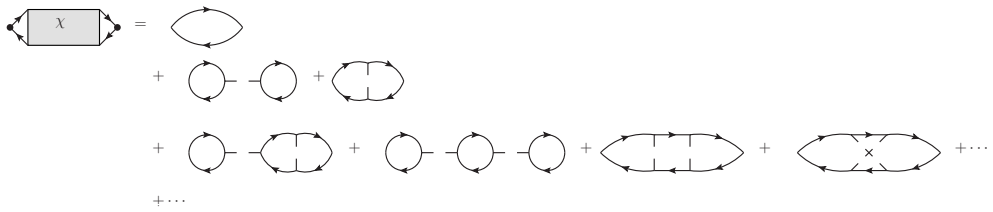

Figure 2.5. The bare Feynman diagram expansion for the spin susceptibility function χ.

2.3 G^2W-skeleton Expansion

The diagrammatic representation in terms of free fermionic fields has a big advantage, which is that except for the alternating sign, there are no other prefactors depending on the diagram topology or diagram orders. This allows one to apply self-consistent equations to deal with certain subsets of diagrams that consist of repeated blocks. In this section, we will introduce one simple self-consistent formulation, which is known as the G^2W-skeleton scheme.

In the G^2W-skeleton technique, one identifies the "irreducible" self-energy-type blocks which consist of diagrams where all vertexes remain connected by some path when one removes any two lines of the same kind: either two propagator lines with the same spin index or two interaction lines. The rest of diagrams ("reducible" ones) are fully accounted for by replacing bare propagators and interaction lines in the irreducible blocks with fully-dressed propagators, $G(\tau)$, and screened interactions, $W(\boldsymbol{r}, \tau)$. The resulting formulation is self-consistent and highly non-linear, since G and W depend on the self-energy-type blocks through the Dyson type equations. Usually, we call the irreducible block for the particle propagator as self-energy Σ, and the block for the interaction line as Π (better known as the polarization operator). The diagram series of G and W can be defined from the self-consistent loop shown in 2.6. Note that we divide the bold interaction line W into two parts: the bare interaction J which is a delta function of imaginary time τ and the rest part $\Delta W = W - J$, a continuous function of τ.

In order to simplify the calculation in the Dyson and screening equation, we can Fourier transform the functions in the (r, τ) representation into $(k, i\omega_n)$ representation. We discretize the imaginary time variables into N bins ($\tau_i = (i - \frac{1}{2})\frac{\beta}{N}$ for $i = 1, 2, \cdots, N$) and perform the discrete Fourier transformation on $G(\tau_n)$, $J(\mathbf{r})$, $\Delta W(\mathbf{r}, \tau_n)$, $\Sigma(\tau_n)$, and $\Pi(\mathbf{r}, \tau_n)$. Note that due to the anti-periodic/periodic nature of the propagator and interaction function, the definition of Matsubara frequency for

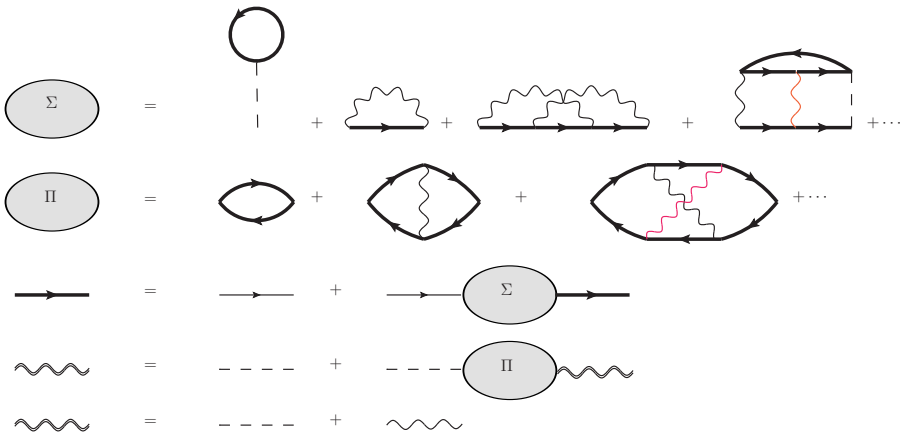

Figure 2.6. We use bold directed lines to represent dressed propagators G, double wavy lines to represent screened interaction lines W, and single wavy lines to represent $\Delta W = W - J$. The thin directed lines and dashed lines are the bare propagators $G^{(0)}$ and bare interactions J. The first two equations give some lower order examples for the irreducible blocks Σ and Π. The third and fourth equations are the self-consistent equations (Dyson equation and screening equation) that define the bold propagator and interaction lines in terms of the irreducible blocks.

$G^{(0)}$, G and Σ is $\omega_n = 2\pi(n + \frac{1}{2})/\beta$, while the Matsubara frequency for ΔW and Π is defined as $\omega_n = 2\pi n/\beta$.

$$G(i\omega_n) = \sum_{i=1}^{N} G(\tau_i) e^{-i\omega_n \tau_i} \qquad \omega_n = 2\pi(n + \frac{1}{2})/\beta \tag{2.12}$$

$$\Sigma(i\omega_n) = \sum_{i=1}^{N} \Sigma(\tau_i) e^{-i\omega_n \tau_i} \qquad \omega_n = 2\pi(n + \frac{1}{2})/\beta \tag{2.13}$$

$$J(\mathbf{k}) = \sum_{\mathbf{r}} J(\mathbf{r}) e^{-i\mathbf{k}\cdot\mathbf{r}} \tag{2.14}$$

$$\Delta W(\mathbf{k}, i\omega_n) = \sum_{i=1}^{N} \sum_{\mathbf{r}} \Delta W(\mathbf{r}, \tau_i) e^{-i\mathbf{k}\cdot\mathbf{r}} e^{-i\omega_n \tau_i} \qquad \omega_n = 2\pi n/\beta \tag{2.15}$$

$$\Pi(\mathbf{k}, i\omega_n) = \sum_{i=1}^{N} \sum_{\mathbf{r}} \Pi(\mathbf{r}, \tau_i) e^{-i\mathbf{k}\cdot\mathbf{r}} e^{-i\omega_n \tau_i} \qquad \omega_n = 2\pi n/\beta \tag{2.16}$$

In the momentum–Matsubara-frequency representation, the Dyson and screening equations can be written as

$$G(i\omega_n) = \frac{G^{(0)}(i\omega_n)}{1 - G^{(0)}(i\omega_n)\Sigma(i\omega_n)} \tag{2.17}$$

$$\Delta W(\mathbf{k}, i\omega_n) = \frac{J(\mathbf{k})}{1 - J(\mathbf{k})\Pi(\mathbf{k}, i\omega_n)} - J(\mathbf{k}) = \frac{J(\mathbf{k})\Pi(\mathbf{k}, i\omega_n)J(\mathbf{k})}{1 - J(\mathbf{k})\Pi(\mathbf{k}, i\omega_n)} \tag{2.18}$$

As mentioned in Sec. 2.1, the main observable of interest for a spin system is the spin-spin correlation function $\chi(\mathbf{r}, \tau)$ (Eq. 2.4). In the G^2W-skeleton scheme, the spin-spin correlation function can also be constructed self-consistently from the polarization operator Π.

Let us first write down the spin-spin correlation function in a more general form where a breaking of the spin rotational symmetry may exist,

$$\begin{aligned}
\chi_{ij}(\tau_1, \tau_2) &= \langle \mathbf{S}_i(\tau_1) \cdot \mathbf{S}_j(\tau_2) \rangle - \langle \mathbf{S}_i(\tau_1) \rangle \cdot \langle \mathbf{S}_j(\tau_2) \rangle \\
&= (\langle \mathcal{T} f^\dagger_{i\alpha}(\tau_1) f_{i\beta}(\tau_1) f^\dagger_{j\gamma}(\tau_2) f_{j\delta}(\tau_2) \rangle - \langle \mathcal{T} f^\dagger_{i\alpha}(\tau_1) f_{i\beta}(\tau_1) \rangle \langle \mathcal{T} f^\dagger_{j\gamma}(\tau_2) f_{j\delta}(\tau_2) \rangle) \boldsymbol{\sigma}_{\alpha\beta} \cdot \boldsymbol{\sigma}_{\gamma\delta} \\
&\equiv \chi_{ij,\alpha\beta\gamma\delta}(\tau_1, \tau_2)\ \boldsymbol{\sigma}_{\alpha\beta} \cdot \boldsymbol{\sigma}_{\gamma\delta}
\end{aligned} \tag{2.19}$$

It is obvious to see that the operator $\chi_{ij,\alpha\beta\gamma\delta}(\tau_1, \tau_2)$ is directly related to the one-body and two-body propagator G and G_2 as follows:

$$G(1; 1') = \langle \mathcal{T} \psi(1) \psi^\dagger(1') \rangle \tag{2.20}$$

$$G_2(1, 2; 1', 2') = \langle \mathcal{T} \psi(1) \psi(2) \psi^\dagger(1') \psi^\dagger(2') \rangle \tag{2.21}$$

$$\begin{aligned}
\chi_{i_1 i_2, \alpha_1 \alpha_1' \alpha_2 \alpha_2'}(\tau_1, \tau_2) &\equiv \chi(1, 2; 1^+, 2^+) \\
&= G_2(1, 2; 1^+, 2^+) - G(1, 1^+) G(2, 2^+)
\end{aligned} \tag{2.22}$$

In the equations above, we use the Grassmann field ψ to replace the fermionic operator $\hat{f}$. To simplify the notation, we use a single number j to represent the corresponding space, spin, and imaginary time variable (i_j, α_j, τ_j). For example, $\psi(1)$ represents $\psi_{i_1,\alpha_1}(\tau_1)$. Fig. 2.7 shows a diagrammatic representation of $\chi(1, 2; 1^+, 2^+)$.

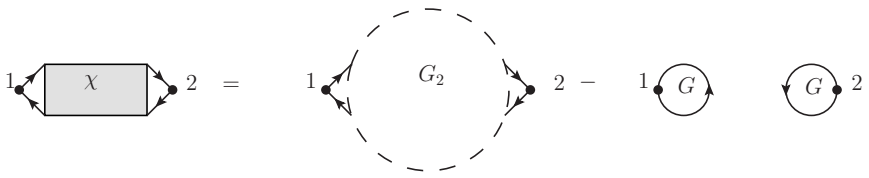

Figure 2.7. The diagrammatic representation of $\chi(1, 2, 1^+, 2^+)$. It contains all the possible connected diagrams with two external points 1 and 2.

We can also identify the "irreducible" block in χ which consists of diagrams where all vertexes remain connected when one removes any two interaction lines. It can be shown that the irreducible block of χ is nothing but the polarization operator Π. Therefore, the spin-spin correlation $\chi(1, 2; 1^+, 2^+)$ can be constructed self-consistently from the polarization Π:

Figure 2.8. The self-consistent construction of magnetic susceptibility χ in terms of polarization Π and bare interaction J.

If we perform the Fourier transformation to the momentum–Matsubara-frequency representation, the equation becomes

$$\chi(\mathbf{k}, i\omega_n) = \frac{\Pi(\mathbf{k}, i\omega_n)}{1 - J(\mathbf{k})\Pi(\mathbf{k}, i\omega_n)} \tag{2.23}$$

In the bold diagrammatic Monte Carlo (BDMC) method, we apply Monte Carlo sampling to calculate the irreducible self-energy $\Sigma^{(n)}$ and polarization $\Pi^{(n)}$ up to a fixed maximum diagram order n, given functions G and W. Then we plug $\Sigma^{(n)}$ and $\Pi^{(n)}$ into the Dyson and screening equations (Eq. 2.17) to calculate a new G and W, and carry out Monte Carlo sampling again, until convergence. At the same time, given a polarization $\Pi^{(n)}$, we can calculate the corresponding spin-spin correlation function $\chi^{(n)}$ using the self-consistent equation 2.23.

With the spin-spin correlation function, we can derive the static structure factor $\mathcal{S}(\mathbf{q})$ of the system based on the following equation

$$\begin{aligned}
\mathcal{S}(\mathbf{q}) &= \langle \mathbf{S}(\mathbf{q}) \cdot \mathbf{S}(-\mathbf{q}) \rangle \\
&= \sum_{\mathbf{r}} \langle \mathbf{S}_0 \cdot \mathbf{S}_{\mathbf{r}} \rangle e^{-i\mathbf{q}\cdot\mathbf{r}} \\
&= \sum_{\mathbf{r}} \int d\tau \chi(\mathbf{r}, \tau) e^{-i\mathbf{q}\cdot\mathbf{r}} \\
&= \chi(\mathbf{q}, i\omega_n = 0)
\end{aligned} \tag{2.24}$$

Moreover, the BDMC method can provide the structure factor on the whole Matsubara frequency curve $\mathcal{S}(\mathbf{q}, i\omega_n)$. It allows us to apply analytical continuation methods [35, 36] to achieve the real frequency dynamic structure factor $\mathcal{S}(\mathbf{q}, \omega)$, which is a quantity that can be directly measured in inelastic neutron scattering experiments. The real and Matsubara frequency functions are related to each other by the standard linear-response theory relation

$$\mathcal{S}(\mathbf{q}, i\omega_n) = \frac{1}{\pi} \int_0^\infty \frac{(1 - e^{-\beta\omega})}{\omega_n^2 + \omega^2} \mathcal{S}(\mathbf{q}, \omega) d\omega \tag{2.25}$$

2.4 Diagrammatic Monte Carlo Method with Worm Algorithm

With the self-consistent formulation, now the task at hand is to calculate the infinite skeleton diagram series for Σ and Π. To fit the problem in the general Diagrammatic Monte Carlo framework [37, 38], we can formulate the problem as computing the quantity $Q(y;l)$ (where y is the space, imaginary time and spin variables of the function, and $l = 1, 2$ labels whether this function is Σ or Π). The quantity $Q(y;l)$ is a series of multidimensional sums/integrals

$$Q(y;l) = \sum_n \sum_{\xi_n} \int dx_1 dx_2 \cdots dx_n dY \mathcal{D}(n, \xi_n, \{x_i\}, Y, l)\delta(y - Y) \tag{2.26}$$

where $n = 1, 2, \cdots$ is the diagram order, ξ_n is the index for the different terms at order n, $\{x_i\}$ are the internal space, imaginary time and spin indices in the sum/integrals, Y are the external variables, $\mathcal{D}$ is the contribution of the diagram to the quantity ($l = 1$ for Σ, $l = 2$ for Π). Since it's more convenient to use the same diagrammatic representation for both Σ and Π, we use the diagrams for free-energy and set one of the propagators or interaction lines as "dummy" line to represent the self-energy (with one dummy propagator) or polarization (with one dummy interaction) sectors.

The Diagrammatic Monte Carlo approach is a stochastic approach which samples the configurations in the space $\{\nu\} = \{n, \xi_n, \{x_i\}, Y, l\}$ with corresponding weights $|\mathcal{D}_\nu| = |\mathcal{D}(n, \xi_n, \{x_i\}, Y, l)|$, and calculates the average of function $\delta(y, Y)e^{iarg(\mathcal{D})}$ over the sample to estimate the quantity in Eq. 2.26.

$$\begin{aligned} Q(y;l) &= \sum_\nu |\mathcal{D}_\nu| e^{iarg(\mathcal{D}_\nu)} \delta(y, Y) && (2.27) \\ &\propto C_l \sum_\nu P_{\nu,l}\ e^{iarg(\mathcal{D}_\nu)} \delta(y, Y) && (2.28) \\ &\to C_l \sum_{\nu_{MC}} e^{iarg(\mathcal{D}_\nu)} \delta(y, Y) && (2.29) \end{aligned}$$

In the equation above, the probability density function of each configuration ν is defined as $P_{\nu,l} = |\mathcal{D}_\nu|/C_l$, where C_l is the normalization factor. The averaging over all the configurations can be estimated by the average over the Markov-Chain Monte Carlo sampling ν_{MC} generated from the probability distribution $P_{\nu,l}$.

There are several different ways to calculate the normalization factor [16]. In this thesis, we choose to add a special "normalization" configuration ν_0 to the configuration space $\{\nu\}$. The normalization diagram doesn't have any external and internal variables and it has weight $Q_0(l) = 1$. Then the ratio $Q(y;l)/Q_0(l)$ can be measured in the MC simulation as

$$Q(y;l)/Q_0(l) = \sum_{\nu_{\mathrm{MC}},\nu_{\mathrm{MC}}\neq\nu_0} e^{iarg(\mathcal{D}_\nu)}\delta(y,Y)/\sum_{\nu_{\mathrm{MC}},\nu_{\mathrm{MC}}=\nu_0} 1 \tag{2.30}$$

2.4.1 Worm Algorithm

We now can proceed with the Markov-Chain Monte Carlo sampling scheme which allows us to explore all the configurations $\nu = (n, \xi_n, \{x_i\}, Y, l)$ with probability density function $P_{\nu,l}$. Note that we do not only need to use MC sampling for the integral and summation of the space and time variables but also need to stochastically sample different diagram topology structures at different diagram orders. Moreover, the skeleton diagrams have an extra constraint about irreducibility, requiring that removing any two propagator lines or interaction lines does not result in a disconnected graph.

In order to deal with irreducibility, we introduce an auxiliary momentum to each propagator line and interaction line, and ensure a momentum conservation law at each vertex as shown in Fig. 2.9. If two lines of the same kind have the same momentum, then cutting these two lines will divide the diagram into two pieces. Therefore we can use Hash tables to store momenta for propagator and interaction lines separately, and perform a check at each MC update to ensure the irreducibility for both types of lines.

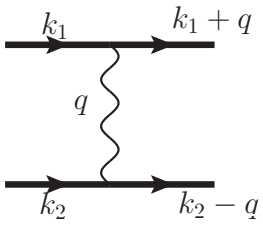

Figure 2.9. An illustration of the momentum conversation law. The difference between the momenta on the incoming and outgoing propagator lines is always the same as the momentum on the interaction line (undirected) connected to them, namely $|k_{in} - k_{out}| = |q|$.

Since the trick with auxiliary momenta is based on momentum conservation laws, a valid update scheme can be either (i) performing non-local updates on closed loops, or (ii) extending the configuration space to include diagrams which violate these conservation laws. The second strategy is the essence of the worm algorithm. By enlarging the configuration space, worm algorithm allows one to carry out local updates that are much easier to implement and have higher acceptance ratio. One more reason for using the worm algorithm approach is the spin projection conservation law in the interaction process, see Eq. 2.9 and Fig. 2.2. It also requires that updates are performed only on closed loops of interaction lines and propagators, unless one enlarges the configuration space to include diagrams which violate the spin conservation law. It turns out that the worm algorithm can be generalized to take care of both conservation laws at the same time [16].

The essence of worm algorithm is to introduce two types of configurations (diagrams) in the configuration space, one type is the physical configurations we discussed above (also including the normalization configuration), the other is the additional unphysical diagrams. The physical diagrams satisfy both momentum and spin projection conservation laws. However, the unphysical diagrams have two special vertexes, I and M, where momentum and spin conservation laws are violated, see Fig. 2.10. The other vertexes still satisfy conservation laws. The special vertexes represent a drain (I) and

a source (M) of momentum p_w and spin projection $d\alpha = 2$, see Figs. 2.10. Note that the spin conservation law is formulated on a pair of vertexes connected by the same interaction line, i.e. an interaction line containing a worm on one of its ends is unphysical and the weight function for this unphysical line is a function independent of spin indices, $J_{unphy}(r)$ or $\Delta W_{unphy}(r, \tau)$ depending on whether the interaction line is a dashed or a wavy line.

With the definition of these special vertexes, one can construct a set of local updates that can move the special vertexes around, update the momentum and spin indices along the way, and at the same time update the topology and diagram order. When the two special vertexes meet at the same point, the configuration comes back to the physical subspace with conservation laws on all the vertexes. Only the physical configurations will contribute to the measurement of the Σ and Π functions.

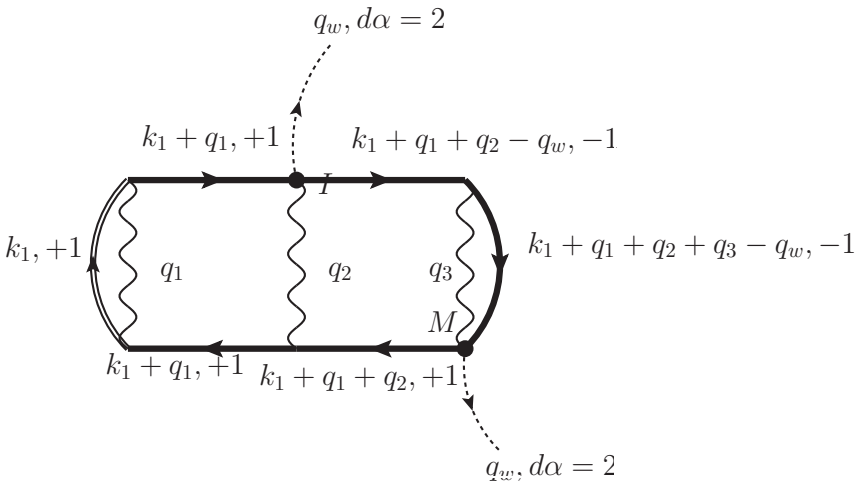

Figure 2.10. One example of an unphysical diagram of order 3. The space and imaginary time variables are neglected. The black dots represent the two special vertexes I and M, which breaks the conservation law for momentum and spin. It can be interpreted as there's a hypothetical line from I to M with a flow of momentum q_w and spin projection 2. The directed double line is the dummy measuring line, which indicates that this diagram is one of the self-energy diagrams.

2.4.2 Updates

In this subsection, we describe an ergodic set of updates to explore the enlarged configuration space of both the physical diagrams and unphysical diagrams. Before we jump to the details of the updates, first let us summarize the structure of the configuration space. The diagrams of order-n contain $2n$ propagator lines, n interaction lines, and $2n$ vertexes. There are two types of interaction lines, the bare interaction J and screened time-dependent interaction ΔW. In the following discussion, for simplicity, we use W to denote the weight for any type of W lines if not specifically stated. Among all the $3n$ lines, there's one "dummy" or "measuring" line (with unity weight) indicating whether this diagram is contributing to self-energy or polarization. The normalization configuration is referred to as order-0 diagram which doesn't have any structures. See Fig. 2.11 as an example.

Figure 2.11. Two examples of configurations of order-3. The first one is a physical diagram which has a measuring propagator line (double line) and contributes to the measurement of self-energy Σ. The second diagram is an unphysical diagram with a measuring interaction line (double line). This diagram doesn't contribute to any measurement because of the existence of the worm.

Below we describe an ergodic updating scheme which contains 15 different updates. At each MC step, one randomly select one of the 15 updates with probability P^c_{update}. Each update performs a Metropolis-Hastings type algorithm to generate a new configuration based on the current state. Metropolis-Hastings algorithm consists of the following stages:

1. start from the current configuration x, propose a new configuration x' with a certain probability $P^p(x \to x')$

2. calculate the acception ratio $R(x \to x') = \frac{|\mathcal{D}(x')|}{|\mathcal{D}(x)|} \frac{P^p(x' \to x)}{P^p(x \to x')}$, where $\mathcal{D}(x)$ is the weight of the diagram x

3. accept the new state x' with probability $\min(1, R(x \to x'))$, otherwise reject and copy the old configuration x as the new x'.

Create-Worm – Delete-Worm

The pair of complementary updates *Create-Worm–Delete-Worm* switches between physical and unphysical sectors by inserting/removing a pair of special vertexes connected by an interaction line, as shown in Fig. 2.12. The special vertexes will break the momentum conservation law at the two vertexes. However, since the spin conservation is defined with respect to both ends of the interaction line, the spin conservation law is still satisfied on the selected interaction line even when there are two special vertexes at its both ends.

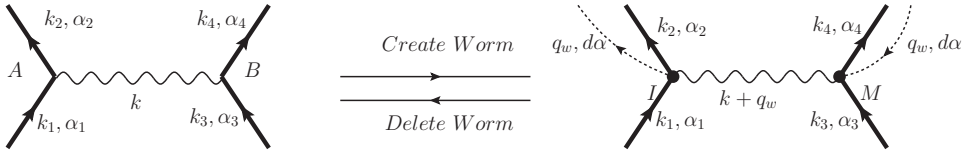

Figure 2.12. The *Create-Worm/Delete-Worm* updates that insert/remove a pair of worms I and M at the ends of an interaction line. The interaction line can be either wavy line or dash line.

When inserting the special vertexes I and M, we need to randomly chose the interaction line from the $2n$ lines in the diagram. We also need to choose the value of spin flow $\delta\alpha = \pm 2$. The momentum variables don't enter the weight of the diagram, therefore we don't include the probability of choosing the momentum flow in the proposal probability. Therefore, the proposal probability for *Create-Worm* is

$$\mathcal{P}^p_{cw} = \mathcal{P}^c_{cw} \frac{1}{2n} \tag{2.31}$$

The proposal probability for *Delete-Worm* , which merges I and M along the interaction line, is

$$\mathcal{P}^p_{dw} = \mathcal{P}^c_{dw} \tag{2.32}$$

The pseudo-code for *Create-Worm* and *Delete-Worm* is listed below.

Algorithm 1 Create Worm

procedure CREATEWORM
  if worm exists **then return**
  Choose a random interaction line r. $i = \text{LeftVertex}(r)$, $j = \text{RightVertex}(r)$.
  Randomly choose q_w.
  Randomly choose $\delta\alpha = +2$ or -2.
Propose to:
  update the momentum $k(r)$, $k(r) \to k(r) + q_w$.
  create I and M on i and j.

  if is-reducible() **then return**
acceptance probability:

$$\begin{aligned} \mathcal{P}^a_{cw} &= min\Big(1, \frac{|D(new)| \cdot \mathcal{P}^p_{dw}}{|D(old)| \cdot \mathcal{P}^p_{cw}}\Big) = min\Big(1, \Big|\frac{D(new)}{A(old)}\Big| \cdot 2n \cdot \frac{\mathcal{P}^c_{dw}}{\mathcal{P}^c_{cw}}\Big) \\ &= min\Big(1, \Big|\frac{W_{\text{unphys}}(I \Leftrightarrow M)}{W(r)}\Big| \cdot 2n \cdot \frac{\mathcal{P}^c_{dw}}{\mathcal{P}^c_{cw}}\Big) \end{aligned} \tag{2.33}$$

  if $rand() \leq \mathcal{P}^a_{cw}$ **then**
    update the momentum on the line
    place I and M on proper places
    keep track of the phase factor based on $D(new)/D(old)$

Algorithm 2 Delete Worm

procedure DELETEWORM
  if no worm **then return**
  if W-line(I)!=W-line(M)) **then return**
  r = W-line(I)
Propose to:
  delete I and M.
  update the momentum of r: $k(r) \to k(r) \pm q_w$.

  if is-reducible() **then return**
acceptance probability:

$$\begin{aligned} \mathcal{P}^a_{dw} &= min\Big(1, \Big|\frac{D(new)}{D(old)}\Big| \frac{1}{2n} \frac{\mathcal{P}^c_{cw}}{\mathcal{P}^c_{dw}}\Big) \\ &= min\Big(1, \Big|\frac{W(r)}{W_{\text{unphys}}(I \Leftrightarrow M)}\Big| \frac{1}{2n} \frac{\mathcal{P}^c_{cw}}{\mathcal{P}^c_{dw}}\Big) \end{aligned} \tag{2.34}$$

  if $rand() \leq \mathcal{P}^a_{dw}$ **then**
    delete I and M
    update the momentum of r
    keep track of the phase factor based on $D(new)/D(old)$

Move-Worm-On-G

Move-Worm-On-G is a self-complenmentary update. It proposes to move I between the vortexes of the diagram along the propagator lines, while updating the momenta and spins on the G-lines that I passed through. Examples are shown in Fig. 2.13. A constraint of the update is that *Move-Worm-On-G* cannot bring I and M together.

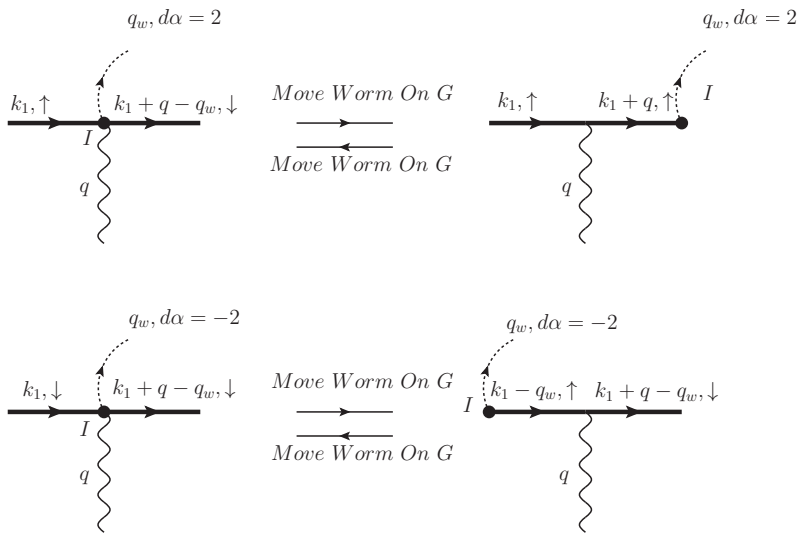

Figure 2.13. Two examples of the *Move-Worm-On-G* update that moves a worm I along a propagator line.

Algorithm 3 Move-Worm-On-G

procedure MoveWormOnG
  if no worm **then return**
  Randomly pick up one of the two G-lines connected to vertex I, and denote the other end of the selected G-line as I'.
  if $I' == M$ **then return**
  if (I ==Start(I–I') and $\delta\alpha == 2$)or(I ==End(I–I') and $\delta\alpha == -2$) **then**
    if Sp(I–I')!=-1 **then return**
  else
    if Sp(I–I')!=1 **then return**
Propose to:
  move I along I–I' to I'
  add to I–I' an additional momentum: q_w to $I \to I'$; $-q_w$ to $I' \to I$
  flip the spin of I–I'
  if is-reducible() **then return**
acceptance probability:

$$\mathcal{P}^a_{mwg} = min\Big(1, \Big|\frac{D(new)}{D(old)}\Big|\Big) = min\Big(1, \Big|\frac{W(W - line(I))W_{\text{unphys}}(W - line(I'))}{W(W - line(I'))W_{\text{unphys}}(W - line(I))}\Big|\Big) \tag{2.35}$$

  if $rand() \leq \mathcal{P}^a_{mwg}$ **then**
    move I to I'
    update the momentum of the line I–I'
    update the spin of the line I–I'
    keep track of the phase factor

Move-Worm-On-W

Move-Worm-On-W is a self-complenmentary update. It proposes to move I along the interaction line, and updates the momentum on the line I passed through, as shown in Fig. 2.14. A constraint of the update is that *Move-Worm-On-W* cannot bring I and M together.

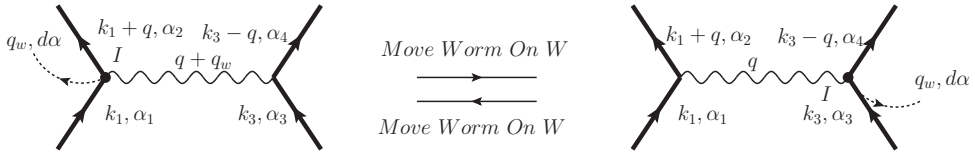

Figure 2.14. An illustration of the *Move-Worm-On-W* update that moves a worm I along the interaction line (either a wavy or a dashed line).

Algorithm 4 Move-Worm-On-W

procedure MOVEWORMONW
  if no worm **then return**
  Denote the other end of the interaction line attached to I as I'.
  if $I' == M$ **then return**
Propose to:
  move I along W-line $I \Leftrightarrow I'$ to I'
  add to $I \Leftrightarrow I'$ an additional momentum: add q_w to $I \Rightarrow I'$ or add $-q_w$ to $I' \Rightarrow I$

  if is-reducible() **then return**
acceptance probability:

$$\mathcal{P}^a_{mww} = min\Big(1, \Big|\frac{D(new)}{D(old)}\Big|\Big) = min\Big(1, \Big|\frac{W_{\text{unphys}}(I \Leftrightarrow I')}{W_{\text{unphys}}(I \Leftrightarrow I')}\Big|\Big) = 1 \tag{2.36}$$

  if $rand() \leq \mathcal{P}^a_{mww}$ **then**
    move I to I'
    update the momentum of the line $I \Leftrightarrow I'$
    keep track of the phase factor

Reconnect

Reconnect is a self-complementary update. It proposes to reconnect the incoming or outgoing propagator lines of I and M as shown in Fig. 2.15. This update allows the MC sampling to jump between all the different diagrams of the same order. It can be shown that the diagram before and after a *Reconnect* update always have number of Fermi loops differing by 1.

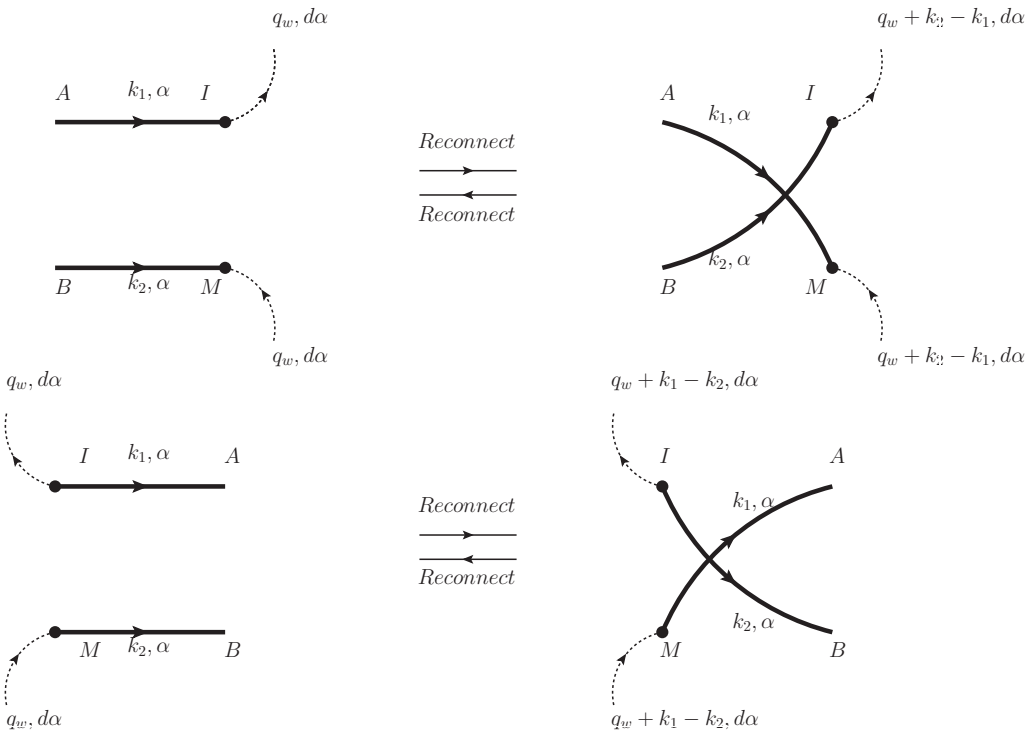

Figure 2.15. Two cases in the *Reconnect* update that reconnect the two incoming or outgoing propagator lines connected to the worm ends I and M.

Algorithm 5 Reconnect

procedure RECONNECT
  if no worm **then return**
  if $(GX(I)$!= $GX(M))$ or $(GY(I)$!= $GY(M))$ **then return**
  Choose direction (incoming or outgoing) with the same probability.
Propose to:
  if incoming **then**
    change the topology $I \leftarrow A$, $M \leftarrow B$ to $I \leftarrow B$,$M \leftarrow A$
    update the momentum q_w to $q_w + k_{M \leftarrow B} - k_{I \leftarrow A}$
    if $\mathrm{Sp}(I \leftarrow A)$!= $\mathrm{Sp}(M \leftarrow B)$ **then return**
  else
    change the topology $I \rightarrow A$, $M \rightarrow B$ to $I \rightarrow B$, $M \rightarrow A$
    update the momentum q_w to $q_w - k_{M \rightarrow B} + k_{I \rightarrow A}$
    if $\mathrm{Sp}(I \rightarrow A)$!= $\mathrm{Sp}(M \rightarrow B)$ **then return**
acceptance probability:

$$\mathcal{P}^a_{rc} = min\Big(1, \Big|\frac{D(new)}{D(old)}\Big|\Big) = min\Big(1, \Big|(-1) \cdot \frac{G(A-M)G(B-I)}{G(A-I)G(B-M)}\Big|\Big) \tag{2.37}$$

  if $rand() \leq \mathcal{P}^a_{rc}$ **then**
    update the topology
    update the momentum q_w
    keep track of the phase factor

Add-Interaction – Remove-Interaction

Add-Interaction and *Remove-Interaction* are a pair of complenmentary updates, which change the diagram order, as shown in Fig. 2.16. This pair of updates adds/removes a wavy interaction line ΔW to/from the diagram.

When adding a new interaction line to the diagram, we need to first randomly pick a direction (incoming or outgoing) and then randomly generate new imaginary time variables for the two new vertexes. Therefore, the proposal probability for *Add-Interaction* is

$$\mathcal{P}^p_{ai} = \frac{1}{2}\mathcal{P}^c_{ai} P_t(t_A) P_t(t_B) dt^2 \tag{2.38}$$

The proposal probability for *Remove-Interaction* is

$$\mathcal{P}^p_{ri} = \frac{1}{2}\mathcal{P}^c_{ri} \tag{2.39}$$

Meanwhile, the ratio between the weights of old and new diagrams is

$$\frac{D(new)}{D(old)} = (-1) \cdot \frac{G(I-A)G(A-C)G(M-B)G(B-D)W(A \Leftrightarrow B)dt^2}{G(I-C)G(M-D)} \tag{2.40}$$

In the final expression of the acceptance probability, the term dt^2 will cancel out which leaves us a finite probability. Note that adding or deleting an interaction line will change the diagram order by 1 which will gives us an extra -1 factor for the weight ratio.

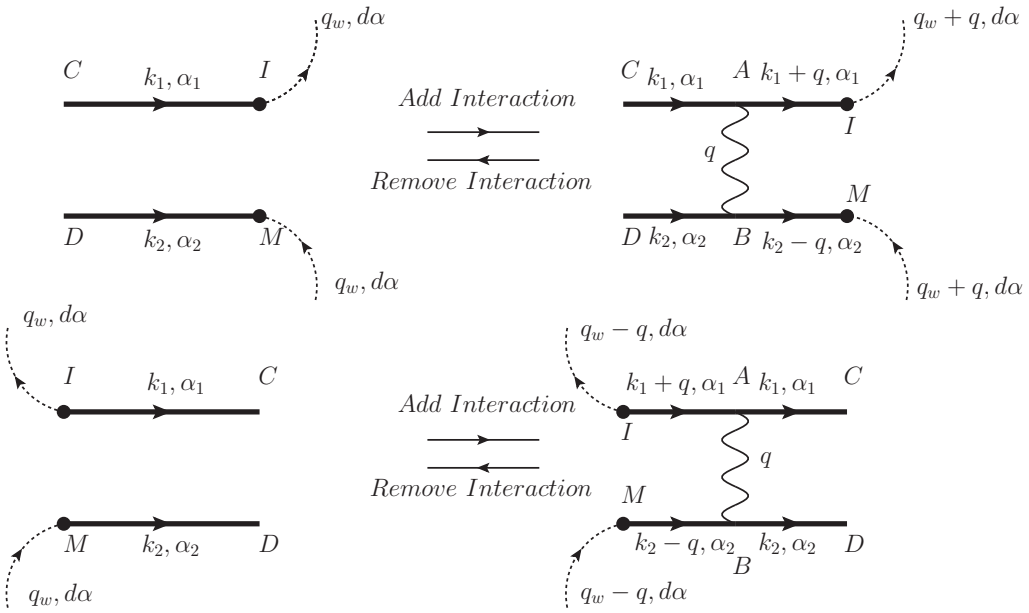

Figure 2.16. Two cases in the *Add-Interaction–Remove-Interaction* updates that insert/remove a new wavy interaction line and change the diagram order by ± 1.

Algorithm 6 Add-Interaction

procedure AddInteraction
  if no worm **then return**
  Choose the direction $\rightarrow$ or $\leftarrow$ for both I and M
Propose to:
  add a **wavy** interaction line $A \Leftrightarrow B$ between propagator lines $I-C$ and $M-D$
  generate time variables with probability density function $P_t(t)$ for A and B
  update the momentum of propagators $I - A$ and $M - B$
  set the spin of propagators $I - A$ and $A - C$ as $\mathrm{Sp}(I - C)$
  set the spin of propagators $M - B$ and $B - D$ as $\mathrm{Sp}(M - D)$

  if is-reducbible() **then return**
acceptance probability:

$$\begin{aligned}
\mathcal{P}^a_{ai} &= min\Big(1, \Big|\frac{D(new)}{D(old)}\Big| \cdot \frac{1}{P_t(t_A))P_t(t_B)dt^2} \cdot \frac{P^c_{ri}}{P^c_{ai}}\Big) \\
&= min\Big(1, \Big|(-1) \cdot \frac{G(I-A)G(A-C)G(M-B)G(B-D)\Delta W(A \Leftrightarrow B)}{G(I-C)G(M-D)}\Big| \\
&\quad \cdot \frac{1}{P_t(t_A)P_t(t_B)} \cdot \frac{P^c_{ri}}{P^c_{ai}}\Big)
\end{aligned} \tag{2.41}$$

13: **if** $rand() \leq \mathcal{P}^a_{ai}$ **then**
14: update the topology
15: update the variables(momenta, times, spins)
16: keep track of the phase factor

Algorithm 7 Remove-Interaction

1: **procedure** RemoveInteraction
2: **if** no worm **then return**
3: Choose the direction $\rightarrow$ or $\leftarrow$ for both I and M
4: find the correponding vertexes A, C, B, D
5: **if** W(A) != W(B) **then return**
6: **if** W(A) is bare-interaction(dash line) **then return**
7: **if** Sp$(I - A)$!= Sp$(A - C)$ **then return**
8: **if** Sp$(M - B)$!= Sp$(B - D)$ **then return**
9: *Propose to*:
10: remove vertexes A and B, and W-line $A \Leftrightarrow B$
11: update the momentum q_w
12:
13: **if** is-reducbible() **then return**
14: *acceptance probability*:

$$\begin{aligned}
\mathcal{P}^a_{ri} &= min\Big(1, \Big|\frac{D(new)}{D(old)}\Big| \cdot P_t(t_A)P_t(t_B)dt^2 \cdot \frac{P^c_{ai}}{P^c_{ri}}\Big) \\
&= min\Big(1, \Big|(-1) \cdot \frac{G(I-C)G(M-D)}{G(I-A)G(A-C)G(M-B)G(B-D)\Delta W(A \Leftrightarrow B)}\Big| \\
&\quad \cdot P_t(t_A)P_t(t_B) \cdot \frac{P^c_{ai}}{P^c_{ri}}\Big) \qquad (2.42)
\end{aligned}$$

15: **if** $rand() \leq \mathcal{P}^a_{ri}$ **then**
16: update the topology
17: update the variables(momenta, times, spins)
18: keep track of the phase factor

Update-R

Update-R is a self-complenmentary update. It proposes to change the space variables along a fermionic loop formed by propagator lines.

Algorithm 8 Update-R

1: **procedure** UPDATER
2: **if** worm exists **then return**
3: Randomly choose a vertex, say i.
4: Search for all the vertexes in the same fermi loop with i and all the interaction lines connected to these vertexes.
5: *Propose to*:
6: update the site variable on the loop $\mathbf{r} \to \mathbf{r}'$ with $P_r(\mathbf{r}')d\mathbf{r}'$.
7: update the weights of interaction lines in the loop, $W \to W'$.
8: *acceptance probability*:

$$\begin{aligned} \mathcal{P}^a_{ur} &= min\Big(1, \Big|\frac{D(new)}{D(old)}\Big| \cdot \frac{P_r(\mathbf{r})}{P_r(\mathbf{r}')}\Big) \\ &= min\Big(1, \Big|\frac{W' \cdots W'}{W \cdots W}\Big| \cdot \frac{P_r(\mathbf{r})}{P_r(\mathbf{r}')}\Big) \end{aligned} \tag{2.43}$$

9: **if** $rand() \leq \mathcal{P}^a_{ur}$ **then**
10: update the site variable
11: update the weights of the interaction lines
12: keep track of the phase factor

Update-Tau

Update-Tau is a self-complenmentary update which proposes to change the imaginary time variable of a vertex.

Algorithm 9 Update-Tau

1: **procedure** UPDATETAU
2: Randomly choose a vertex, say i.
3: *Propose to*:
4: update the imaginary time variable on the vertex $\tau \to \tau'$ with $P_t(\tau')d\tau'$.
5: update the weights of the interaction line and propagator lines connected to the vertex, $G_{\text{in}} \to G'_{\text{in}}$, $G_{\text{out}} \to G'_{\text{out}}$, and $W \to W'$

6: *acceptance probability*:

$$\begin{aligned} \mathcal{P}^a_{ur} &= min\Big(1, \Big|\frac{D(new)}{D(old)}\Big| \cdot \frac{P_t(\tau)}{P_t(\tau')}\Big) \\ &= min\Big(1, \Big|\frac{G'_{\rm in}G'_{\rm out}W'}{G_{\rm in}G_{\rm out}W}\Big| \cdot \frac{P_t(\tau)}{P_t(\tau')}\Big) \end{aligned} \tag{2.44}$$

7: **if** $rand() \leq \mathcal{P}^a_{ur}$ **then**
8: update the imaginary time variable
9: update the weights of the propagators and interaction
10: keep track of the phase factor

Swap-Measure

Swap-Measure is a self-complenmentary update. It proposes to swap the measuring line between a propagator line and an interaction line. There's a constraint that we can not assign a measuring line to a bare interaction line which is a delta function of imaginary time.

Algorithm 10 Swap-Measure

1: **procedure** SWAPMEASURE
2: **if** worm exists **then return**
3: **if** measuring line is G line **then**
4: Randomly choose an interaction line (n choices)
5: **if** W-line is a dash line **then return**
6: **else**
7: Randomly choose a G-line from $2n$ propagator lines
8: *Propose to*:
9: set the new selected line as the measuring line
10: set the old measuring line back to normal
11: *acceptance probability*:
12: **if** old measuring line is G, new measuring line is W **then**

$$\begin{aligned} \mathcal{P}^a_{sm} &= min\Big(1, \Big|\frac{D(new)}{D(old)}\Big| \cdot \frac{n}{2n}\Big) \\ &= min\Big(1, \Big|\frac{G}{W}\Big| \cdot \frac{1}{2}\Big) \end{aligned} \tag{2.45}$$

13: **else**

$$\begin{aligned} \mathcal{P}^a_{sm} &= min\Big(1, \Big|\frac{D(new)}{D(old)}\Big| \cdot \frac{2n}{n}\Big) \\ &= min\Big(1, \Big|\frac{W}{G}\Big| \cdot 2\Big) \end{aligned} \tag{2.46}$$

14: **if** $rand() \leq \mathcal{P}^a_{sm}$ **then**
15: update the measuring index
16: keep track of the phase factor

Change-W-Function

Change-W-Function is a self-complenmentary update which proposes to change an interaction line from a ΔW-line to a dashed J-line or vise versa.

Algorithm 11 Change-W-Function

1: **procedure** ChangeWFunction
2: **if** worm exists **then return**
3: Randomly choose a W-line from n interaction lines
4: **if** W is a measuring line **then return**
5: *Propose to*:
6: **if** W is bare interaction J **then**
7: change W to a wavy line ΔW
8: generate a new imaginary time variable to the right end of W
9: **else** W is ΔW
10: change W to a dashed J-line
11: change the imaginary time at the right end of W as τ of the left end
12: *acceptance probability*:
13: **if** current W line is bare interaction J **then**

$$\begin{aligned} \mathcal{P}^a_{cwf} &= min\Big(1, \Big|\frac{D(new)}{D(old)}\Big| \cdot \frac{1}{P_t(\tau_2)d\tau_2}\Big) \\ &= min\Big(1, \Big|\frac{\Delta W(\tau_2 - \tau_1)}{J}\Big| \cdot \frac{1}{P_t(\tau_2)}\Big) \end{aligned} \tag{2.47}$$

14: **else**

$$\begin{aligned} \mathcal{P}^{a}_{cwf} &= min\Big(1, \Big|\frac{D(new)}{D(old)}\Big| \cdot P_t(\tau_2)d\tau_2\Big) \\ &= min\Big(1, \Big|\frac{J}{\Delta W(\tau_2-\tau_1)}\Big| \cdot P_t(\tau_2)\Big) \end{aligned} \tag{2.48}$$

15: **if** $rand() \leq \mathcal{P}^{a}_{cwf}$ **then**
16: update the weight
17: update the imaginary time variable
18: keep track of the phase factor

Jump-To-Norm – Jump-To-Order1

Jump-To-Norm and *Jump-To-Order1* are a pair of complementary updates that swap configurations between an order-0 normalization diagram and an order-1 diagram.

When proposing to jump from an order-1 diagram to a normalization configuration, the proposal probability is simply

$$\mathcal{P}^{p}_{jn} = \mathcal{P}^{c}_{jn} \tag{2.49}$$

However, if one proposes to jump from the normalization configuration to an order-1 diagram, there'll be a set of new variables generated, including the space variable on the Fermi loop, the time variables on the 2 vertexes, the spin indices for the two propagators. The proposal probability is

$$\mathcal{P}^{p}_{jo1} = \mathcal{P}^{c}_{jo1}(\frac{1}{2})^2 P_r(\mathbf{r})P_t(\tau_1)P_t(\tau_2)d\mathbf{r}dt^2 \tag{2.50}$$

Once the new variables have been generated, the weight of the new order-1 diagram can also be calculated. Note that the prefactor for order-1 diagram is $(-1)^1$ since $n = 1$ and there's 0 Fermi loop in the self-energy or polarization diagram.

Algorithm 12 Jump-To-Norm

procedure JUMPTONORM
  if worm exists **then return**
  if Interaction is bare interaction J **then return**
Propose to:
  update the configuration to the normalization diagram.
acceptance probability:

$$\begin{aligned}\mathcal{P}^a_{jn} &= min\Big(1, \Big|\frac{D(new)}{D(old)}\Big| \cdot \frac{1}{4} P_r(\mathbf{r}) P_t(\tau_1) P_t(\tau_2) d\mathbf{r} dt^2 \cdot \frac{\mathcal{P}^c_{jo1}}{\mathcal{P}^c_{jn}}\Big) \\ &= min\Big(1, \Big|\frac{D(norm)}{D(order1)}\Big| \frac{1}{4} P_r(\mathbf{r}) P_t(\tau_1) P_t(\tau_2) \cdot \frac{\mathcal{P}^c_{jo1}}{\mathcal{P}^c_{jn}}\Big) \end{aligned} \tag{2.51}$$

  if $rand() \leq \mathcal{P}^a_{jn}$ **then**
    update the configuration to the normalization diagram
    keep track of the phase factor

Algorithm 13 Jump-To-Order1

procedure JUMPTOORDER1
  if worm exists **then return**
  Randomly pick α_1, α_2 from ± 1
  Randomly generate space variable $\mathbf{r}$ from $P_r(\mathbf{r})$
  Randomly generate imaginary time τ_1 and τ_2 from $P_t(\tau_1)$ and $P_t(\tau_2)$
  Randomly set the momentum for the propagators, calculate the momentum for the interaction line
Propose to:
  update the configuration to the order-1 diagram.
acceptance probability:

$$\begin{aligned}\mathcal{P}^a_{jo1} &= min\Big(1, \Big|\frac{D(new)}{D(old)}\Big| \cdot 4 \cdot \frac{1}{P_r(\mathbf{r}) P_t(\tau_1) P_t(\tau_2) d\mathbf{r} dt^2} \cdot \frac{\mathcal{P}^c_{jn}}{\mathcal{P}^c_{jo1}}\Big) \\ &= min\Big(1, \Big|\frac{D(order1)}{D(norm)}\Big| \cdot 4 \cdot \frac{1}{P_r(\mathbf{r}) P_t(\tau_1) P_t(\tau_2)} \cdot \frac{\mathcal{P}^c_{jn}}{\mathcal{P}^c_{jo1}}\Big) \end{aligned} \tag{2.52}$$

  if $rand() \leq \mathcal{P}^a_{jo1}$ **then**
    update the configuration to a order-1 diagram
    set the spin of the two propagators as α_1 and α_2
    set the space variables of both vertexes as $\mathbf{r}$
    set the imaginary time variables of both vertexes as τ_1 and τ_2
    set the interaction function as ΔW
    set the momenta for propagators and interaction
    keep track of the phase factor

2.5 $G^2W\Gamma_3$-skeleton Expansion

In this section, we introduce another boldification scheme as an extension of the G^2W-skeleton expansion, which we will refer to as the $G^2W\Gamma_3$-skeleton scheme. This formulation is based on Hedin's equations [39] and involves the calculation of the three-point vertex function Γ using Diagrammatic Monte Carlo techniques.

Hedins equations [39] are a complete set of self-consistent equations for self-energy(Σ), polarization(Π), propagator(G), effective potential(W), and vertex function(Γ). For finite temperature systems, Hedin's equations have the following form:

$$
\begin{aligned}
G &= G^{(0)} + G^{(0)}\Sigma G \quad (Dyson's\ equation) && (2.53)\\
\Gamma &= 1 + \frac{\delta\Sigma}{\delta G} GG\Gamma && (2.54)\\
\Pi &= GG\Gamma && (2.55)\\
W &= J + J\Pi W \quad (Screening\ equation) && (2.56)\\
\Sigma &= -GW\Gamma && (2.57)
\end{aligned}
$$

where equations 2.53, 2.55, 2.57, and 2.56 are all closed-form expressions, while equation 2.54 consists of an infinite series of diagrams.

The vertex function in the space–imaginary-time representation (Fig. 2.17) has two space variables and two imaginary time variables.

$$
\Gamma_{\alpha_1\alpha_2\alpha_3\alpha_4}(\mathbf{r}, \mathbf{r}', \tau, \tau') = \Gamma_{\alpha_1\alpha_2\alpha_3\alpha_4}(\mathbf{r}_1 - \mathbf{r}_3, \mathbf{r}_2 - \mathbf{r}_3, \tau_1 - \tau_3, \tau_2 - \tau_3) \tag{2.58}
$$

It can be proved that in spin systems, because the propagators are always local in space, the vertex function $\Gamma(\mathbf{r}, \mathbf{r}') = \Gamma(\mathbf{r})\delta(\mathbf{r} - \mathbf{r}')$ only has one space variable. The diagrammatic representation for the three-point vertex function Γ is a triangle object as in Fig. 2.17.

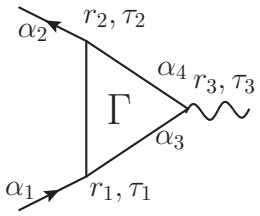

Figure 2.17. Variables of the three-point vertex function Γ. In the Heisenberg model, the spin indices satisfy the conservation law $\alpha_1 + \alpha_4 = \alpha_3 + \alpha_2$, and the space variables satisfy $r_1 = r_2$.

The Feynman diagram representation of Hedin's equations is shown in Fig. 2.18.

The diagrammatic expansion for the three-point vertex function Γ is shown in Fig. 2.19.

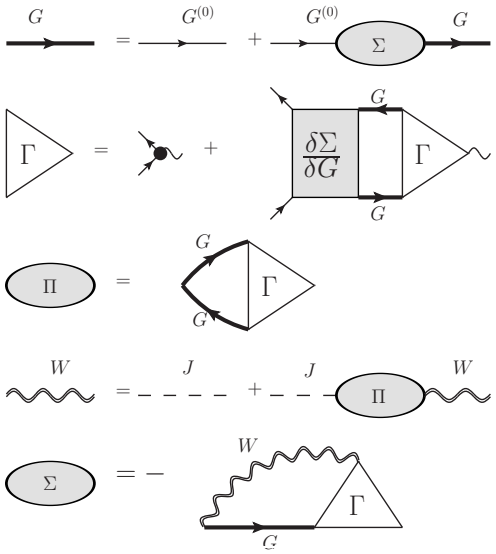

Figure 2.18. The Feynman diagram representation of Hedin's equations. Here we use thick directed lines to denote the full propagator G, thin directed line to denote the bare propagator $G^{(0)}$, dashed line to denote the bare interaction J, and double wavy line to denote the screened interaction W. The three-point vertex Γ has two terms, a delta function term (denoted as a black dot), and a continuous part.

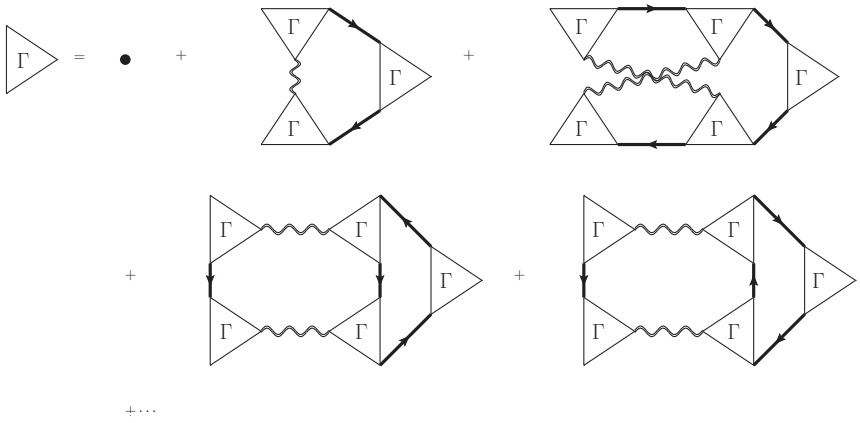

Figure 2.19. The Feynman diagram expansion of the three-point vertex Γ. The diagrams for Γ satisfy the following irreducibility condition: by cutting any two propagators and one interaction line that are not connected to the same Γ one will not separate the diagram into disconnected pieces.

The three-point vertex diagrams are irreducible in the following sense: when cutting two propagator lines and one interaction line which are not connected to the same Γ, the graph always remains connected. This irreducible rule can also be implemented by introducing an auxiliary momentum to each propagator and interaction line with conservation law at each Γ object (Fig.2.20). Similar to the G^2W scheme, we store those momenta in two separate Hash tables for propagators and interactions. The irreduciblity rule for Γ can be formulated as: for any two propagators with momenta k_1 and k_2, there can not be an interaction line with momentum $q = |k_1 - k_2|$ except when all the three lines are connected to the same Γ.

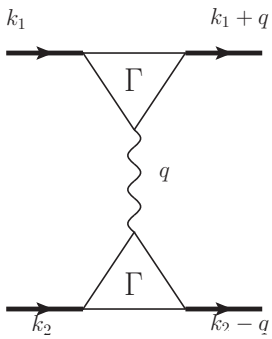

Figure 2.20. The auxiliary momentum on each propagator line and interaction line. The momentum conservation law is satisfied at each Γ triangle.

There is another interesting property of the Γ diagrams which is the conservation law for spin variables. For a Heisenberg Hamiltonian, we have already shown that in the G^2W-skeleton scheme, the total spin is conserved at each interaction line. It can be proved that, in the Feynman diagram expansion for the three-point vertex Γ, the spins are also conserved at each interaction line as shown in Fig. 2.21.

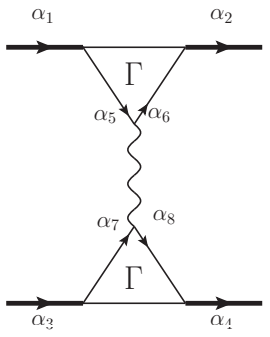

Figure 2.21. The spins at each interaction line satisfy the conservation law $\alpha_5+\alpha_7 = \alpha_6+\alpha_8$. The four spin indices for Γ also satisfy the conservation law, for example, $\alpha_1+\alpha_6 = \alpha_5+\alpha_2$, and $\alpha_3+\alpha_8 = \alpha_7+\alpha_4$. Thus the spins on the four propagators have relation $\alpha_1+\alpha_3 = \alpha_2+\alpha_4$.

Similarly to the G^2W-skeleton scheme, we can apply Monte Carlo sampling to calculate the diagrams of the three-point vertex Γ up to a fixed maximum diagram order n, and plug the obtained Γ into the other Hedin's equations to calculate the self-

energy Σ, polarization Π, full propagator G and screened interaction W, which can be passed to the Monte Carlo procedure and recalculate Γ again until convergence.

In the diagrammtic Monte Carlo sampling, the diagram configurations have the following structure. As shown in Fig. 2.22, each configuration of order-n contains $2(n+1)$ propagator lines, $n+1$ interaction lines, $2(n+1)$ Γ triangles, and $6(n+1)$ vertexes. Each propagator line in the diagram carries a spin index α, and each vertex carries a space and imaginary time variable $(\mathbf{r}, \tau)$. At each vertexes that connects to an interaction line, there're two spin indices which define the spin type for the interaction line. There are two types of interaction lines in the diagram, the delta function J (dashed line), or the continuous part $\Delta W = W - J$ (single wavy line). For each diagram, there's one Γ triangle that is a dummy measuring object (denoted as a black dot) with unity weight, and all the three lines connected to it are also measuring lines with unity weight.

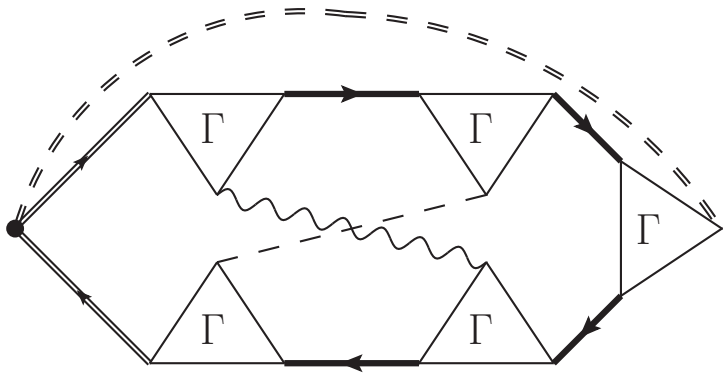

Figure 2.22. An example of an order-2 diagram for the three-point vertex Γ. The double lines and black dot are the measuring part with the weight 1. The weight of the diagram is calculated as the product of weights of all diagrammatic elements present in the Feynman diagram: lines and triangles.

In order to enforce the irreducibility and spin conservation law in the diagrams, the Monte Carlo sampling for the Γ diagrams also employs the worm algorithm. Thus the configuration space for the three-point vertex Γ consists of physical and unphysical diagrams.

In an unphysical diagram, there exist two special Γ triangles (Fig. 2.23), namely I and M, which break the conservation law of spin and momentum.

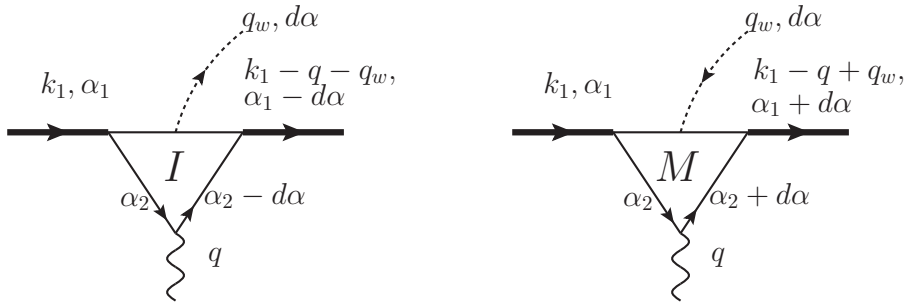

Figure 2.23. Two examples of the special triangles I and M which break the conservation law for momentum and spin. It can be interpreted as there is an imaginary line from I to M with a flow of momentum q_w and spin projection $d\alpha$. Note that the conservation law is violated only at the interaction lines connected to I or M, but the conservation law for the four spins of each triangle is always satisfied even for I and M.

With these special triangles, one can construct a complete set of local updates that can move the special triangles around, update the momentum and spin indexes along the way, and at the same time update the topology and diagram order. When the two special triangles fall on top of each other, the configuration returns to a physical configuration with conservation law satisfied on all the triangles. Only the physical configurations will contribute to the measurement of the three-point vertex Γ.

The design of updates for the three-point vertex diagrams follows the same principle as in the G^2W-skeleton scheme, therefore we will not list the detailed pseudo-codes here.

Compared to the G^2W-skeleton scheme, the self-consistent $G^2W\Gamma_3$-skeleton scheme for the three-point vertex further reduces the number of diagrams and allows the Monte Carlo method to account for diagrams of higher orders (the number of diagrams for different renormalization schemes is shown in Table 2.1). However, there's no guarantee that the $G^2W\Gamma_3$-skeleton diagram series will have better convergence

than the G^2W expansion. Another disadvantage of the $G^2W\Gamma_3$ expansion is that the general Γ function has two space variables and two imaginary time variables, which will cause a memory problem in the simulations. But in the spin systems where the propagators are always local, the number of space variables in Γ is reduced to 1, which makes the three-point vertex approach more tractable.

n	1	2	3	4	5	6	7	8	9
bare	1	9	100	1323	20088	342430	6461208	133618275	3006094768
G^2W	1	6	49	542	7278	113824	2017881	39842934	865391422
$G^2W\Gamma_3$	1	3	13	147	1965	30979	559357	11289219	250794109

Table 2.1. The number of n^{th}-order skeleton diagrams in the bare expansion, G^2W-skeleton scheme and the $G^2W\Gamma_3$-skeleton scheme [1].

2.6 Benchmark Results

In this section, we show the results of the bold diagrammatic Monte Carlo simulations with G^2W-skeleton expansion and $G^2W\Gamma_3$-skeleton expansion for the nearest-neighbor antiferromagnetic quantum Heisenberg model on 3-dimensional cubic lattice. The results are compared with the unbiased path-integral Monte Carlo calculations [38].

The quantum Heisenberg model with nearest-neighbor antiferromagnetic (AF) interactions on cubic lattice (Eq. 2.1) features a finite-temperature phase transition at $T_c = 0.946(1)$ [40]. Above the critical temperature, the system is a paramagnet, while when temperature drops below the critical temperature T_c, the system becomes an antiferromagnet with long-range Néel order. Since the three-dimensional simple cubic lattice is bipartite, the path-integral representation of the AF quantum Heisenberg model doesn't have any sign problem and thus can be efficiently simulated by path-

integral Monte Carlo method [38]. Therefore we can use it to benchmark the bold diagrammatic Monte Carlo methods we introduced in this chapter.

We use the staggered susceptibility as the observable to perform the comparison.

$$\chi_{stag} = \langle \mathbf{M}_{stag}^2 \rangle = \langle (\sum_i (-1)^{x_i+y_i+z_i} \mathbf{S_i})^2 \rangle \tag{2.59}$$

At $\beta J = J/T = 0.5$, the two diagram series both have good convergence toward the unbiased result. After lowering the temperature to $\beta J = 0.7$, the $G^2W\Gamma_3$ series fails to converge up to 6th-order, while the G^2W expansion retains good convergence. When we further lower the temperature to $\beta J = 0.85$, the G^2W-expansion doesn't achieve convergence up to 7th-order (nevertheless, the 7-th order answer is within 10% of the correct value). Note that this temperature is still above the critical temperature $T/J = 0.946(1)$ a.k.a. $\beta J = 1.057(1)$. Slow convergence is, of course, expected on approach to the phase transition point because at T_c the thermodynamic functions are not analytic.

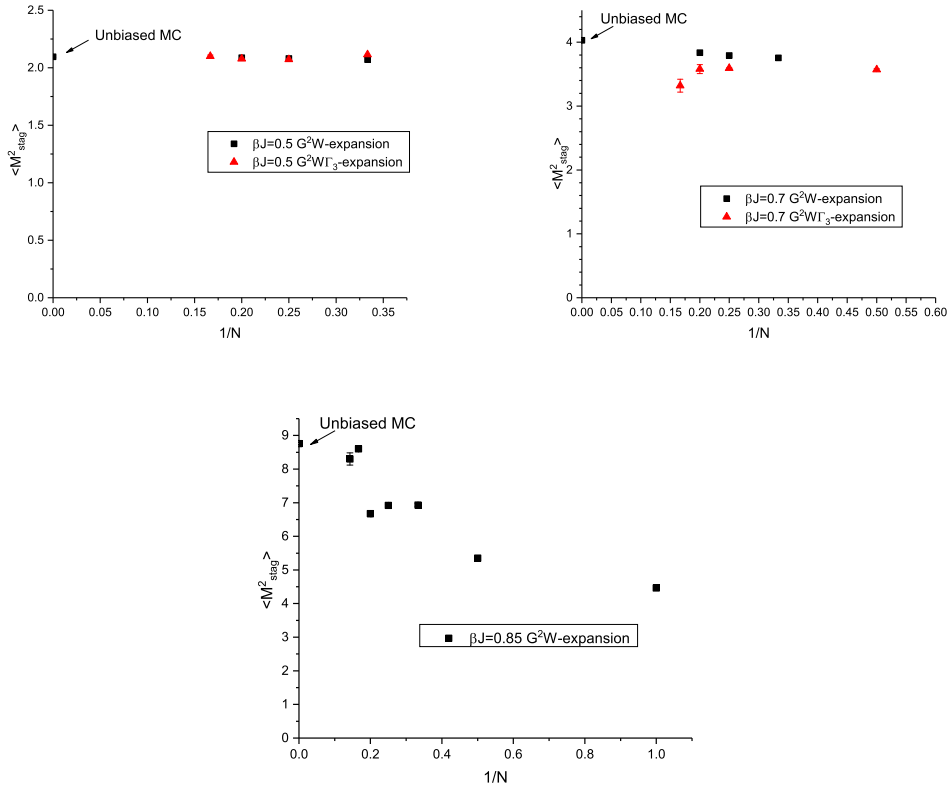

Figure 2.24. Staggered magnetization as a function of the inverse series order $1/N$ calculated from the G^2W and $G^2W\Gamma_3$ expansions using the diagrammatic Monte Carlo method, along with the unbiased path-integral Monte Carlo results plotted at $1/N = 0$.

CHAPTER 3

CONSERVING BOLD DIAGRAMMATIC MONTE CARLO

In the previous chapter, we introduced the BDMC approach to self-consistently calculate the Green's function, screened interaction, self-energy and polarization in a quantum spin system, and construct the spin-spin correlation function (Eq. 2.23) using the polarization $\Pi^{(n)}$. However, this construction fails to satisfy several important conservation laws and sum rules, which is known as the vertex problem. This problem has the consequence that one is unable, from these correlation functions, to describe correctly even the qualitative features of the low-energy transport processes of the system. In this chapter, we will introduce another approximation method based on the Baym and Kadanoff theorem [41] that yields spin-spin correlation function which guarantees the conservation law of the total spin (or particle number in a different context). We will also explain in detail how to implement this conserving approximation on top of the existing G^2W-skeleton BDMC framework.

3.1 Conserving Approximations

In order to study a transport property, one applies an external field to a system initially in thermodynamic equilibrium, $H \to H - \sum_{\mathbf{r},\tau} U(\mathbf{r},\tau) n(\mathbf{r},\tau)$. The response to the applied field can be calculated from the changes in the expectation values of the density of the quantity (total particle number), which can be expressed in terms of the one-particle Green's function $G(1,1',U)$ defined in the presence of the external

potential U. In order to obtain $G(U)$, we first write down the partition function in the presence of U,

$$Z[U] = Z_0 \left\langle \int \mathcal{D}[\psi^\dagger, \psi]\; e^{-\int_0^\beta d\tau H_I(\tau)}\; e^{\int d1d1' \psi^\dagger(1') U(1',1) \psi(1)} \right\rangle_0 \tag{3.1}$$

$$Z_0 = \int \mathcal{D}[\psi^\dagger, \psi]\; e^{\int d1d1' \psi^\dagger(1') G^{(0)-1}(1',1) \psi(1)} \tag{3.2}$$

and deduce the one-particle Green's function $G(1, 1', U)$ from the functional derivative

$$G(1, 1', U) = \langle \mathcal{T} \psi(1) \psi^\dagger(1') \rangle = \frac{\delta \ln Z[U]}{\delta U(1', 1)} \tag{3.3}$$

The G^2W-skeleton formulation in the presence of U is shown in Fig. 3.1. The functions W, Σ, and Π don't explicitly depend on U (we deliberately exclude the U term from the definition of Σ and mention it separately in the Dyson equation).

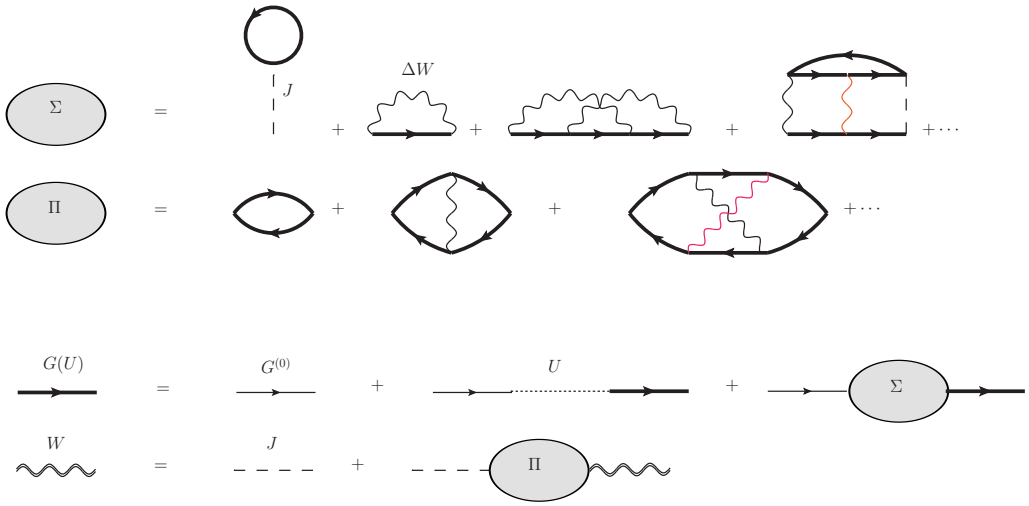

Figure 3.1. The G^2W-skeleton formulation in the presence of the external potential term U (the dotted line in the equation for $G(U)$). The operators W, Σ, and Π don't explicitly depend on U.

According to the Dyson equation relating bare and fully dressed Green's functions, we can show that the one-particle Green's function $G(U)$ satisfies the following

relations:

$$\begin{aligned}
\delta(1,1') &= \int d2(G(1,2)G^{-1}(2,1')) \\
&= \int d2(G(1,2)G^{(0)-1}(2,1') - G(1,2)U(2,1') - G(1,2)\Sigma(2,1')) \\
&= (-\frac{\partial}{\partial\tau_{1'}} - \frac{\nabla_{1'}^2}{2m})G(1,1') - \int d2(G(1,2)U(2,1') + G(1,2)\Sigma(2,1')) \quad (3.4) \\
\delta(1,1') &= \int d2G^{-1}(1,2)G(2,1') \\
&= \int d2(G^{(0)-1}(1,2)G(2,1') - U(1,2)G(2,1') - \Sigma(1,2)G(2,1')) \\
&= (\frac{\partial}{\partial\tau_1} - \frac{\nabla_1^2}{2m})G(1,1') - \int d2(U(1,2)G(2,1') + \Sigma(1,2)G(2,1')) \quad (3.5)
\end{aligned}$$

Now subtract Eq. 3.4 from Eq. 3.5 to see that $G(U)$ satisfies:

$$\begin{aligned}
(\frac{\partial}{\partial\tau_{1'}} + \frac{\partial}{\partial\tau_1} - \frac{\nabla_1^2 - \nabla_{1'}^2}{2m})G(1,1') = &\int d2(U(1,2)G(2,1') - G(1,2)U(2,1')) \\
&+ \int d2(\Sigma(1,2)G(2,1') - G(1,2)\Sigma(2,1')) \quad (3.6)
\end{aligned}$$

When we set $1' = 1^+$ in Eq. 3.6, we will find that

$$\begin{aligned}
\frac{\partial}{\partial\tau_1}G(1,1^+) - i\nabla_1 \cdot (\frac{\nabla_1 - \nabla_{1'}}{2mi}G(1,1')|_{1'=1^+}) &= -i\ (i\frac{\partial}{\partial\tau_1}\langle\hat{n}(1)\rangle + \nabla_1 \cdot \langle\hat{\mathbf{j}}(1)\rangle) \\
&= \int d2(U(1,2)G(2,1^+) - G(1,2)U(2,1^+)) \quad (3.7)
\end{aligned}$$

The second term on the right hand side of Eq. 3.6 vanishes because in the G^2W-skeleton formulation, we have $\int d2\Sigma(1,2)G(2,1^+) = \int d2G(1,2)\Sigma(2,1^+)$ order by order. Eq. 3.7 is an exact statement of the particle number conservation law in the presence of an external field which adds and removes particles from the system. If $U(2,2') = \delta(2,2')U(2)$, i.e., if the external field can be represented in the Hamiltonian by a coupling to the density, then Eq. 3.7 becomes

$$i\frac{\partial}{\partial\tau_1}\langle\hat{n}(1)\rangle + \nabla_1 \cdot \langle\hat{\mathbf{j}}(1)\rangle = 0 \quad (3.8)$$

The right hand side vanishes since such a external field term can not add or remove particles from the system. We see then, that in our G^2W-skeleton expansion, the approximate G(U) exactly satisfies the particle number conservation law, Eq. 3.7.

Once we have a fully conserving $G(U)$, we can find the linear response to the external potential. This linear response is defined by

$$\frac{\delta G(1,1',U)}{\delta U(2)} = \frac{\delta^2 \ln Z[U]}{\delta U(1',1)\delta U(2^+,2)} \equiv \Gamma_G(1,1',2) \tag{3.9}$$

which we denote as the three-point vertex $\Gamma_G(1,1',2)$, see Fig. 3.2.

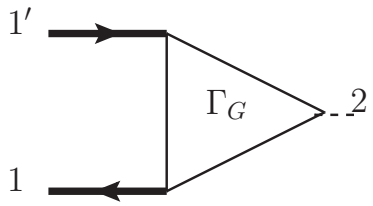

Figure 3.2. The three-point vertex $\Gamma_G(1,1',2)$. The short line on the right of the triangle denotes that this point can be connected to an interaction line.

When we set $1' = 1^+$ in the three-point vertex $\Gamma_G(1,1',2)$, we obtain the two-body correlation function $\chi(1,2)$ (shown in Fig. 3.3),

$$\begin{aligned} \Gamma_G(1,1^+,2) &= \frac{\delta G(1,1^+)}{\delta U(2^+,2)} = \frac{\delta \langle \hat{n}(1) \rangle}{\delta U(2^+,2)} \\ &= \langle \hat{n}(1)\hat{n}(2) \rangle - \langle \hat{n}(1) \rangle \langle \hat{n}(2) \rangle = \chi(1,2) \end{aligned} \tag{3.10}$$

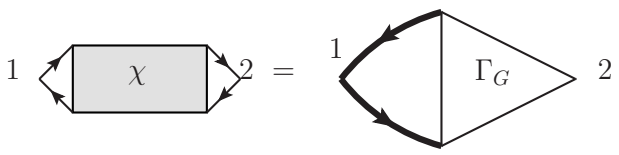

Figure 3.3. The two-body correlation function $\chi(1,2)$ is defined as $\Gamma_G(1,1^+,2)$.

The conservation laws for $G(U)$ imply conservation laws for Γ_G. If we take derivative of the conservation law (Eq. 3.7), we will find

$$[(\frac{\partial}{\partial\tau_1} - i\nabla_1 \cdot \frac{\nabla_1 - \nabla_{1'}}{2mi})\frac{\delta G(1,1')}{\delta U(2',2)}]|_{1'=1^+,2'=2^+} = G(2,2')[\delta(1,2') - \delta(1,2)]|_{2'=2^+} \quad (3.11)$$

Applying $\frac{\nabla_2 - \nabla_{2'}}{2mi}$ on both sides, we will get

$$\frac{\partial}{\partial\tau_1}\langle\mathcal{T}\hat{n}(1)\ \hat{\mathbf{j}}(2)\rangle - i\nabla_1 \cdot \langle\mathcal{T}\hat{\mathbf{j}}(1)\ \hat{\mathbf{j}}(2)\rangle = \frac{\nabla_2}{mi}\delta(1,2)\langle\hat{n}(2)\rangle \quad (3.12)$$

Eq. 3.12 indicates that the exact Γ_G not only satisfies the density conservation law in the form

$$\langle\mathcal{T}[(\frac{\partial}{\partial\tau_1} - i\nabla_i \cdot \hat{\mathbf{j}}(1))\ \hat{\mathbf{j}}(2)]\rangle = 0 \quad (3.13)$$

but that it also correctly relates the expectation value of the equal-time density-current commutator to the density gradient

$$\langle[n(\mathbf{r}_1), \mathbf{j}(\mathbf{r}_2)]\rangle = i\frac{\nabla_1}{m}\delta(\mathbf{r}_1, \mathbf{r}_2)\langle\hat{n}\rangle \quad (3.14)$$

3.2 Self Consistent Construction for Γ_G

In the previous section, we have shown that we can use the three-point vertex Γ_G to obtain the two-body correlation function χ. In this section, we will describe how to construct the diagrammatic formulation for the three-point vertex Γ_G from the approximate G, W, Σ and Π from the G^2W-skeleton expansion that respects the above conservation laws and exact relations, unlike the previous scheme shown in Fig. 2.19.

As defined in Eq. 3.9, the three-point vertex Γ_G can be derived from the dressed Green's function G using the following relation

$$\Gamma_G(1,1',2) = \frac{\delta G(1,1')}{\delta U(2)} \quad (3.15)$$

From the relation $GG^{-1} = 1$, we notice that

$$\Gamma_G(1,1',2) = \frac{\delta G(1,1')}{\delta U(2)} = -\int d3d3'\ G(1,3)\frac{\delta G^{-1}(3,3')}{\delta U(2)}G(3',1') \tag{3.16}$$

Combined with the relation $G^{-1} = G^{(0)-1} - U - \Sigma$, we obtain the self-consistent relation for Γ_G:

$$\begin{aligned}
\frac{\delta G^{-1}(3,3')}{\delta U(2)} &= -\delta(3,2^+)\delta(3',2) - \int d4d4'(\frac{\partial\Sigma(3,3')}{\partial G(4,4')}\frac{\delta G(4,4')}{\delta U(2)} + \frac{\partial\Sigma(3,3')}{\partial W(4,4')}\frac{\delta W(4,4')}{\delta U(2)}) \\
\Gamma_G(1,1',2) &= G(1,2)G(2,1') + \int d3d3'd4d4'G(1,3)\frac{\partial\Sigma(3,3')}{\partial G(4,4')}\frac{\delta G(4,4')}{\delta U(2)}G(3',1') \\
&\quad + \int d3d3'd4d4'G(1,3)\frac{\partial\Sigma(3,3')}{\partial W(4,4')}\frac{\delta W(4,4')}{\delta U(2)}G(3',1')
\end{aligned} \tag{3.17}$$

Fig. 3.4 gives a diagrammatic illustration of the self-consistent equation for Γ_G, where $\frac{\partial\Sigma}{\partial G}$ and $\frac{\partial\Sigma}{\partial W}$ correpond to removing one propagator or interaction line in the self-energy diagram expansions defined in Fig. 3.1. The three-point vertex Γ_W in the last term represents $\frac{\delta W}{\delta U}$ which will be expalined later.

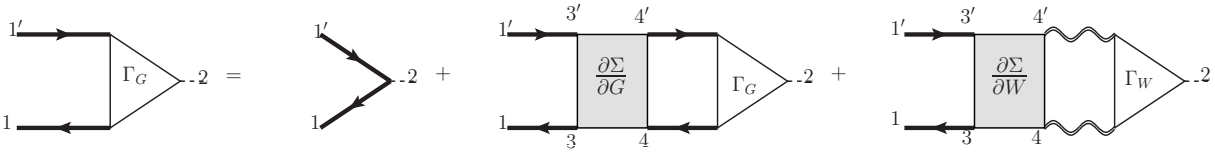

Figure 3.4. The self consistent construction for Γ_G. The objects $\frac{\partial\Sigma}{\partial G}$ and $\frac{\partial\Sigma}{\partial W}$ correpond to removing one propagator or interaction line in the self-energy diagram expansions. The object Γ_W can also be given by a self-consistent equation shown later (Eq. 3.18).

Note that although the Hatree term doesn't contribute to Σ after summing up the spin indices, this term can not be neglected in $\frac{\partial\Sigma}{\partial G}$. Therefore, we use $\frac{\partial\tilde{\Sigma}}{\partial G}$ to denote the irreducible part which can not be cut into two parts when removing one interaction line, and take care of the Hatree term separately in our calculation.

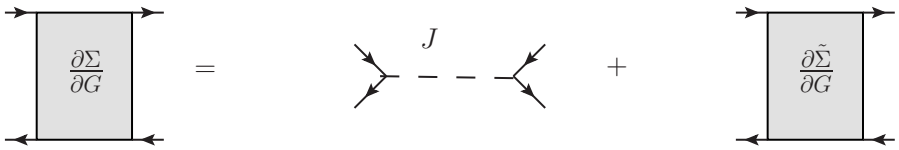

Figure 3.5. The operator $\frac{\partial\Sigma}{\partial G}$ can be divided into two parts: one is the Hatree term which is simply a bare interaction line, the other one is the irreducible $\frac{\partial\tilde{\Sigma}}{\partial G}$ which can not be cut into two parts when removing one interaction line. In our calculation, the second term will be directly sampled in the Monte Carlo simulation, and the first term will be dealt with analytically.

The three-point vertex Γ_W is given by a similar self-consistent equation:

$$\begin{aligned}
\Gamma_W(1,1',2) &= \frac{\delta W(1,1')}{\delta U(2)} = -\int d3d3'\ W(1,3)\frac{\delta W^{-1}(3,3')}{\delta U(2)}W(3',1') \\
&= \int d3d3'd4d4'W(1,3)\frac{\partial\Pi(3,3')}{\partial G(4,4')}\frac{\delta G(4,4')}{\delta U(2)}W(3',1') \\
&+ \int d3d3'd4d4'W(1,3)\frac{\partial\Pi(3,3')}{\partial W(4,4')}\frac{\delta W(4,4')}{\delta U(2)}W(3',1') \qquad (3.18)
\end{aligned}$$

The diagrammatic representation of Γ_W is shown in Fig. 3.6. Combined with Fig. 3.4, this gives the self-consistent construction of the three-point vertexes Γ_G and Γ_W, based on which the correlation function with conserving properties can be obtained.

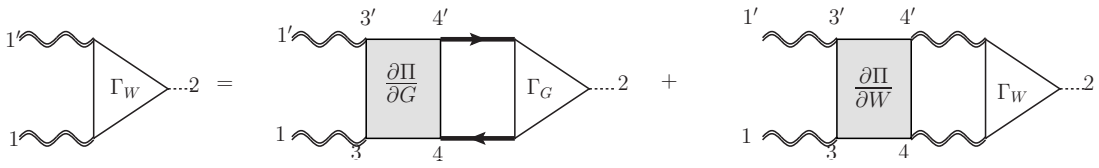

Figure 3.6. The self consistent construction for Γ_W. The objects $\frac{\partial\Pi}{\partial G}$ and $\frac{\partial\Pi}{\partial W}$ correpond to removing one propagator or interaction line in the polarization diagram expansions. The object Γ_G is given by the self-consistent Eq. 3.17.

3.3 Monte Carlo Sampling

In this section, we will show that the calculation of the three-point vertexes can be naturally integrated to the BDMC scheme with a few additional Monte Carlo updates.

3.3.1 Configuration Setup

In Section 2.4, we have introduced a Monte Carlo update scheme that stochastically samples the self-energy and polarization diagrams. The configuration space includes the normalization diagram, physical diagrams(self-energy sector, polarization sector) and unphysical diagrams (with worm). In order to measure the three-point vertexes, we need to add two more measuring sectors in the configuration space (Γ_G and Γ_W sector).

The Γ_G and Γ_W sectors measure the diagram expansions shown in Fig. 3.7 and Fig. 3.8 respectively. For convenience, the measured diagrams are not based on the integrals in Eq. 3.17 and Eq. 3.18, but rather on the parts $\int d4d4' \frac{\partial \tilde{\Sigma}(3,3')}{\partial G(4,4')} \Gamma_G(4,4',2) + \frac{\partial \Sigma(3,3')}{\partial W(4,4')} \Gamma_W(4,4',2)$ and $\int d4d4' \frac{\partial \Pi(3,3')}{\partial G(4,4')} \Gamma_G(4,4',2) + \frac{\partial \Pi(3,3')}{\partial W(4,4')} \Gamma_W(4,4',2)$, i.e. the final three-point vertex is recovered after the convolution of the measured Monte Carlo objects, Γ_G^{MC} and Γ_W^{MC} with propagator and interaction lines, respectively:

After obtaining the measurements of Γ_G^{MC} and Γ_W^{MC}, we can calculate the actual Γ_G and Γ_W functions as

$$\begin{aligned} \Gamma_G(1,1',2) &= G(1,2)G(2,1') + \int d3d4\ G(1,3)G(3,1')J(3,4)\Gamma_G(4,4,2) \\ &\quad + \int d3d3'\ G(1,3)\Gamma_G^{MC}(3,3',2)G(3',1') \qquad (3.19) \\ \Gamma_W(1,1',2) &= \int d3d3'\ W(1,3)\Gamma_W^{MC}(3,3',2)W(3',1') \qquad (3.20) \end{aligned}$$

To reduce computational cost, one can also Fourier transform the functions into $(\mathbf{k}, i\omega_n)$ representation to perform fast convolutions.

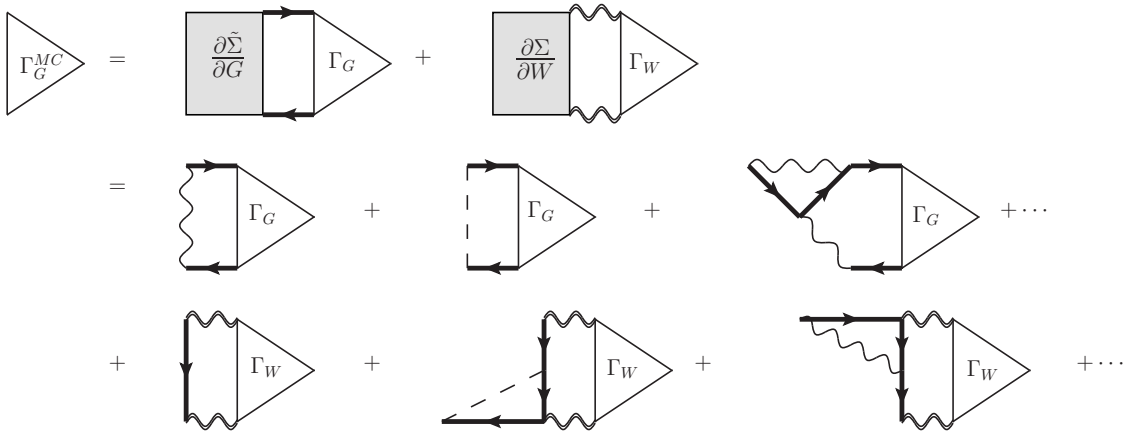

Figure 3.7. The diagram expansions of Γ_G^{MC} measured in Monte Carlo. We can see that the diagrams of Γ_G^{MC} can be obtained by replacing a propagator line with a Γ_G or an interaction line with a Γ_W in a self-energy diagram.

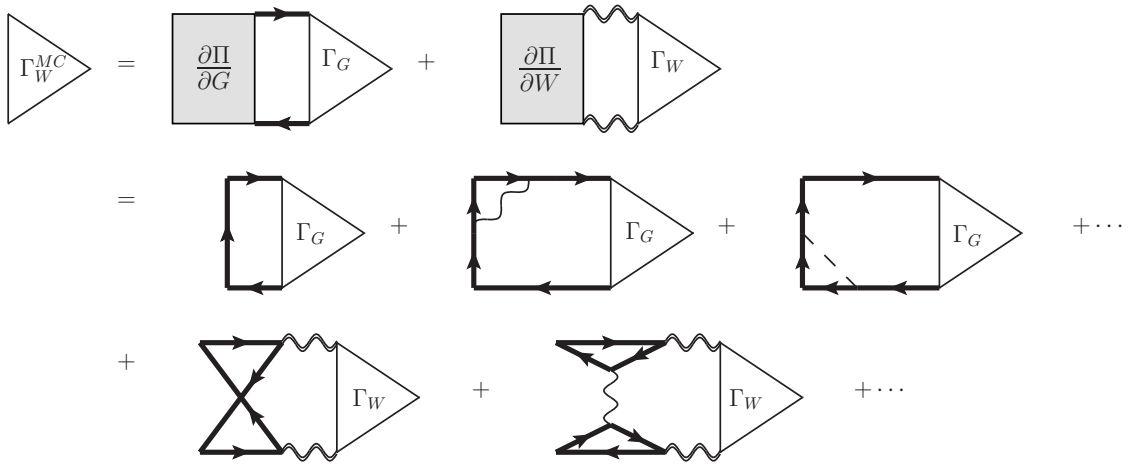

Figure 3.8. The diagram expansions of Γ_W^{MC} measured in Monte Carlo. We can see that the diagrams of Γ_W^{MC} can be obtained by replacing a propagator line with a Γ_G or an interaction line with a Γ_W in a polarization diagram.

3.3.2 Updating Scheme

The scheme discussed in this subsection is implemented on top of the scheme discussed in subsection 2.4.2, where we described a set of updates that are ergodic to explore the enlarged configuration space of both the physical diagrams of self energy and polarization and unphysical diagrams.

The new configuration space has the same structure as in subsection 2.4.2, but with an additional label on each line. Each of the $2n$ propagator lines and n interaction lines has a label to indicate whether this line is a normal propagator (or interaction) line, or a Γ_G (or Γ_W) line. Since there's an external point in the Γ_G and Γ_W structure, the space, time, and spin indices of this external vertex will also be part of the configuration. In the diagram, there can be only one Γ_G line or one Γ_W line (Γ_G and Γ_W can not exist at the same time), or none. If in a physical diagram there's a Γ_G or Γ_W line, the diagram measures either a Γ_G^{MC} or a Γ_W^{MC} depending on the measuring line. If there's no special Γ line, the diagram measures a self-energy or polarization depending on the measuring line.

In subsection 2.4.2, all the updates are still able to be applied to the new enlarged configuration space as long as we take care of the weight of each line corresponding to its label. The set of updates in subsection 2.4.2 allows us to explore all the physical and unphysical configurations with a fixed set of Γ labels for all the lines and a fixed set of external variables. In order to make the updates ergodic, we need to introduce some additional updates to update the Γ labels and external variables.

G-to-GammaG – GammaG-to-G

The pair of complementary updates *G-to-GammaG – GammaG-to-G* change a random propagator line between a normal G and a Γ_G designations, as shown in Fig. 3.9.

When changing a propagator from a normal G to Γ_G, we need to randomly choose a propagator line and randomly choose the variables $(\mathbf{r}_{ext}, \tau_{ext}, \{\alpha_{ext}\})$ for the external

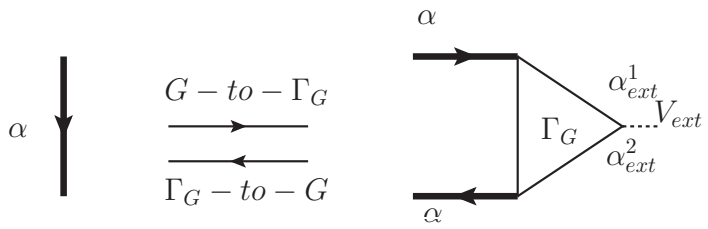

Figure 3.9. The *G-to-GammaG/GammaG-to-G* updates that change a random propagator line between a normal G and a Γ_G.

vertex V_{ext}. Therefore, the proposal probability for *G-to-GammaG* is

$$\mathcal{P}^{p}_{g2ga} = \mathcal{P}^{c}_{g2ga} \frac{1}{2n} P_r(\mathbf{r}_{ext}) P_\tau(\tau_{ext}) \cdot \frac{1}{4} \tag{3.21}$$

The proposal probability for *GammaG-to-G* is

$$\mathcal{P}^{p}_{ga2g} = \mathcal{P}^{c}_{ga2g} \tag{3.22}$$

The pseudo-codes for *G-to-GammaG* and *GammaG-to-G* are listed as follows.

Algorithm 14 G-to-GammaG

```
1: procedure GtoGammaG
2:     if worm exists then return
3:     if there exists a Γ_G or Γ_W in the diagram then return
4:     Choose a random Gline G(A → B)
5:     if G(A → B) is measuring line then return
6:     Randomly choose α^1_ext = ±1 and α^2_ext = ±1
7:     Generate r_ext from distribution P_r(r)
8:     Generate τ_ext from distribution P_τ(τ_ext)
9:  Propose to:
10:    change the label for G(A → B) to Γ_G
11:    set the variables for external vertex V_ext as (r_ext, τ_ext, α^1_ext, α^2_ext)
12:    update the weight of G(A → B) as Γ_G
```

13: *acceptance probability*:

$$\begin{aligned}\mathcal{P}^a_{g2ga} &= min\Big(1, \frac{|D(new)|\cdot\mathcal{P}^p_{ga2g}}{|D(old)|\cdot\mathcal{P}^p_{g2ga}}\Big)\\ &= min\Big(1, \Big|\frac{D(new)}{D(old)}\Big|\cdot\frac{8n}{P_r(\mathbf{r}_{ext})P_t(\tau_{ext})}\cdot\frac{\mathcal{P}^c_{ga2g}}{\mathcal{P}^c_{g2ga}}\Big)\\ &= min\Big(1, \Big|\frac{\Gamma_G(A\to B, V_{ext})}{G(A\to B)}\Big|\cdot\frac{8n}{P_r(\mathbf{r}_{ext})P_t(\tau_{ext})}\cdot\frac{\mathcal{P}^c_{ga2g}}{\mathcal{P}^c_{g2ga}}\Big)\end{aligned} \tag{3.23}$$

14: **if** $rand() \le \mathcal{P}^a_{g2ga}$ **then**
15: change the label for $G(A\to B)$ to Γ_G
16: save the index of this propagator line
17: set the variables for external vertex V_{ext}
18: update the weight
19: keep track of the phase factor based on $D(new)/D(old)$

Algorithm 15 GammaG-to-G

1: **procedure** GammaG-to-G
2: **if** worm exists **then return**
3: **if** there is no $Gamma_G$ in the diagram **then return**
4: get the index for the $\Gamma_G(A\to B, V_{ext})$ propagator
5: *Propose to*:
6: change the propagator to a normal G line
7: update the weight
8: *acceptance probability*:

$$\begin{aligned}\mathcal{P}^a_{ga2g} &= min\Big(1, \Big|\frac{D(new)}{D(old)}\Big|\cdot\frac{P_r(\mathbf{r}_{ext})P_t(\tau_{ext})}{8n}\cdot\frac{\mathcal{P}^c_{g2ga}}{\mathcal{P}^c_{ga2g}}\Big)\\ &= min\Big(1, \Big|\frac{G(A\to B)}{\Gamma_G(A\to B, V_{ext}}\Big|\cdot\frac{P_r(\mathbf{r}_{ext})P_t(\tau_{ext})}{8n}\cdot\frac{\mathcal{P}^c_{g2ga}}{\mathcal{P}^c_{ga2g}}\Big)\end{aligned} \tag{3.24}$$

9: **if** $rand() \le \mathcal{P}^a_{ga2g}$ **then**
10: delete the external vertex V_{ext}
11: change the label of $G(A\to B)$ back to normal
12: update the weight of $G(A\to B)$
13: keep track of the phase factor based on $D(new)/D(old)$

W-to-GammaW – GammaW-to-W

Similarly, the pair of complementary updates *W-to-GammaW – GammaW-to-W* change a random wavy interaction line between a normal ΔW and a Γ_W , as shown in Fig. 3.10.

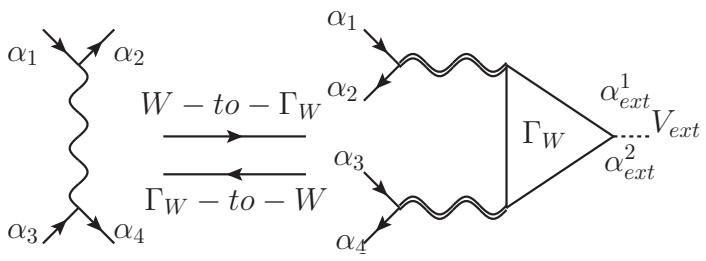

Figure 3.10. The *W-to-GammaW/GammaW-to-W* updates that change a random interaction line between a normal ΔW and a Γ_W.

When changing an interaction from a normal ΔW to Γ_W, we need to randomly choose an interaction line and randomly choose the variables $(\mathbf{r}_{ext}, \tau_{ext}, \{\alpha_{ext}\})$ for the external vertex V_{ext}. Therefore, the proposal probability for *W-to-GammaW* is

$$\mathcal{P}^p_{w2ga} = \mathcal{P}^c_{w2ga} \frac{1}{n} P_r(\mathbf{r}_{ext}) P_\tau(\tau_{ext}) \cdot \frac{1}{4} \tag{3.25}$$

The proposal probability for *GammaW-to-W* is

$$\mathcal{P}^p_{ga2w} = \mathcal{P}^c_{ga2w} \tag{3.26}$$

The pseudo-code for *W-to-GammaW* and *GammaW-to-W* are listed as follows.

Algorithm 16 W-to-GammaW

procedure WtoGammaW
  if worm exists **then return**
  if there exists a Γ_W or Γ_G in the diagram **then return**
  Choose a random Wline $W(A \Leftrightarrow B)$
  if $W(A \Leftrightarrow B)$ is measuring line **then return**
  if $W(A \Leftrightarrow B)$ is a delta interaction J **then return**
  Randomly choose $\alpha^1_{ext} = \pm 1$ and $\alpha^2_{ext} = \pm 1$
  Generate $\mathbf{r}_{ext}$ from distribution $P_r(\mathbf{r})$
  Generate τ_{ext} from distribution $P_\tau(\tau_{ext})$
Propose to:
  change the label for $W(A \Leftrightarrow B)$ to Γ_W
  set the variables for external vertex V_{ext} as $(\mathbf{r}_{ext}, \tau_{ext}, \alpha^1_{ext}, \alpha^2_{ext})$
  update the weight of $W(A \Leftrightarrow B)$ as Γ_W
acceptance probability:

$$\begin{aligned}
\mathcal{P}^a_{w2ga} &= min\Big(1, \frac{|D(new)| \cdot \mathcal{P}^p_{ga2w}}{|D(old)| \cdot \mathcal{P}^p_{w2ga}}\Big) \\
&= min\Big(1, \Big|\frac{D(new)}{D(old)}\Big| \cdot \frac{4n}{P_r(\mathbf{r}_{ext})P_t(\tau_{ext})} \cdot \frac{\mathcal{P}^c_{ga2w}}{\mathcal{P}^c_{w2ga}}\Big) \\
&= min\Big(1, \Big|\frac{\Gamma_W(A \Leftrightarrow B, V_{ext})}{\Delta W(A \Leftrightarrow B)}\Big| \cdot \frac{4n}{P_r(\mathbf{r}_{ext})P_t(\tau_{ext})} \cdot \frac{\mathcal{P}^c_{ga2w}}{\mathcal{P}^c_{w2ga}}\Big) \qquad (3.27)
\end{aligned}$$

  if $rand() \leq \mathcal{P}^a_{w2ga}$ **then**
    change the label for $W(A \Leftrightarrow B)$ to Γ_W
    save the index of this interaction line
    set the variables for external vertex V_{ext}
    update the weight
    keep track of the phase factor based on $D(new)/D(old)$

Algorithm 17 GammaW-to-W

procedure GammaW-to-W
  if worm exists **then return**
  if there is no $Gamma_W$ in the diagram **then return**
  get the index for the $\Gamma_W(A \Leftrightarrow B, V_{ext})$ interaction
Propose to:
  change the interaction to a normal ΔW wavy interaction line
  update the weight

8: *acceptance probability*:

$$\begin{aligned}\mathcal{P}^a_{ga2w} &= min\Big(1, \Big|\frac{D(new)}{D(old)}\Big| \cdot \frac{P_r(\mathbf{r}_{ext})P_t(\tau_{ext})}{4n} \cdot \frac{\mathcal{P}^c_{w2ga}}{\mathcal{P}^c_{ga2w}}\Big) \\ &= min\Big(1, \Big|\frac{\Delta W(A \Leftrightarrow B)}{\Gamma_W(A \Leftrightarrow B, V_{ext}}\Big| \cdot \frac{P_r(\mathbf{r}_{ext})P_t(\tau_{ext})}{4n} \cdot \frac{\mathcal{P}^c_{w2ga}}{\mathcal{P}^c_{ga2w}}\Big) \end{aligned} \quad (3.28)$$

9: **if** $rand() \leq \mathcal{P}^a_{ga2w}$ **then**
10: delete the external vertex V_{ext}
11: change the label of $W(A \Leftrightarrow B)$ back to normal
12: update the weight of $W(A \Leftrightarrow B)$
13: keep track of the phase factor based on $D(new)/D(old)$

3.4 Irreducible Three-point Vertexes

In the previous sections, we define the self-consistent construction of the three-point vertexes Γ_G and Γ_W as shown in Eqs. 3.19, 3.20, and Figs. 3.7, 3.8. However, this construction will raise a problem when the system approaches a phase transition. The diagrams of Γ^{MC}_G and Γ^{MC}_W measured in Monte Carlo sampling will eventually diverge when approaching the phase transition and lead to unphysical results. In this section, we will introduce a modification in our self-consistent scheme to avoid this instability in the Γ_G and Γ_W function.

In order to overcome this problem, we define the irreducible three-point vertexes $\tilde{\Gamma}_G$ and $\tilde{\Gamma}_W$ as in Fig. 3.11. Since the self-energy $\tilde{\Sigma}$ and polarization Π are irreducible blocks, it's not difficult to prove that the resulted $\tilde{\Gamma}_G$ and $\tilde{\Gamma}_W$ are irreducible, namely they will not be divided into two pieces when cut through one J-line. From the irreducible $\tilde{\Gamma}_G$ and $\tilde{\Gamma}_W$, we can restore the full Γ_G and Γ_W according to Fig. 3.12.

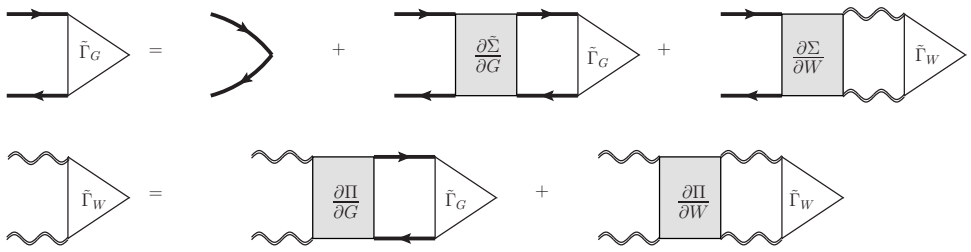

Figure 3.11. The self-consistent definitions for the irreducible three-point vertex $\tilde{\Gamma}_G$ and $\tilde{\Gamma}_W$.

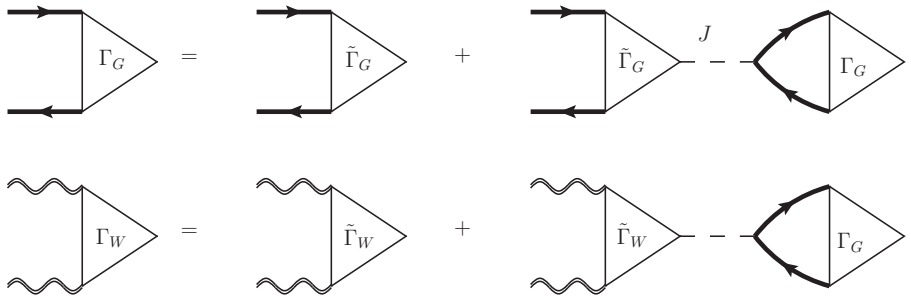

Figure 3.12. The definitions of the full three-point vertexes Γ_G, Γ_W based on the irreducible $\tilde{\Gamma}_G$ and $\tilde{\Gamma}_W$.

The correctness of these relations can be proved as follows. Based on the definitions of $\tilde{\Gamma}_G$ and $\tilde{\Gamma}_W$ given in Fig. 3.11, we can find that the right hand sides in the equations have exactly the same self-consistent definitions with the full three-point vertexes Γ_G and Γ_W.

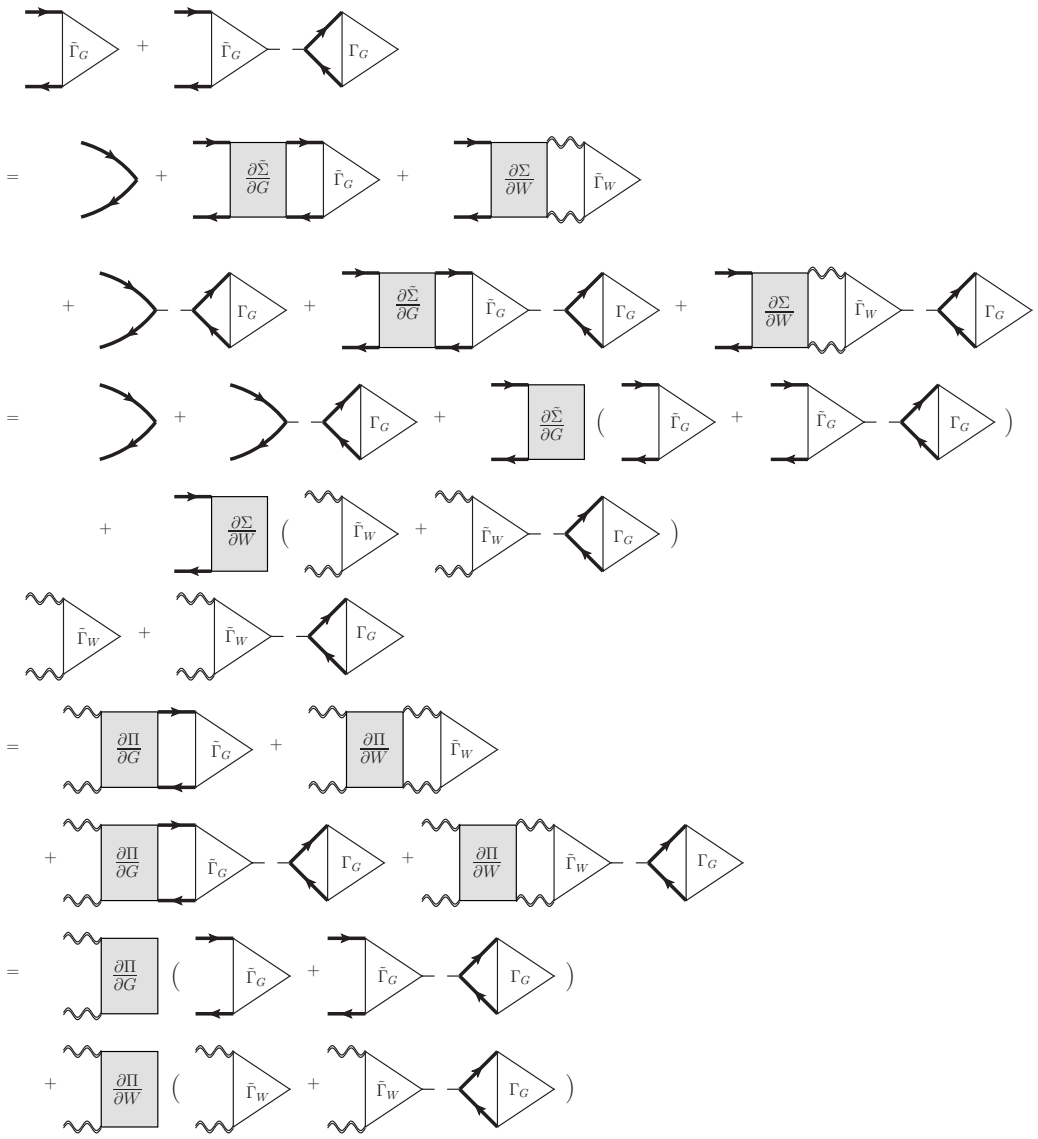

Figure 3.13. Plugging the definitions of $\tilde{\Gamma}_G$ and $\tilde{\Gamma}_W$ (Fig. 3.11) into equations in Fig. 3.12, we can find that the right hand sides are consistent with the definitions of full Γ_G and Γ_W.

With the relations in Fig. 3.12, we only need to measure the irreducible three-point vertexes $\tilde{\Gamma}_G$ and $\tilde{\Gamma}_W$ in the self-consistent scheme and restore the full vertexes

at the end. In the Monte Carlo sampling, we measure diagrams $\tilde{\Gamma}_G^{MC}$ and $\tilde{\Gamma}_W^{MC}$ which have similar structure with Γ_G^{MC} and Γ_W^{MC} defined in Fig. 3.7 and 3.8, but replacing Γ_G, Γ_W with $\tilde{\Gamma}_G$ and $\tilde{\Gamma}_W$ in the diagrams.

Because the singular part of the functions has been taken out, the irreducible part of the three-point vertex $\tilde{\Gamma}_G$ has a very smooth behavior in the whole imaginary time plane. The comparison between the full vertex function Γ_G and irreducible vextex function $\tilde{\Gamma}_G$ is shown in Fig. 3.14 and Fig. 3.15.

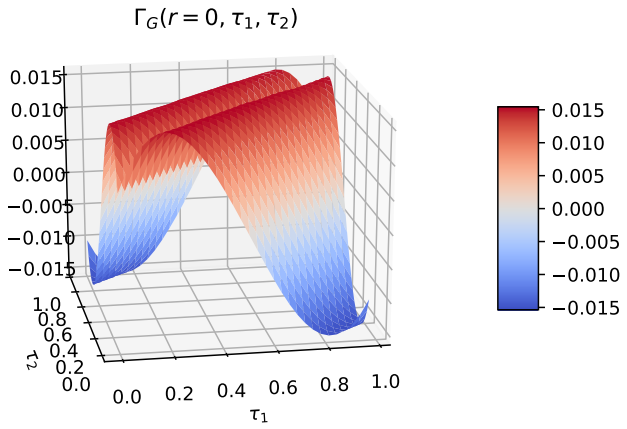

Figure 3.14. The three-point vertex Γ_G as a function of imaginary time τ_1 and τ_2. This result is observed in a square lattice antiferromagnetic Heisenberg model at temperature $T/J = 1$ based on the G^2W-skeleton expansion up to diagram order $N = 4$. There is a cusp in the function along the line $\tau_1 = \tau_2$ which features a discontinuity in the derivative.

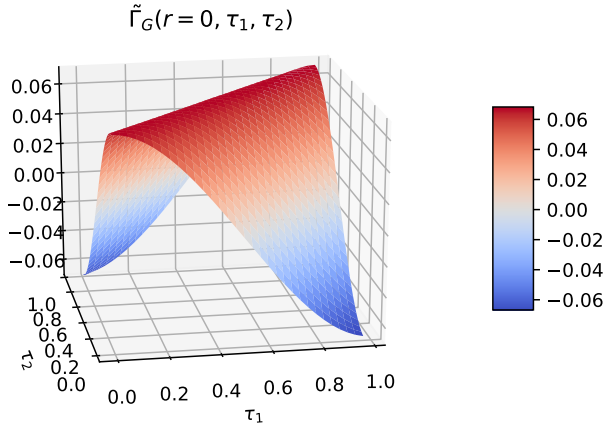

Figure 3.15. The irreducible three-point vertex $\tilde{\Gamma}_G$ in a square lattice antiferromagnetic Heisenberg model at temperature $T/J = 1$ computed up to diagram order $N = 4$. We can see that the irreducible part of Γ_G is a rather smooth function of imaginary time τ_1 and τ_2.

3.5 Benchmarks on Static Observables

In this section, we use the system of antiferromagnetic Heisenberg spins on a two-dimensional square lattice to benchmark the results from the G^2W-skeleton BDMC method and the Baym-Kadanoff Conserving Bold Diagrammatic Monte Carlo approach (CBDMC).

According to the conservation law of the total magnetization, the uniform susceptibility should be independent of imaginary time,

$$\chi(\mathbf{k} = 0, \tau) = \chi(\mathbf{k} = 0, \tau = 0). \tag{3.29}$$

However, as we can see from in the right panel in Fig. 3.16, the susceptibility obtained from the G^2W-skeleton scheme violates this conservation law when we truncate the series to a fixed order. On the other hand, the CBDMC susceptibility constructed from the three-point vertex Γ_G (Fig. 3.3) satisfies the conservation law Eq. 3.29 order by order as shown in the left panel in Fig. 3.16.

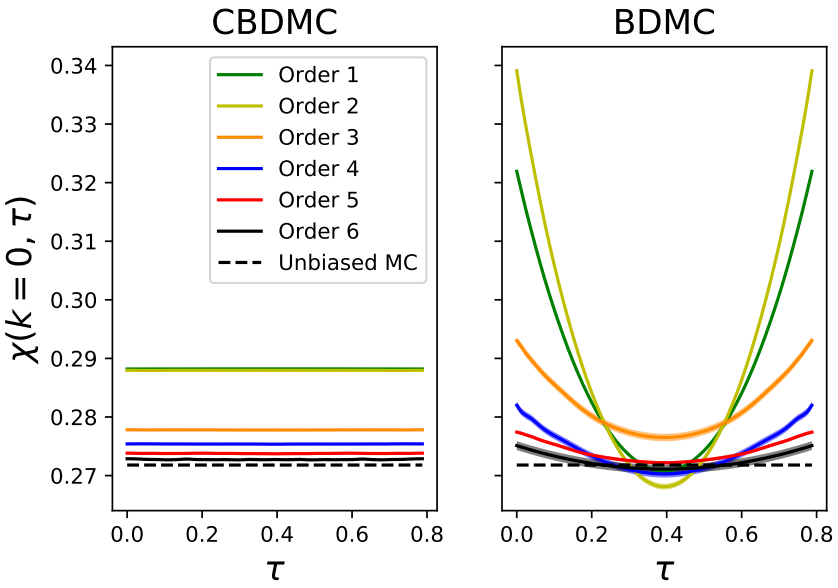

Figure 3.16. The imaginary-time dependence of the uniform susceptibility in the square lattice AF Heisenberg model at temperature $T/J = 0.8$. The left panel is obtained using the CBDMC approach, while the right panel is obtained from the G^2W-skeleton BDMC scheme.

Another important property for the susceptibility is the sum rule in the Fourier space,

$$\beta V \sum_{k,n} \chi(\mathbf{k}, i\omega_n) = \chi(\mathbf{r} = 0, \tau = 0) = \frac{3}{4} \tag{3.30}$$

which is related to the crossing symmetry of the system. However, this property is also violated when we truncate the series at a certain order in the G^2W-skeleton BDMC scheme. Figure 3.17 shows the onsite equal-time susceptibility as a function of diagram order from the BDMC and CBDMC calculations. It turns out, the conserving approximation not only enforces the conservation law in the long wavelength limit ($\mathbf{k} = 0$), but also improves the convergence to the exact result in the ultraviolet limit.

Compared to the BDMC method, the improvement in convergence in CBDMC has been observed in almost all the observables, such as the energy and staggerred magnetization shown in Fig. 3.18 and 3.19 respectively.

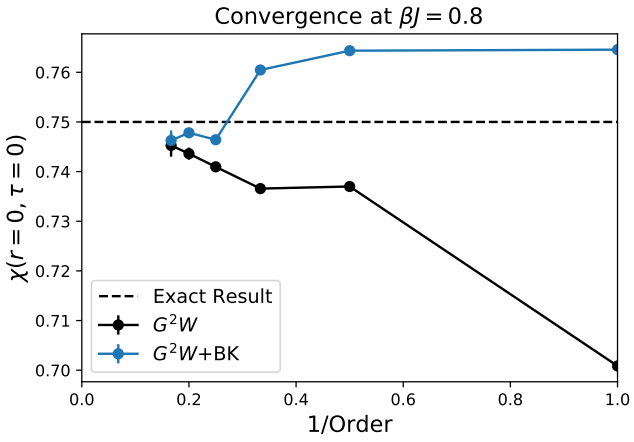

Figure 3.17. The onsite equal-time susceptibility as a function of the inverse diagram order in the square lattice quantum AF Heisenberg model at temperature $T/J = 0.8$. The results are obtained from the G^2W-skeleton BDMC and CBDMC methods respectively.

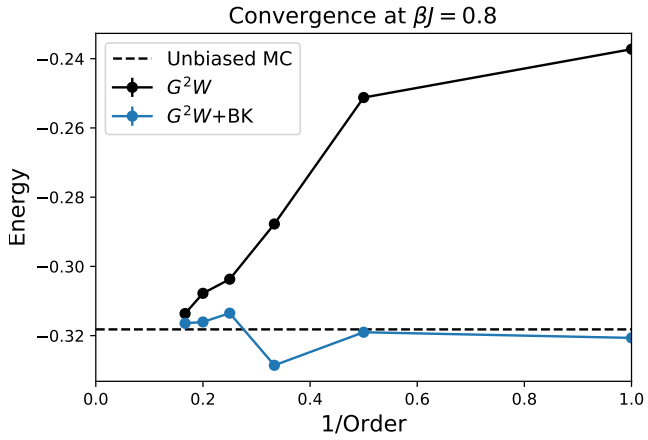

Figure 3.18. The energy as a function of the inverse diagram order in the square lattice quantum AF Heisenberg model at temperature $T/J = 0.8$. The results are obtained from the G^2W-skeleton BDMC and CBDMC methods respectively.

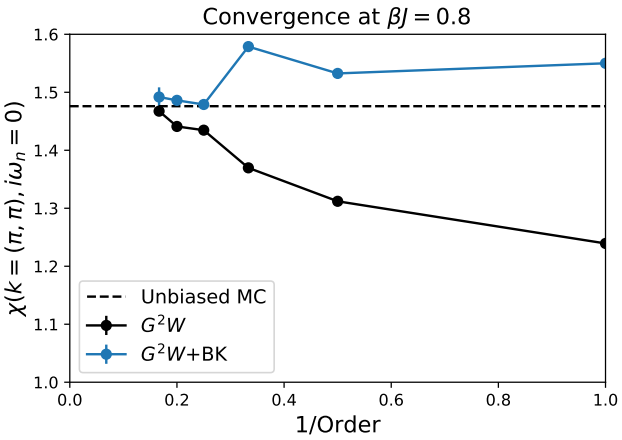

Figure 3.19. The staggered magnetization as a function of the inverse diagram order in the square lattice quantum AF Heisenberg model at temperature $T/J = 0.8$. The results are obtained from the G^2W-skeleton BDMC and CBDMC methods respectively.

In the end, we show the convergence for the static uniform susceptibility for both the G^2W-skeleton BDMC and CBDMC methods. The convergence for the CBDMC series is slightly better than the G^2W-skeleton diagrammatic series at temperature $T/J = 0.8$.

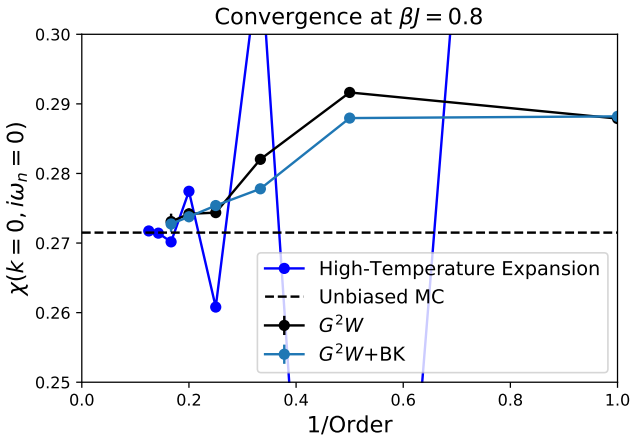

Figure 3.20. The static uniform susceptibility as a function of the inverse diagram order in the square lattice quantum AF Heisenberg model at temperature $T/J = 0.8$. The results are obtained from the G^2W-skeleton BDMC and CBDMC methods respectively.

3.6 Dynamics

Since the Baym Kadanoff conserving approximation fixes the conservation laws in the susceptibility, now we can reliably study the dynamic properties of the system. In this section, we use the triangular lattice AF Heisenberg model as an example and calculate the dynamical structure factor at the Γ point of the brillouin zone, see Fig. 3.21 using both the G^2W-skeleton BDMC and the CBDMC methods.

Since the uniform magnetization is a constant motion in the system, we expect the dynamics of the susceptibility at the Γ point to be a delta function at frequency $\omega = 0$. The dynamics extracted from the G^2W-skeleton BDMC method clearly violates this physics. There is an unphysical "ghost" mode even up to diagram order $N = 4$ as shown in Fig. 3.22. On the other hand, the dynamics calcuated from the CBDMC method fixes this problem and gives the correct peak position starting from the first order. This result shows the importance of the Baym Kadanoff conserving approximation to the study of dynamics.

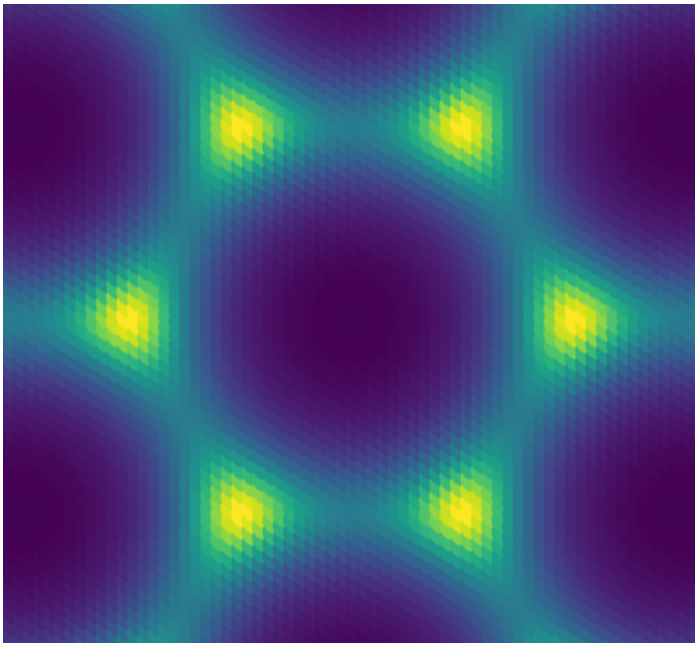

Figure 3.21. The static structure factor of the triangular AF Heisenberg model at temperature $T/J = 0.4$. The Γ point is at the center of the figure.

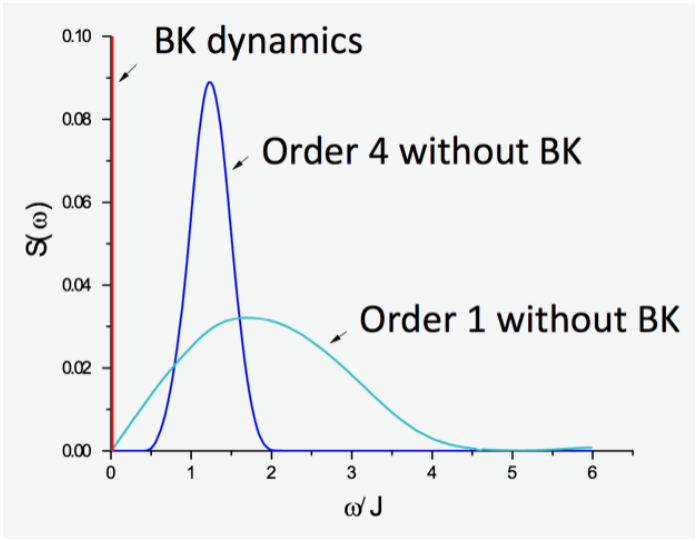

Figure 3.22. The dynamic structure factor at the Γ point of the brillouin zone calculated from the G^2W-skeleton expansion (cyan: order 1 and blue: order 4) and the Baym Kadanoff conserving approximation (red: order 1).

CHAPTER 4

BLESSING OF FRUSTRATION

In this chapter, we will show the convergence of the Bold Diagrammatic Monte Carlo results within the G^2W-skeleton scheme in different quantum spin systems in comparison with high-temperature expansions. We observed that the G^2W-skeleton diagram expansions show the signal of series divergence when the system approaches a low temperature state that can not be smoothly connected to the high temperature state, no matter whether the ground state is ordered or not. However, in frustrated spin systems, where the long range order only develops at very low temperature or even zero-temperature, the G^2W-skeleton series show much better convergence at low temperature.

4.1 Two Spins With Antiferromagnetic Interaction

Let us first consider a very simple system of two quantum S-1/2 spins with antiferromagnetic interaction $J > 0$,

$$H_Q = J\ \hat{\mathbf{S}}_1 \cdot \hat{\mathbf{S}}_2 \tag{4.1}$$

where $\hat{\mathbf{S}} = \frac{1}{2}\hat{\boldsymbol{\sigma}}$. The ground state of the system is a spin singlet $|s\rangle = \frac{1}{\sqrt{2}}(|\uparrow\downarrow\rangle - |\downarrow\uparrow\rangle)$. The spin-spin correlation function $\chi_{ij}(\tau) = \langle \mathcal{T}\mathbf{S}_i(0) \cdot \mathbf{S}_j(\tau)\rangle$ at any finite temperature can be solved exactly with the result

$$\begin{aligned}\langle \mathbf{S}_1(0)\cdot\mathbf{S}_2(\tau)\rangle &= 3\langle \mathcal{T}\ S_1^z e^{H\tau} S_2^z e^{-H\tau}\rangle \\ &= \frac{3}{4}\cdot\frac{(2-e^{J\tau})e^{-\frac{1}{4}J\beta}-e^{-J\tau}e^{\frac{3}{4}\beta J}}{Z} \\ &= \frac{3}{4}\cdot\frac{2-e^{J\tau}-e^{J(\beta-\tau)}}{3+e^{\beta J}}\end{aligned} \tag{4.2}$$

$$\begin{aligned}\langle \mathbf{S}_1(0)\cdot\mathbf{S}_1(\tau)\rangle &= 3\langle \mathcal{T}\ S_1^z e^{H\tau} S_1^z e^{-H\tau}\rangle \\ &= \frac{3}{4}\cdot\frac{2+e^{J\tau}+e^{J(\beta-\tau)}}{3+e^{\beta J}}\end{aligned} \tag{4.3}$$

$$\chi(k=0,i\omega_n=0)=\int_0^\beta \chi_{12}(\tau)+\chi_{11}(\tau)d\tau=\frac{3\beta}{3+e^{\beta J}} \tag{4.4}$$

Taking the inverse temperature βJ as the small parameter, we can obtain the high-temperature expansion as a Taylor expansion in terms of βJ. This result is actually equivalent to the bare series expansion for the spin-spin correlation function as in Fig. 2.5. This expansion nicely converges until temperature as low as $T/J \approx 0.5$.

Figure. 4.1 shows the convergence of the G^2W-skeleton diagram series up to order 5 (black curve) compared to the bare expansion up to order 14 (blue curve). The G^2W-skeleton scheme doesn't seem to improve much in terms of the series convergence compared to the high-temperature expansion series.

4.2 Square Lattice Antiferromagnetic Heisenberg Model

The second system we study is the quantum spin-1/2 square lattice Heisenberg antiferromagnet.

$$H = J\sum_{\langle ij\rangle}\hat{\mathbf{S}}_i\cdot\hat{\mathbf{S}}_j \tag{4.5}$$

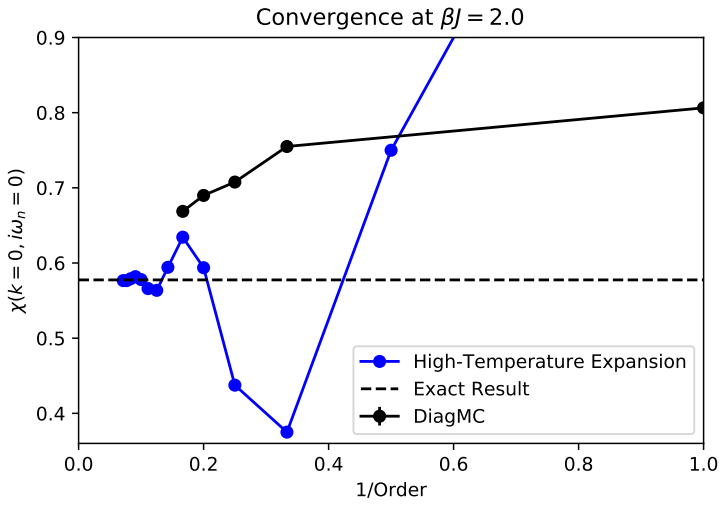

Figure 4.1. The G^2W-skeleton BDMC and high-temperature expansion results of the uniform susceptibility in the two-spin system at temperature $T/J = 0.5$. The susceptibility is ploted as a function of the inverse expansion order.

We use the high-temperature expansion results calculated by H. Schmidt et. al. in Ref. [42] to perform the comparison. The high temperature expansion results from order 4 to 8 for the uniform susceptibility start to exhibit divergence at temperature $T/J \approx 1$.

We carry out the BDMC simulation with the G^2W-skeleton scheme for the square lattice Heisenberg model at temperature $T/J = 1$ and see that the convergence is slightly better than the high-temperature expansion. But since the square lattice is bipartite, the path-integral Monte Carlo for the quantum Heisenberg model doesn't suffer any sign problem and can provide us unbiased results for benchmark. Compared to the unbiased path-integral Monte Carlo result, the systematic error of the DiagMC result stopped at finite order N is still larger than the statistical error, indicating that higher-order calculations are necessary. Still, at order $N = 5$, the BDMC scheme is more accurate than the high-temperature expansion.

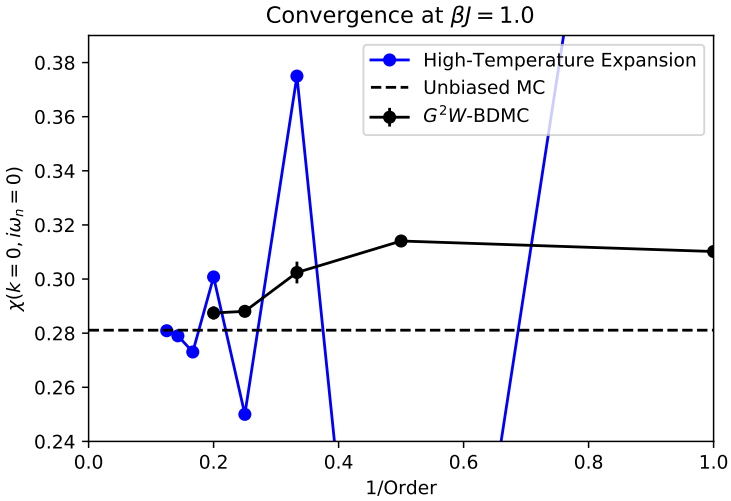

Figure 4.2. The G^2W-skeleton BDMC and high-temperature expansion results of the uniform susceptibility in the square lattice Heisenberg antiferromagnet at temperature $T/J = 1$, along with the unbiased result calculated using path-integral Monte Carlo. The susceptibility is ploted as a function of the inverse expansion order.

4.3 Triangular Lattice Antiferromagnetic Heisenberg Model

From the results for the two-spin system and square lattice, it seems that the G^2W-skeleton series are not significantly better than the high-temperature expansion. It starts to show divergence when approaching the low temperature state. However, in this section, we are going to show that in a frustrated spin system, the performance of the G^2W-skeleton series is much better than the high-temperature expansion results because of the blessing of frustration.

We use the high-temperature expansion results calculated by W. Zheng, et. al. in Ref. [43] to perform the comparison. The high temperature expansion results up to order 10 for the uniform susceptibility start to exhibit divergence at temperature $T/J \approx 1$.

The BDMC simulation with the G^2W-skeleton scheme for the triangular lattice Heisenberg model at temperature $T/J = 1$ shows a significantly better convergence

than the high-temperature expansion. More results for the G^2W-skeleton BDMC results on the triangular lattice AF Heisenberg model can be found in Ref. [16, 17].

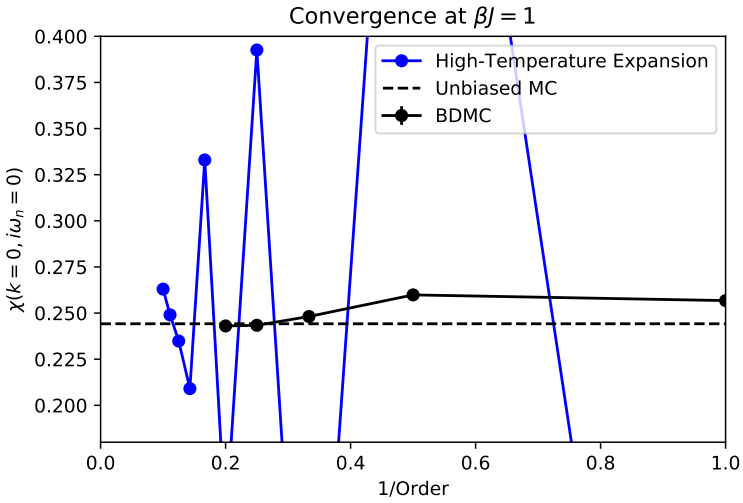

Figure 4.3. The G^2W-skeleton BDMC and high-temperature expansion results for the uniform susceptibility in the triangular lattice Heisenberg antiferromagnet at temperature $T/J = 1$. The susceptibility is ploted as a function of the inverse expansion order.

CHAPTER 5

FRUSTRATED MAGNETISM ON PYROCHLORE LATTICE

The text of this chapter has been adapted from Ref. [44].

5.1 Pyrochlore Lattice Heisenberg Antiferromagnet

A characteristic feature of all frustrated magnets is close competition among numerous classical spin configurations and absence of an obvious arrangement that gains the maximum amount of energy from all interaction terms [45]. Frustration prevents the development of long-range magnetic orders and often leads to novel and exotic collective phenomena. One of the best known examples is the spin-liquid groundstate [46] that does not break any symmetry and supports fractional elementary excitations and emergent gauge fields.

In many quantum antiferromagnets (AFM), frustration has a simple geometric origin when nearest neighbor (n.n.) spins form triangular or tetrahedral units. The canonical three-dimensional example of such a system is the Heisenberg AFM on a pyrochlore lattice that consists of corner-sharing tetrahedrons. The pyrochlore structure is found in numerous magnetic materials and is directly associated with such exotic low-temperature phenomena as spin glass freezing in $Y_2Mo_2O_7$ and $Y_2Mn_2O_7$ [47, 48, 49], classical spin-ice behavior in $Dy_2Ti_2O_7$ and $Ho_2Ti_2O_7$ [50, 51, 52], and cooperative paramagnetism down to ultra-low temperatures in $Tb_2Ti_2O_7$ (and, pre-

sumably, a spin-liquid groundstate) [53, 54, 55] In this chapter, we study the SU(2)-symmetric spin-1/2 Heisenberg AFM on the pyrochlore lattice,

$$H = J \sum_{<ij>} \boldsymbol{S}_i \cdot \boldsymbol{S}_j \qquad (J > 0) \ , \tag{5.1}$$

where $\boldsymbol{S}_i$ is the spin operator on site i, and $\langle \ldots \rangle$ stands for n.n. sites. Despite its simplicity, this model is known to be notoriously difficult to solve at low, but finite, temperature $T < J$ where perturbative treatments are not reliable, conventional Monte Carlo methods suffer from the notorious sign problem (because of frustration), and variational methods are not applicable. As far as we know, diagrammatic Monte Carlo (DiagMC) is the only generic method capable of establishing controlled results in this strongly correlated regime [18, 56, 16, 17], which is also the region most frequently studied experimentally.

5.2 Analytics

Several analytic and numeric studies [57, 58, 59, 60, 61, 21, 20, 62] looked at properties of the related XXZ model $H_{\mathrm{XXZ}} = \sum_{<ij>} J_{zz} S_i^z S_j^z + J_{xy}(S_i^x S_j^x + S_i^y S_j^y)$ that has lower $U(1) \otimes Z_2$ symmetry, admits perturbative treatment when $J_{xy} \ll J_{zz}$, and reduces to the Ising system at $J_{xy} = 0$.

At temperature $T < J_{zz}$, the Ising system features emergent gapped $S_z = 1/2$ spinons that carry fractionalized "electric" charges and interact by Coulomb forces; they remain deconfined because of screening. Charged excitations "freeze out" at low temperature, leaving a massively degenerate ground state manifold. It is known as the spin-ice phase where degenerate states satisfy the "2-in/2-out" ice rule on each tetrahedron [63] and give rise to dipolar correlations. Its characteristic feature is the bow-tie pattern with pinch point singularities in the static structure factor.

Spin-ice states were also predicted to exist in the large-S and large-N limits of spin models [64, 57, 21, 20, 62].

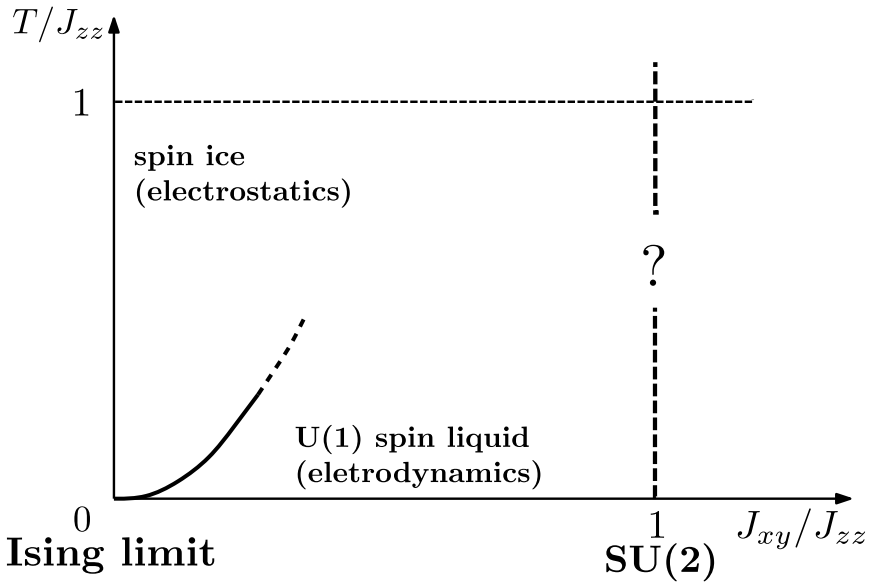

Figure 5.1. Sketch of the finite-temperature phase diagram for the XXZ model based on the perturbation theory. For $J_{xy} \ll J_{zz}$, the first crossover at $T \sim J_{zz}$ (dotted line) is to the thermal spin-ice state; it is followed by a second crossover at $T \sim J_{xy}^3/J_{zz}^2$ to the low-temperature U(1) spin-liquid ground state. Whether the spin-ice state survives on approach to the isotropic Heisenberg point, $J_{xy}/J_{zz} = 1$ is beyond the perturbation theory.

Weak transverse terms, $|J_{xy}| \ll J_{zz}$, can be dealt with by degenerate perturbation theory [61]. At third-order (and low-enough temperature), quantum exchange processes $\propto J_{xy}^3/J_{zz}^2$ operating within the hexagons are argued to lead to the effective "quantum electrodynamics" type system in the continuum limit. In addition to spinons, the system features emergent gapped monopoles carrying fractionalized "magnetic" charges and gapless U(1) gauge bosons, or "photons" [61, 65, 66]. The resulting finite temperature phase diagram is illustrated in Fig. 5.1. The ground state is argued to be a U(1) quantum spin liquid with gapless "photon" excitations. Quantum fluctuations suppress the characteristic pinch-point singularities of the classical

spin-ice, and this fact can be used for experimental identification of the spin-liquid state from the structure factor.

To answer what happens in the non-perturbative case, $J_{xy}/J_{zz} \sim 1$, is a far more difficult task. In this chapter, we employ the DiagMC method to study the isotropic case $J_{xy}/J_{zz} = 1$ in (5.1). We find the spin-ice state dominating system properties over a wide temperature interval, from $T \sim J$ down to the lowest simulated temperature $T = J/6$. At $T = J/6$ the static structure factor features a characteristic bow-tie pattern with pinch points. The ultimate "fingerprint" evidence follows from remarkable quantum-to-classical correspondence (QCC) [17] between the static spin correlation functions of quantum Heisenberg, classical Heisenberg, and classical Ising models on the same lattice at all length scales and all accessible temperatures. Using analytic continuation methods, we compute the dynamic structure factor at real frequencies and observe diffusive spinon dynamics at the pinch points and local spin-fluctuation continuum along the nodal lines. These results are consistent with the effective hydrodynamic theory for the spin ice [20, 67]. A quantum spin-liquid state, if any, may emerge only at temperatures significantly below $J/6$.

5.3 Bold Diagrammatic Monte Carlo Simulations

As introduced in Chapter 2, the bold diagrammatic Monte Carlo method is a controlled numerical approach based on stochastic sampling of all skeleton Feynman diagrams up to some high order N and extrapolation to the $N \to \infty$ limit. This technique allows us to go far beyond the mean-field approximation and account for all skeleton diagrams up to the 6-th order ($> 10^5$ graphs). We apply the BDMC method on the pyrochlore lattice AF Heisenberg model to study its low temperature physics. We simulate finite systems with periodic boundary conditions and always consider system sizes much larger than the spin correlation length to ensure that finite-size corrections remain negligible.

5.4 Results

5.4.1 Static Correlation Function

Magnetic properties are deduced from the correlation function $\chi(\boldsymbol{r}_i, \boldsymbol{r}_j; \tau) = \langle \hat{\boldsymbol{S}}(\boldsymbol{r}_i, 0) \cdot \hat{\boldsymbol{S}}(\boldsymbol{r}_j, \tau) \rangle$, where $\boldsymbol{r}_i$ is the radius vector of the lattice site i. The structure factor in the momentum–Matsubara-frequency domain is given by

$$S(\boldsymbol{Q}, i\omega_n) = \frac{1}{V} \sum_{i,j} \int_0^\beta d\tau \chi(\boldsymbol{r}_i, \boldsymbol{r}_j; \tau) e^{-i[\boldsymbol{Q}\cdot(\boldsymbol{r}_j - \boldsymbol{r}_i) + \omega_n \tau]} \tag{5.2}$$

where $\boldsymbol{Q}$ belongs to the first Brillouin zone (BZ), $\omega_n = 2\pi n/\beta$ is the Matsubara frequency, and V is total number of spins. Static response is described by $S(\boldsymbol{Q}, 0)$, and the uniform magnetic susceptibility χ_u is given by $S(0, 0)$.

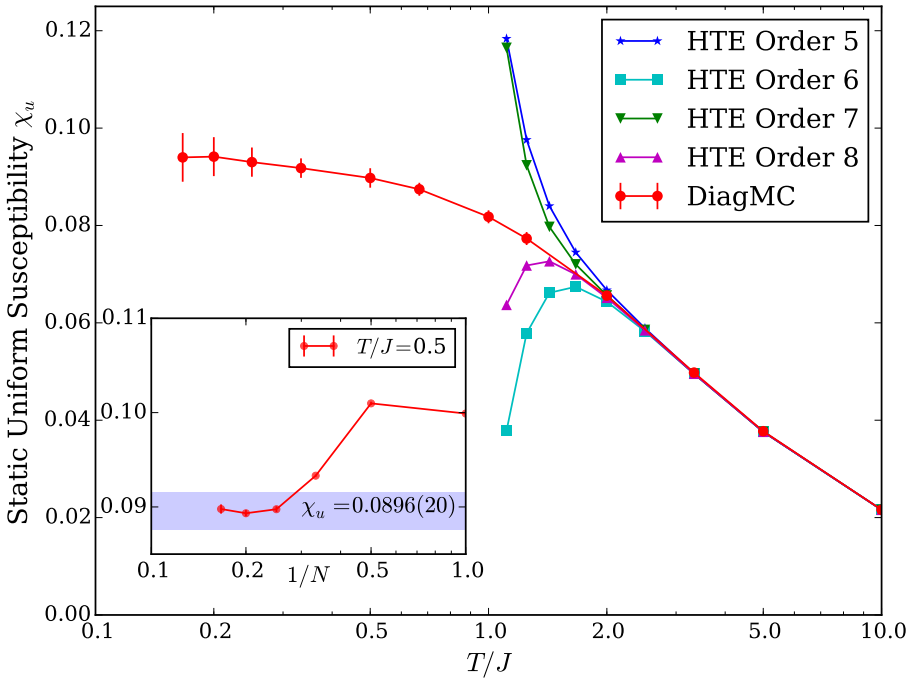

Figure 5.2. Uniform susceptibility χ_u as a function of temperature from the DiagMC approach(red circles) and from the high temperature expansion (HTE) method [2] truncated at different expansion orders. Inset: χ_u at $T/J = 1/2$ as a function of inverse maximal skeleton diagram order N. The errorbar on the final answer, shown as the blue region, is a combination of statistical Monte Carlo errors for fixed-N points and the systematic error of extrapolation to the $N \to \infty$ limit.

In Fig. 5.2 we compare DiagMC and the high-temperature expansion [2] results for χ_u. At high temperature $T/J > 2$ the agreement between the two methods is at the level of three meaningful digits. As temperature is lowered below $1.5J$, the high-T series explode while the diagrammatic series continue to converge at least down to $T/J \approx 1/6$. In the inset of Fig. 5.2 we show how χ_u depends on the inverse diagram order $1/N$ at $T/J = 1/2$. This temperature is well below the divergence point of the high-T series and, thus, is in the strongly correlated paramagnetic regime. Clearly, the answer does not change outside of error bars after accounting for 5-th and 6-th order diagrams.

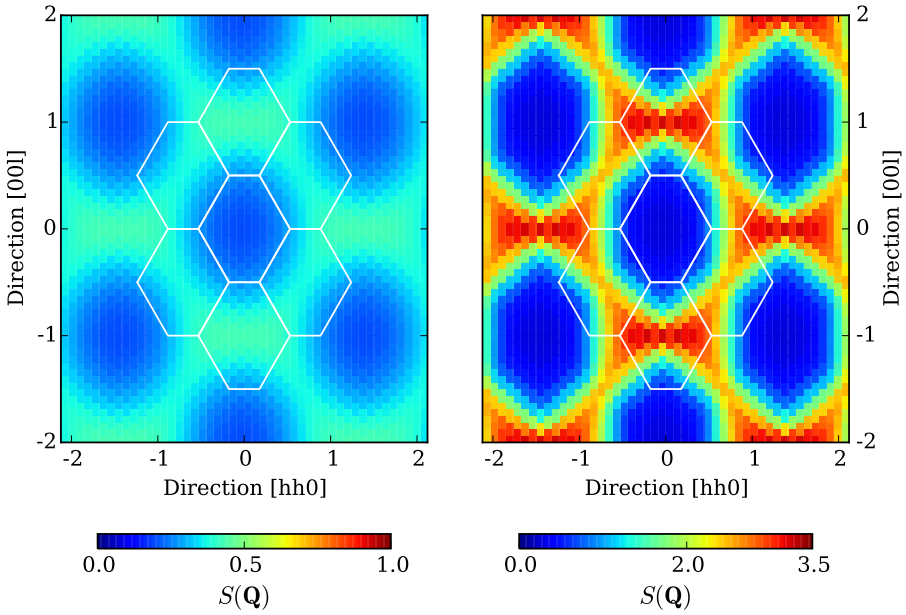

Figure 5.3. Structure factor $S(\boldsymbol{Q})$ in the $([hh0][00l])$ plane at $T/J = 2$ (left panel) and $T/J = 1/6$ (right panel). Note that the color scheme contrast (shown at the bottom) is significantly enhanced for the left panel.

In Fig. 5.3, we show the evolution of the static structure factor in the $([hh0][00l])$ plane of the reciprocal space from high $(T/J = 2)$ to low $(T/J = 1/6)$ temperature. As the temperature is lowered, the system goes through a smooth crossover from the high-T state with the checkerboard pattern in $S(\boldsymbol{Q}, 0)$ to the low-T state with the

bow-tie pattern and pseudo-singular pinch points. As pointed out in Refs. [20, 21], these strongly anisotropic pinch points are a direct consequence of the "2-in/2-out" ice rule. All by itself, this is strong evidence that at $T/J = 1/6$ the isotropic Heisenberg model is dominated by the spin-ice physics with excitations forming a dilute gas of "electric" charges.

5.4.2 Quantum-to-Classical Correspondence

Taking system configuration "snapshots" is equivalent to considering multi-point correlation functions in the diagrammatic approach (an impossible task for a large collection of spins), not to mention that the standard technique calculates their statistical averages. QCC comes to rescue here. In addition to (5.1), we consider the Ising model with spins $s = \pm 1$ and the classical Heisenberg model with unit-vector spins $\boldsymbol{s}$ on the pyrochlore lattice. Both classical models have nearly identical bow-tie patterns in $S(\boldsymbol{Q})$ at $T = 0$ [20, 21]. What we establish here, is an accurate QCC for spin correlation functions (static in the quantum case) between the original quantum model at temperature $T_{\rm QH}$ and its classical counterparts at temperatures $T_{\rm I}$ and $T_{\rm CH}$, respectively. The result is the "fingerprint" identification of dominant system configurations at low-T as originating from the spin-ice state (temperatures need to be fine-tuned because quantum and classical models have different spin values and configuration spaces [16]).

The QCC protocol is as follows. For the quantum system, we compute the static correlation function $\chi(\boldsymbol{r}) \equiv \int_0^\beta d\tau \chi(\boldsymbol{r}_0, \boldsymbol{r}_i; \tau)$ where $\boldsymbol{r} = \boldsymbol{r}_i - \boldsymbol{r}_0$ (its classical counterparts are defined similarly without the τ-dependence). We normalize the correlation functions to unity at the origin, $f(\boldsymbol{r}) = \chi(\boldsymbol{r})/\chi(0)$, and then consider the classical-model temperature ($T_{\rm I}$ or $T_{\rm CH}$) as a free parameter to obtain the best fit for $f(\boldsymbol{r})$ curves. The essence of QCC is that the entire functional dependence $f(\boldsymbol{r})$ is reproduced with high accuracy at all distances with this minimally required effort [16].

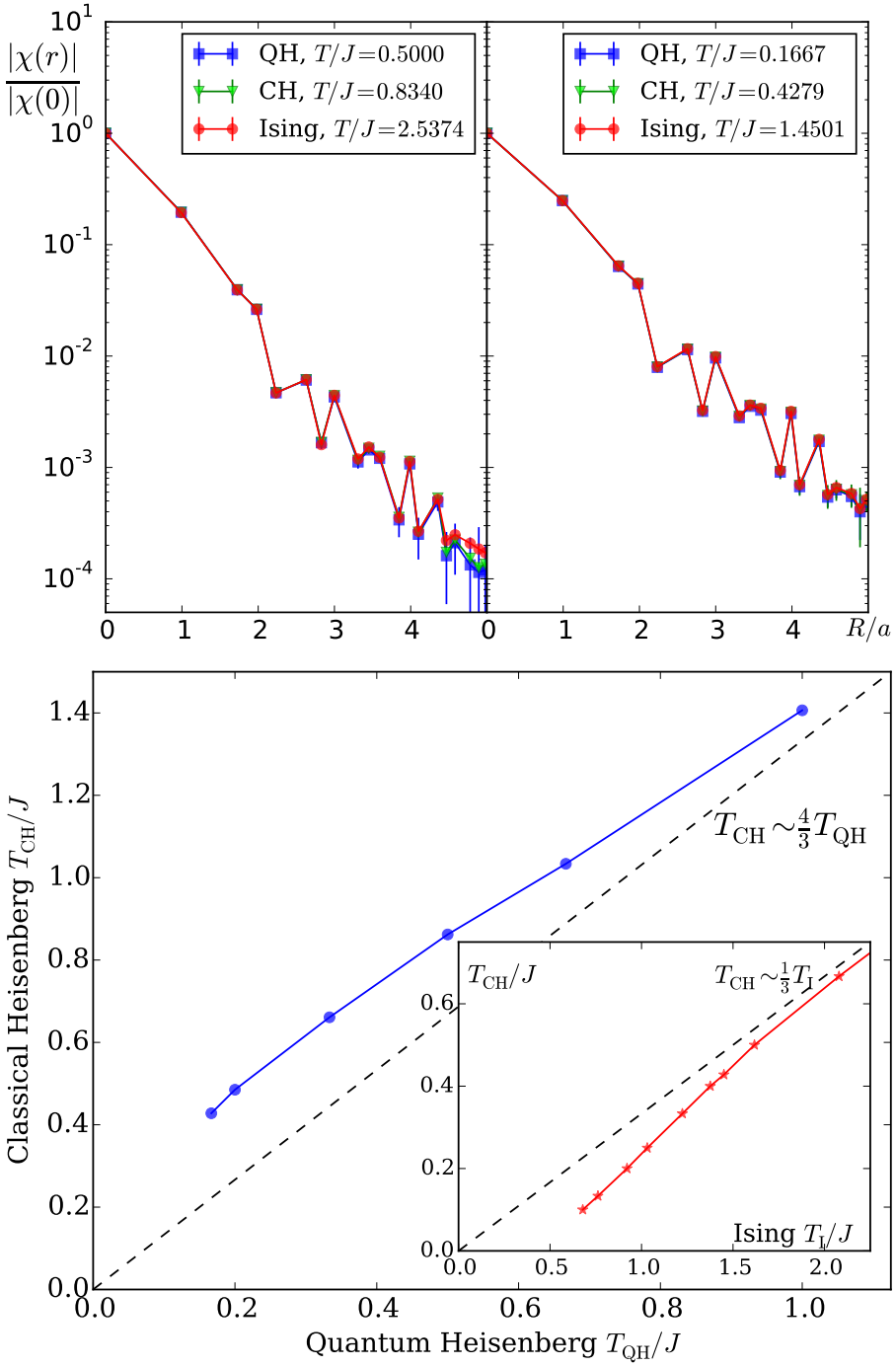

Figure 5.4. Upper panel: Normalized static susceptibilities (by modulus), $|\chi_s(\boldsymbol{r})/\chi_s(0)|$, in quantum Heisenberg, classical Heisenberg and classical Ising models at temperatures $T_{\rm QH}/J = 1/2$, $T_{\rm CH}/J = 0.8340$, $T_{\rm I}/J = 2.5374$ (left panel), and $T_{\rm QH}/J = 1/6$, $T_{\rm CH}/J = 0.4279$, $T_{\rm I}/J = 1.4501$ (right panel). The quantum-to-classical correspondence is satisfied within the error bars at all distances. Lower panel: Quantum-to-classical temperature relationship plot $T_{\rm CH}$ *vs* $T_{\rm QH}$. The straight black line is the high-T relation $T_{\rm CH} = (4/3)\, T_{\rm QH}$. Inset: temperature relationship $T_{\rm CH}$ *vs* $T_{\rm I}$ between the classical Heisenberg and Ising systems. The straight black line is the high-T relation $T_{\rm CH} = (1/3)\, T_{\rm I}$.

Remarkably, we observe a perfect match between the quantum result at $T_{\rm QH}$ and classical results at rescaled temperatures; the accuracy is at the sub-percent level at any temperature. In Fig. 5.4(a) we show two examples of QCC at $T_{\rm QH}/J = 1/2$ and $T_{\rm QH}/J = 1/6$. Since system "snapshots" are readily available in classical models, the identification of the quantum state becomes unambiguous. [It should be noted that QCC is absent for the equal-time correlation function $\chi(\boldsymbol{r}, \tau = 0)$.] The relationship between the temperature of the quantum Heisenberg model and its classical counterpart is plotted in the lower panel of Fig. 5.4; the relationship between the classical temperatures is shown in the inset of the lower panel in Fig. 5.4.

It is not surprising to observe QCC in two limiting cases: (i) at high temperature $T/J \gg 1$ when weak short-range correlations are captured at the lowest series-expansion order, and (ii) at distances much larger than the correlation length where statistical description in terms of the coarse-grained field becomes universal. What we observe is different: the correspondence holds at all distances starting from the nearest-neighbor sites and at all temperatures, including the crossover region $T/J \sim 1$. Similarly accurate QCC was reported for Heisenberg models on the square and triangular lattices [16] (it fails in 1D). Currently, sharp theoretical understanding of QCC for spin-1/2 magnetic systems in $D > 1$ is missing.

5.4.3 Dynamics

Having established that static properties correspond to those of the spin ice, we proceed with the study of dynamic response and compute the structure factor on the real frequency axis. This quantity can be directly measured in inelastic neutron scattering experiments. Real and Matsubara frequency functions are related to each other by the standard linear-response theory relation

$$S(\boldsymbol{Q}, i\omega_n) = \frac{1}{\pi}\int_0^\infty \frac{(1-e^{-\beta\omega})\omega}{\omega_n^2+\omega^2} S(\boldsymbol{Q},\omega)d\omega \tag{5.3}$$

This integral equation is solved using numerical analytic continuation methods [35, 36]. The result for two characteristic momentum points $\boldsymbol{Q}_1 = (0, 0, \frac{2\pi}{a})$ and $\boldsymbol{Q}_2 = (0, 0, \frac{5\pi}{4a})$, where a is the lattice constant, is shown in Fig. 5.5. On the basis of the thermal spin-ice picture, we expect two dynamic contributions: one from slow diffusive motion of spinons and the other from propagating spin waves. At the pinch point $\boldsymbol{Q}_1$, the dynamic response is best described as that of the diffusive (Drude-type) spinon peak [20]. The second point $(0, 0, \frac{5\pi}{4a})$ is on one of the nodal lines, which correspond to special directions along which the spinon contribution is suppressed due to the ice rule and lattice structure [20, 67]. Indeed, for this point the diffusive peak at $\omega = 0$ is absent, and a broad continuum originating from local spin fluctuations with the typical energy scale $\omega \sim J$ emerges instead.

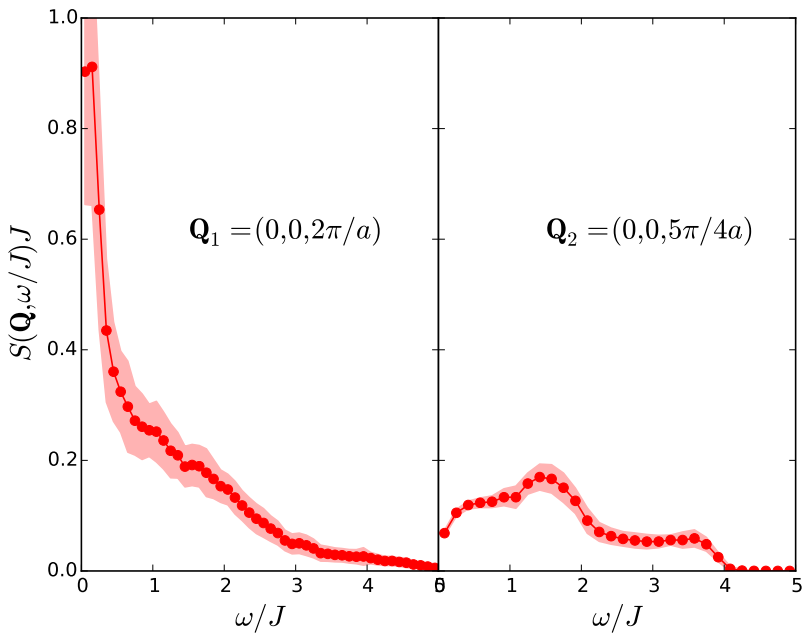

Figure 5.5. Dynamic structure factor as a function of frequency at the pinch point $\boldsymbol{Q}_1 = (0, 0, 2\pi/a)$ (left panel) and on the nodal line at $\boldsymbol{Q}_2 = (0, 0, 5\pi/4a)$.

5.5 Conclusion and Discussions

Using the BDMC technique, we carried out a systematic investigation of the quantum SU(2)-symmetric Heisenberg AFM on the pyrochlore lattice. The correlated paramagnetic state at temperature well below the exchange coupling constant is unambiguously identified as the thermal spin-ice phase. The U(1) spin liquid (predicted from perturbative studies of the strongly anisotropic XXZ model) has not been observed. Apparently, the characteristic temperature to see the emergent gauge structure is much lower than $T/J = 1/6$.

Our work paves the road for applications of BDMC to studies of frustrated magnetic materials with complicated Hamilitonians when in (5.1) the exchange constant J is replaced with a 3×3 tensor and interactions are extended beyond the nearest-neighbor sites [68, 69]. Dealing with such Hamiltonians does not present any additional burden for the BDMC method because in the skeleton formulation all lines are automatically assumed to be fully renormalized and non-local in space-time. Our work demonstrates that it is possible to use BDMC to perform accurate *ab initio* calculations of both static and dynamic response for frustrated magnets, and obtain results that can be directly compared with experiments such as the inelastic neutron scattering. In particular, one's ability to enter the strongly correlated regime and accurately compute properties at temperatures significantly below J leads to the possibility of extracting the relevant Hamiltonian parameters for frustrated magnetic materials from measurements.

CONCLUSIONS

In this dissertation, we performed numerical studies on two types of strongly correlated quantum spin models that are possible candidates for the spin liquid state.

In Chapter 1, we study the J-Q model at the Nèel to valence-bond solid quantum phase transition, which is known as the testbed of the deconfined criticality theory. Through a directly comparison by the flowgram method between the Nèel-VBS transition and the SU(2)-symmetric discrete NCCP^1 representation of the deconfined critical action, we find that the flows of two systems coincide in a broad region of linear system sizes, implying that the theory correctly captures the mesoscopic physics of competition between the antiferromagnetic and valence-bond orders in quantum spin systems. At larger sizes, however, we observe significant deviations between the two flows which both demonstrate strong violations of scale invariance. This reliably rules out the second-order transition scenario in at least one of the two models and suggests that the most likely explanation for the nature of the transition in the J-Q model is weak first-order transition.

From Chapter 2 to Chapter 5, we study a more general family of candidates for the intriguing quantum spin-liquid state, the frustrated magnets. In Chapter 2, we introduce the bold diagrammatic Monte Carlo method based on the G^2W-skeleton expansion, and also explore the possibility of employing the full skeleton technique based on the effective three-point vertex. In Chapter 3, we introduce a new approach, referred to as the conserving bold diagrammatic Monte Carlo method, which allows us to construct observables that satisfy conservation laws order by order in the bold diagrammatic Monte Carlo framework. In Chapter 4, we show the results from BDMC

and CBDMC simulations in various quantum spin systems with or without frustration and compare the performance with high-temperature expansions.

In Chapter 5, we study the low-temperature physics of the SU(2)-symmetric spin-1/2 Heisenberg antiferromagnet on the pyrochlore lattice and find fingerprint evidence for the thermal spin-ice state in this frustrated quantum magnet. Our conclusions are based on the results of bold diagrammatic Monte Carlo simulations, with good convergence of the skeleton series down to the temperature $T = J/6$. The identification of the spin-ice state is done through a remarkably accurate microscopic correspondence for the static structure factor between the quantum Heisenberg, classical Heisenberg, and Ising models at all accessible temperatures, and the characteristic bow-tie pattern with pinch points observed at $T = J/6$. We also obtained the dynamic structure factor at real frequencies by the analytic continuation of numerical data, showing results consistent with diffusive spinon dynamics at the pinch points.

With our diagrammatic Monte Carlo tool, it is possible to perform accurate *ab-initio* calculations of both static and dynamic response for frustrated magnets, and directly compare with experiments such as the inelastic neutron scattering. In particular, one's ability to enter the strongly correlated regime and accurately compute properties at temperatures significantly below J leads to the possibility of extracting the relevant Hamiltonian parameters for frustrated magnetic materials from measurements.

BIBLIOGRAPHY

[1] L. G. Molinari and N. Manini, *Enumeration of many-body skeleton diagrams*, Euro. Phys. Journal. B, 51 (2006), pp. 331–336.

[2] H.-J. Schmidt, A. Lohmann, and J. Richter, *Eighth-order high-temperature expansion for general Heisenberg Hamiltonians*, Physical Review B, 84 (2011).

[3] L. Savary and L. Balents, *Quantum spin liquids: a review*, Reports on Progress in Physics, 80 (2017), p. 016502.

[4] P. A. Lee, *An End to the Drought of Quantum Spin Liquids*, Science, 321 (2008), pp. 1306–1307.

[5] T. Senthil, A. Vishwanath, L. Balents, S. Sachdev, and M. P. A. Fisher, *Deconfined Quantum Critical Points*, Science, 303 (2004), pp. 1490–1494.

[6] T. Senthil, L. Balents, S. Sachdev, A. Vishwanath, and M. P. A. Fisher, *Quantum criticality beyond the Landau-Ginzburg-Wilson paradigm*, Physical Review B, 70 (2004), p. 144407.

[7] ——, *Deconfined Criticality Critically Defined*, Journal of the Physical Society of Japan, 74 (2005), pp. 1–9.

[8] A. B. Kuklov, N. V. Prokofev, B. V. Svistunov, and M. Troyer, *Deconfined criticality, runaway flow in the two-component scalar electrodynamics and weak first-order superfluid-solid transitions*, Annals of Physics, 321 (2006), pp. 1602–1621.

[9] A. B. Kuklov, M. Matsumoto, N. V. Prokofev, B. V. Svistunov, and M. Troyer, *Deconfined Criticality: Generic First-Order Transition in the SU(2) Symmetry Case*, Physical Review Letters, 101 (2008), p. 050405.

[10] A. W. Sandvik, *Evidence for Deconfined Quantum Criticality in a Two-Dimensional Heisenberg Model with Four-Spin Interactions*, Physical Review Letters, 98 (2007), p. 227202.

[11] R. G. Melko and R. K. Kaul, *Scaling in the Fan of an Unconventional Quantum Critical Point*, Physical Review Letters, 100 (2008), p. 017203.

[12] J. Lou, A. W. Sandvik, and N. Kawashima, *Antiferromagnetic to valence-bond-solid transitions in two-dimensional SU(N) Heisenberg models with multi-spin interactions*, Physical Review B, 80 (2009), p. 180414.

[13] F.-J. Jiang, M. Nyfeler, S. Chandrasekharan, and U.-J. Wiese, *From an antiferromagnet to a valence bond solid: evidence for a first-order phase transition*, Journal of Statistical Mechanics: Theory and Experiment, 2008 (2008), p. P02009.

[14] A. W. Sandvik, *Continuous Quantum Phase Transition between an Antiferromagnet and a Valence-Bond Solid in Two Dimensions: Evidence for Logarithmic Corrections to Scaling*, Physical Review Letters, 104 (2010), p. 177201.

[15] L. Balents, *Spin liquids in frustrated magnets*, Nature, 464 (2010), pp. 199–208.

[16] S. Kulagin, N. V. Prokof'ev, O. Starykh, B. V. Svistunov, and C. N. Varney, *Bold Diagrammatic Monte Carlo technique for frustrated spin systems*, Physical Review B, 87 (2013).

[17] S. A. Kulagin, N. Prokof'ev, O. A. Starykh, B. Svistunov, and C. N. Varney, *Bold Diagrammatic Monte Carlo Method Applied to Fermionized Frustrated Spins*, Physical Review Letters, 110 (2013).

[18] N. V. Prokof'ev and B. V. Svistunov, *Bold Diagrammatic Monte Carlo: When Sign Problem is Welcome*, Physical Review Letters, 99 (2007).

[19] V. N. Popov and S. A. Fedotov, *The functional-integration method and diagram technique for spin systems*, Journal of Experimental and Theoretical Physics, 67 (1988), p. 535.

[20] C. L. Henley, *Power-law spin correlations in pyrochlore antiferromagnets*, Physical Review B, 71 (2005), p. 014424.

[21] S. V. Isakov, K. Gregor, R. Moessner, and S. L. Sondhi, *Dipolar Spin Correlations in Classical Pyrochlore Magnets*, Physical Review Letters, 93 (2004), p. 167204.

[22] K. Chen, Y. Huang, Y. Deng, A. B. Kuklov, N. V. Prokofev, and B. V. Svistunov, *Deconfined Criticality Flow in the Heisenberg Model with Ring-Exchange Interactions*, Physical Review Letters, 110 (2013), p. 185701.

[23] O. I. Motrunich and A. Vishwanath, *Emergent photons and transitions in the $O(3)$ sigma model with hedgehog suppression*, Physical Review B, 70 (2004), p. 075104.

[24] L. Balents, L. Bartosch, A. Burkov, S. Sachdev, and K. Sengupta, *Putting competing orders in their place near the Mott transition*, Physical Review B, 71 (2005), p. 144508.

[25] ——, *Putting competing orders in their place near the Mott transition. II. The doped quantum dimer model*, Physical Review B, 71 (2005), p. 144509.

[26] R. Moessner, S. L. Sondhi, and E. Fradkin, *Short-ranged resonating valence bond physics, quantum dimer models, and Ising gauge theories*, Physical Review B, 65 (2001), p. 024504.

[27] E. Babaev, *Phase diagram of planar U(1)× U(1) superconductor: Condensation of vortices with fractional flux and a superfluid state*, Nuclear Physics B, 686 (2004), pp. 397–412.

[28] J. Smiseth, E. Smrgrav, E. Babaev, and A. Sudb, *Field- and temperature-induced topological phase transitions in the three-dimensional n-component london superconductor*, Physical Review B, 71 (2005), p. 214509.

[29] S. Sachdev, *Finite temperature dissipation and transport near quantum critical points*, arXiv:0910.1139 [cond-mat, physics:hep-th], 20103812 (2010), pp. 3–30.

[30] H. P. Bchler, M. Hermele, S. D. Huber, M. P. A. Fisher, and P. Zoller, *Atomic Quantum Simulator for Lattice Gauge Theories and Ring Exchange Models*, Physical Review Letters, 95 (2005), p. 040402.

[31] A. W. Sandvik, S. Daul, R. R. P. Singh, and D. J. Scalapino, *Striped Phase in a Quantum xy Model with Ring Exchange*, Physical Review Letters, 89 (2002), p. 247201.

[32] A. W. Sandvik and R. G. Melko, *Ground-state phases and quantum phase transitions in a two-dimensional spin-1/2 XY model with four-spin interactions*, Annals of Physics, 321 (2006), pp. 1651–1668.

[33] V. N. Popov and F. S. A., *The functional-integration method and diagram technique for spin systems*, Sov. Phys. JETP, 67 (1988), p. 535.

[34] H. O. John W. Negele, *Quantum many-particle systems*, 68 of Frontiers in physics (1988).

[35] A. S. Mishchenko, N. V. Prokofev, A. Sakamoto, and B. V. Svistunov, *Diagrammatic quantum Monte Carlo study of the fröhlich polaron*, Physical Review B, 62 (2000), pp. 6317–6336.

[36] N. V. Prokofev and B. V. Svistunov, *Spectral analysis by the method of consistent constraints*, JETP Letters, 97 (2013), pp. 649–653.

[37] N. V. Prokof'ev and B. V. Svistunov, *Polaron problem by diagrammatic quantum monte carlo*, Phys. Rev. Lett., 81 (1998), pp. 2514–2517.

[38] N. V. Prokof'ev, B. V. Svistunov, and I. S. Tupitsyn, *worm algorithm in quantum monte carlo simulations*, Physics Letters A, 238 (1998), pp. 253–257.

[39] L. Hedin, *New method for calculating the one-particle green's function with application to the electron-gas problem*, Phys. Rev., 139 (1965), pp. A796–A823.

[40] A. W. Sandvik, *Critical temperature and the transition from quantum to classical order parameter fluctuations in the three-dimensional heisenberg antiferromagnet*, Phys. Rev. Lett., 80 (1998), pp. 5196–5199.

[41] G. Baym and L. P. Kadanoff, *Conservation laws and correlation functions*, Phys. Rev., 124 (1961), pp. 287–299.

[42] H.-J. Schmidt, A. Lohmann, and J. Richter, *Eighth-order high-temperature expansion for general heisenberg hamiltonians*, Phys. Rev. B, 84 (2011), p. 104443.

[43] W. Zheng, R. R. P. Singh, R. H. McKenzie, and R. Coldea, *Temperature dependence of the magnetic susceptibility for triangular-lattice antiferromagnets with spatially anisotropic exchange constants*, Phys. Rev. B, 71 (2005), p. 134422.

[44] Y. Huang, K. Chen, Y. Deng, N. Prokofev, and B. Svistunov, *Spin-Ice State of the Quantum Heisenberg Antiferromagnet on the Pyrochlore Lattice*, Physical Review Letters, 116 (2016), p. 177203.

[45] A. P. Ramirez, *Strongly Geometrically Frustrated Magnets*, Annual Review of Materials Science, 24 (1994), pp. 453–480.

[46] P. W. Anderson, *Resonating valence bonds: A new kind of insulator?*, Materials Research Bulletin, 8 (1973), pp. 153–160.

[47] J. N. Reimers, J. E. Greedan, R. K. Kremer, E. Gmelin, and M. A. Subramanian, *Short-range magnetic ordering in the highly frustrated pyrochlore $Y_2Mn_2O_7$*, Physical Review B, 43 (1991), pp. 3387–3394.

[48] J. S. Gardner, B. D. Gaulin, S.-H. Lee, C. Broholm, N. P. Raju, and J. E. Greedan, *Glassy Statics and Dynamics in the Chemically Ordered Pyrochlore Antiferromagnet $Y_2Mo_2O_7$*, Physical Review Letters, 83 (1999), pp. 211–214.

[49] C. H. Booth, J. S. Gardner, G. H. Kwei, R. H. Heffner, F. Bridges, and M. A. Subramanian, *Local lattice disorder in the geometrically frustrated spin-glass pyrochlore $Y_2Mo_2O_7$*, Physical Review B, 62 (2000), pp. R755–R758.

[50] M. J. Harris, S. T. Bramwell, D. F. McMorrow, T. Zeiske, and K. W. Godfrey, *Geometrical Frustration in the Ferromagnetic Pyrochlore $Ho_2Ti_2O_7$*, Physical Review Letters, 79 (1997), pp. 2554–2557.

[51] R. Siddharthan, B. S. Shastry, A. P. Ramirez, A. Hayashi, R. J. Cava, and S. Rosenkranz, *Ising Pyrochlore Magnets: Low-Temperature Properties, "Ice Rules," and Beyond*, Physical Review Letters, 83 (1999), pp. 1854–1857.

[52] S. T. Bramwell and M. J. P. Gingras, *Spin Ice State in Frustrated Magnetic Pyrochlore Materials*, Science, 294 (2001), pp. 1495–1501.

[53] J. S. Gardner, B. D. Gaulin, A. J. Berlinsky, P. Waldron, S. R. Dunsiger, N. P. Raju, and J. E. Greedan, *Neutron scattering studies of the cooperative paramagnet pyrochlore $Tb_2Ti_2O_7$*, Physical Review B, 64 (2001), p. 224416.

[54] S.-W. Han, J. S. Gardner, and C. H. Booth, *Structural properties of the geometrically frustrated pyrochlore $Tb_2Ti_2O_7$*, Physical Review B, 69 (2004), p. 024416.

[55] T. Fennell, M. Kenzelmann, B. Roessli, M. K. Haas, and R. J. Cava, *Power-Law Spin Correlations in the Pyrochlore Antiferromagnet $Tb_2Ti_2O_7$*, Physical Review Letters, 109 (2012), p. 017201.

[56] N. Prokof'ev and B. Svistunov, *From Popov-Fedotov trick to universal fermionization*, arXiv:1103.3730 [cond-mat, physics:hep-lat], (2011).

[57] R. Moessner and J. T. Chalker, *Low-temperature properties of classical, geometrically frustrated antiferromagnets*, Physical Review B, 58 (1998), pp. 12049–12062.

[58] ——, *Properties of a Classical Spin Liquid: The Heisenberg Pyrochlore Antiferromagnet*, Physical Review Letters, 80 (1998), pp. 2929–2932.

[59] B. Canals and C. Lacroix, *Pyrochlore Antiferromagnet: A Three-Dimensional Quantum Spin Liquid*, Physical Review Letters, 80 (1998), pp. 2933–2936.

[60] B. Canals and C. Lacroix, *Quantum spin liquid: The Heisenberg antiferromagnet on the three-dimensional pyrochlore lattice*, Physical Review B, 61 (2000), pp. 1149–1159.

[61] M. Hermele, M. P. A. Fisher, and L. Balents, *Pyrochlore photons: The $U(1)$ spin liquid in a $S = 1/2$ three-dimensional frustrated magnet*, Physical Review B, 69 (2004), p. 064404.

[62] C. L. Henley, *The Coulomb Phase in Frustrated Systems*, Annual Review of Condensed Matter Physics, 1 (2010), pp. 179–210.

[63] P. W. Anderson, *Ordering and Antiferromagnetism in Ferrites*, Physical Review, 102 (1956), pp. 1008–1013.

[64] M. P. Zinkin, M. J. Harris, and T. Zeiske, *Short-range magnetic order in the frustrated pyrochlore antiferromagnet $CsNiCrF_6$*, Physical Review B, 56 (1997), pp. 11786–11790.

[65] A. Banerjee, S. V. Isakov, K. Damle, and Y. B. Kim, *Unusual Liquid State of Hard-Core Bosons on the Pyrochlore Lattice*, Physical Review Letters, 100 (2008), p. 047208.

[66] J.-P. Lv, G. Chen, Y. Deng, and Z. Y. Meng, *Coulomb liquid phases of bosonic cluster Mott insulators on a pyrochlore lattice*, Physical Review Letters, 115 (2015).

[67] P. H. Conlon and J. T. Chalker, *Spin Dynamics in Pyrochlore Heisenberg Antiferromagnets*, Physical Review Letters, 102 (2009), p. 237206.

[68] S. H. Curnoe, *Structural distortion and the spin liquid state in* $Tb_2Ti_2O_7$, Physical Review B, 78 (2008), p. 094418.

[69] K. A. Ross, L. Savary, B. D. Gaulin, and L. Balents, *Quantum Excitations in Quantum Spin Ice*, Physical Review X, 1 (2011), p. 021002.